Controlled Synthesis, Processing, and Applications of Structural and Functional Nanomaterials

ASSESSING THE LIMITS OF ACCURACY FOR THE TAUC METHOD FOR OPTICAL BAND GAP DETERMINATION

Dunbar P. Birnie, III
Rutgers University, Department of Materials Science and Engineering
New Brunswick, New Jersey, 08854-8065

ABSTRACT

Scientists and engineers working with nanotechnology and thin film optical devices often make use of “Tauc plots” to determine band gaps and evaluate the effect of processing conditions on the quality of coatings made for these applications. Broad-band optical data are easy to acquire and usually exhibit a region of reasonable transparency and then a sharp rise in absorption with increasing photon energy as the band-gap energy is exceeded. The shape of the onset of absorption is diagnostic of whether the band-gap is direct or indirect. Then, an appropriate linear regression can be used to extrapolate to the band gap value, though sometimes the extrapolation is quite far in absolute energy terms from the data used to make the extrapolation. This paper covers some of our recent work where we use known materials to standardize the fitting protocols and assess the accuracy of this simple method.

INTRODUCTION

In our earlier work with thin films (and for many studies in the literature that use the Tauc method) we’ve noticed that the distance of extrapolation in the fitting process may be relatively large, and the tail of sub-band-gap absorption can also be quite large. This raised the basic question about how accurate the Tauc method would be, and how to establish procedures that improve the accuracy of the fitting results[1]. We delved deeply into this problem by looking at ZnO thin films because they are an extremely well-studied material and ZnO is known to have a direct band gap. By looking closely at a population of over 120 thin film Tauc fits we found the band-gap results overall were consistent with a value of 3.27 +/- 0.05 eV, with evidence for two small outlier populations [1]. A subpopulation of higher gap values appeared to be caused by nanoparticle quantum confinement effects (not surprisingly), while a subpopulation of lower gap values appeared to be correlated with more defective samples. These were essentially cases that had stronger sub-band-gap absorption, which has the mathematical effect of shifting the intercept point somewhat to the left and making the confidence interval of the band-gap determination wider (less accurate). To quantify this effect and provide a figure of merit for identifying the more accurate samples, we introduced the “near-edge absorptivity ratio (NEAR)”. And, when using the NEAR to focus on the more accurate data sets, we found that the Tauc method generally gave an experimental distribution of results with a standard deviation of only 0.033 eV, thus emphasizing the relatively high accuracy of the method in general.

We extend that work to the case of indirect band-gap materials and examine accuracy limits based on absorption coefficient values and coating thickness effects that can influence the signal-to-noise ratio of real optical absorption data. Indirect band-gaps are more difficult to characterize because their absorption intensities are characteristically weaker, which provides an added difficulty when most optical data are determined from thin film samples. We address this problem by working with single crystal data from silicon, probably the most well-characterized indirect band-gap material available.

BACKGROUND

The seminal work of Tauc, Grigorovici, and Vancu [2] presented a simple method that uses broad band absorption spectra and interpreted the shape of the absorption edge to arrive at a

determination of the band gap, and its character. Their method was further developed in Davis and Mott's more general work on amorphous semiconductors [3, 4]. Together they've shown that the optical absorption strength depends on the difference between the photon energy and the band gap as shown in (Eq. 1):

$$(\alpha h\nu)^{1/n} = A(h\nu - E_g) \quad (1)$$

where h is Planck's constant, ν is the photon's frequency, α is the absorption coefficient, Eg is the band gap and A is a proportionality constant. The value of the exponent denotes the nature of the electronic transition, whether allowed or forbidden and whether direct or indirect:

For direct allowed transitions	n=1/2
For direct forbidden transitions	n=3/2
For indirect allowed transitions	n=2
For indirect forbidden transitions	n=3

Typically, the allowed transitions dominate the basic absorption processes, giving either n=1/2 or n=2, for direct and indirect transitions, respectively.

Thus, the basic procedure for a Tauc analysis is to acquire optical absorbance data for the sample in question that spans a range of energies from below the band gap transition to above it. Then, plotting the (α h ν) with various test exponents versus photon energy allows the researcher to decide which of the exponents gives the most linear plot. Finally, with this exponent, the line is extrapolated down to intersect the X-axis, which will be the band-gap value (as can be interpreted from Equation 1). Of the four exponent choices listed, it is usually found that either the ½ and 2 exponents are most frequently used (being associated with the allowed transitions).

ANALYSIS OF DIRECT-GAP MATERIALS

Zinc oxide was a good candidate for evaluating the Tauc method because it has been widely studied for a number of useful applications [5-13]. Among these applications the band-gap plays a central and fundamental role as it controls many absorption and conductivity phenomena. Single crystal optical studies have found a direct band gap of 3.3 eV[14-16], though many of the papers surveyed in our thin film analysis were collected from very well crystallized films or even epitaxially grown layers[1]. ZnO was also attractive as a reference material because of its high level of stoichiometry. While every stoichiometric compound must thermodynamically have point defects at some level (and therefore by definition be non-stoichiometric), the phase of ZnO has been experimentally studied and found to have very little deviation from the ideal 1:1 ratio. For example, the early work of Allsopp and Roberts found a slight zinc excess, but less than 50 ppm [17]. This is much more stoichiometric than many phases and thus provided a good calibration test-case for the Tauc method.

Figure 1 gives one example Tauc plot for ZnO where the absorption coefficient times the photon energy to the second power is plotted versus the incident photon energy[18]. The second power was used as zinc oxide is well known to have a direct allowed transition. The characteristic features of Tauc plots are evident: at low photon energies the absorption approaches zero – the material is transparent; near the band-gap value the absorption gets stronger and shows a region of linearity in this squared-exponent plot. This linear region has been used to extrapolate to the X-axis intercept to find the band gap value (here about 3.28 eV).

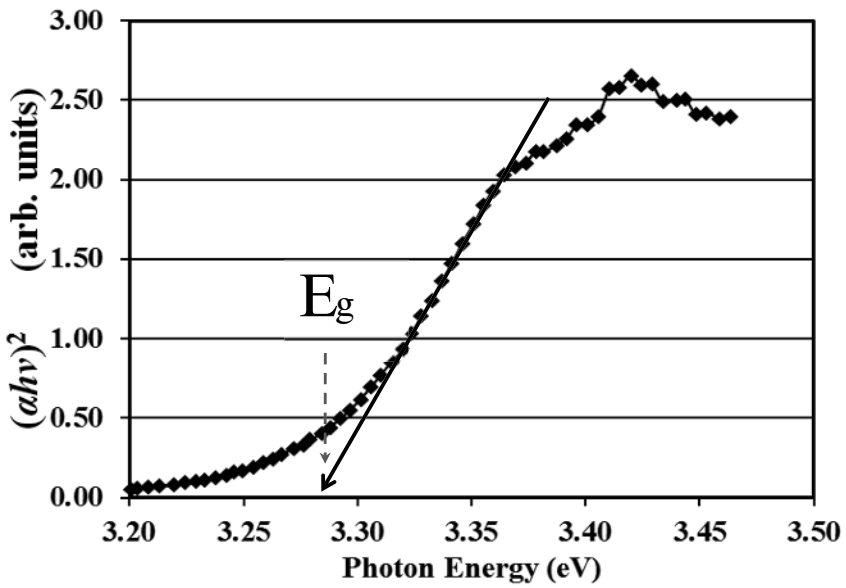

Figure 1: Example Tauc Plot from UV-Vis analysis of a ZnO thin film, illustrating the method of fitting the linear region to extrapolate the band-gap at the X-axis intercept, here about 3.28 eV. Data replotted from ref.[18].

At even higher energies the absorption processes saturate and the curve again deviates from linear. To select and justify a linear region for extrapolation one must understand the reasons for these lower and upper deviations from linear behavior. On the low energy end, the deviation from linearity can be associated with defect absorption states that are near the band edge. This phenomenon has been investigated by Urbach [19] and in subsequent years, therefore, identified as an "Urbach Tail." These states are usually described by an exponential function, corresponding to a typical distribution of density of states, evident in the absorption behavior seen in the example Tauc plot (Figure 1). On the high energy end, saturation of available transition states can be responsible for a leveling out of absorption strength in most collected spectra.

The absorption data are rooted in the possible optical transitions within the electronic structure of the material. Figure 2 (next page) shows the band diagram for ZnO[20], showing that the material is direct and that the band-gap derives from states at, Γ, the center of the Brillouin Zone. A representative direct optical transition is shown for a photon energy slightly larger than the band-gap energy.

Selecting the "right" points to use for fitting from Figure 1 is largely subjective, but could also have a profound effect on the extrapolated value for the band-gap. In our earlier work on ZnO, we tried to develop a completely unbiased method for picking the linear portion of the plot and finding the band gap value[1]. Digital data were processed in a spreadsheet to achieve a

series of linear regressions corresponding to incremental portions of the data set. We typically fitted using an 11-data-point window for evaluating the local linear regression (using +/- 5 datapoints on either side for any given local fit), and then we slid this fitting-window along and tested the fit at every possible location. The impact of fitting window width can be illustrated in Figure 3 where we plot the R^2 value for each incremental linear regression fit for the data we extracted from the graph shown in Figure 1. Three different curves are presented that cover 5, 11, and 15 datapoint fitting windows, respectively. When fewer data points are used for fitting then better R^2 results are generally obtained (as a mathematical certainty). However, if the actual linear region is relatively short then using a bigger span of datapoints will force the inclusion of points that are clearly not part of the linear region and the R^2 value will be reduced. Or, similarly when fitting a line to a clearly curved part of the dataset, the same R^2 reduction will occur. Figure 3 illustrates this behavior with the general trend downward for the energy values between 3.2 and 3.3 eV (see arrow). Referring back to Figure 1, it can be seen that this is a

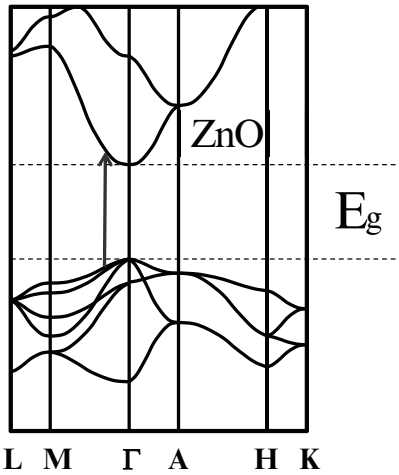

Figure 2: Band diagram for ZnO showing direct transitions at the central Γ point. One direct transition at slightly higher energy is illustrated.

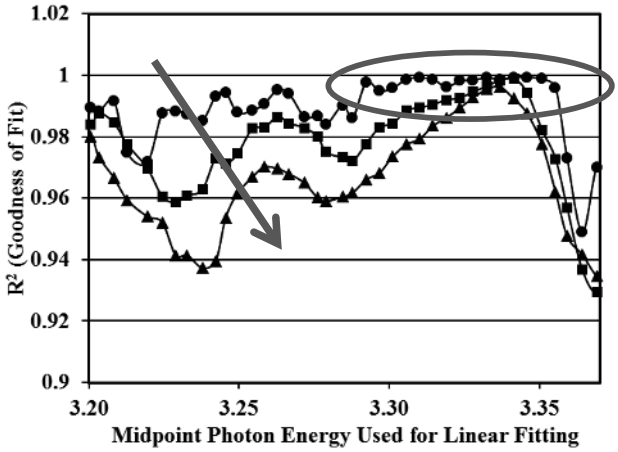

Figure 3: Linear regression fitting quality for different portions of the data as a method of choosing the best region for extrapolating the "Tauc gap": using (●) 5, (■) 11, or (▲) 15 sequential points.

region of upward curvature for the Tauc plot, so that extending the fit to larger ranges of data can force the inclusion of more curvature and therefore poorer fits (as shown). The best fit values are found in the mid-point photon energy region between 3.30 and 3.35 eV (as marked with the red ellipse in Figure 3). In our analysis, each linear regression can be evaluated to find the X-axis intercept (the band gap value). Figure 4 shows how this band gap/intercept value changes depending on which set of adjacent datapoints was used for linear regression fitting. The best R^2 values for fitting correspond to the band gap values highlighted with the ellipse, all around 3.28 eV. Note that the choice of the width of fitting window imposes only a slight change in extrapolated band gap value establishing a method-imposed precision of about +/-0.005 eV. Interestingly, the standard regression error from any specific fit can be used to calculate a confidence interval for specific fit's extrapolated bandgap value. For the data shown in Figure 1-4 the best-fit region is found to have 95% confidence intervals of +/-0.0025 eV, +/-0.0015 eV, and +/-0.0023 eV, for the 5, 11, and 15 point fitting windows, respectively. The smaller fitting window has a better R^2 value, but the extrapolation is poorer because it is based on a narrower range of energy values and fewer data points. The largest fitting window has a wider basis for making the extrapolation, but the R^2 value is a little lower and the confidence interval a little wider, too. In any case, these confidence intervals must be considered the best precision values for the technique, though when many measurements are considered and compared the accuracy is not as good as this.

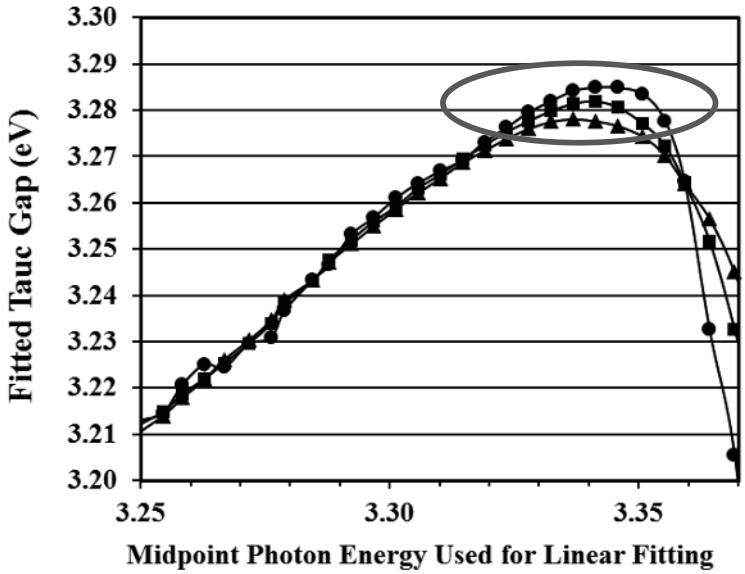

Figure 4: Fitted Tauc gap obtained from linear regression fits covered in Figure 1 and 3. The region where the best R^2 values resulted is also the region where the fitting slope is steepest and the largest Tauc gap intercept is found: (●) 5, (■) 11, and (▲) 15 sequential points used.

In view of the importance of the overlap between the linear region used for Tauc gap fitting and the lower energy Urbach tail absorption effects we also have tried to provide a quantitative measure for comparing different plots and data[1]. We noted that if there were no Urbach tail at all then the absorption would be zero up to the optical gap and then rise linearly according to equation (1). So we suggest that the $(\alpha h\nu)^2$ value measured at the Tauc gap should relate to the size of the Urbach tail, though perhaps not to its energy breadth or shape in detail. Often the Tauc plots are put on an arbitrary units scale, so we normalize this value by comparing it to a $(\alpha h\nu)^2$ value at slightly higher energy. To make it generalizable we suggested normalizing using a value taken at 2% higher energy than the Tauc gap that has been determined by the fitting process, ie. @ hν = 1.02Eg. To generalize this further and make the concept applicable to indirect materials, also, we take the square root and correct for the 2% difference in photon energy to arrive at a factor we call the "Near-Edge Absorptivity Ratio", or NEAR, which is essentially the ratio of the absorption coefficients at those two energy values.

$$NEAR = 1.02\left\{\frac{(\alpha h\nu)^2|_{h\nu=E_{gap}}}{(\alpha h\nu)^2|_{h\nu=1.02E_{gap}}}\right\}^{1/2} = \frac{\alpha(E_{gap})}{\alpha(1.02E_{gap})} \qquad (2)$$

Note that this ratio is dimensionless and can thus be evaluated from $(\alpha h\nu)^2$ graphs even when arbitrary units are used in the plots. The +2% offset is arbitrary and merely intended to probe how steep the curve is close to the Tauc gap. Similarly, when the NEAR factor would be applied to an indirect-gap material (where the $(\alpha h\nu)^n$ would have been plotted with a ½ power, then the ratio would need to be squared to yield a dimensionless absorption coefficient ratio.

This NEAR factor was shown to be correlated with the accuracy of the band-gap determined using the Tauc method [1]. Certainly, sharper absorption data that come closer to the X-axis before exhibiting their Urbach tail will be mathematically more likely to have a more accurate band-gap value.

ANALYSIS OF INDIRECT-GAP MATERIALS

The case of indirect band-gap materials is quite a bit more complicated since every indirect band-gap material will also, eventually, have direct band optical transitions that start to come into play at photon energies above the indirect gap value. In this regard, many publications provide both the n=1/2 and n=2 plots and use these to extract the indirect edge as well as the lowest of the direct band transitions. And, in many of these analyses, the transition from indirect to direct is not so starkly delineated; there is often a rather broad energy range where the data might be contributing to the linear regression fit for both values – even though each line would have to be built from the assumption of having a dominant contribution from one type or the other.

We address this situation by using the best optical data possible for silicon, an indirect-band-gap material, as a proxy for well crystallized thin film indirect-gap materials. This allows us, eventually, to assess the limits that might be found for distinguishing the indirect and direct band edges and key data signatures that help quantify these assessments. Figure 5 (next page) shows a band-diagram for silicon [21-23]. Silicon is an indirect band-gap material where the indirect transition goes from the center of the Brillouin Zone (Γ) and requires the simultaneous absorption or emission of a phonon in one of the <100> directions of the lattice (denoted X), resulting in the slanted vector shown. Direct optical transitions happen vertically, but will require larger energy for silicon because the electron must be excited from a filled state into an available

state at higher energy. One such direct transition is shown. Interestingly, the earliest direct transitions for silicon happen up near 3 eV, which is quite a bit larger than the room temperature band-gap of around 1.12 eV. Figure 6 (next page) shows the rapid rise in absorption coefficient for energies above 3 eV and much lower values between 1.1 and 3 eV (associated with indirect optical transitions).

In the basic understanding of how the energy levels vary with electron momentum (k) result in shapes that often have parabolic shapes at symmetry points (for example at the valence band edge and other high symmetry points. And, this parabolic shape is the mathematical reason that the Tauc exponents were found to be the values listed above in equation (1).

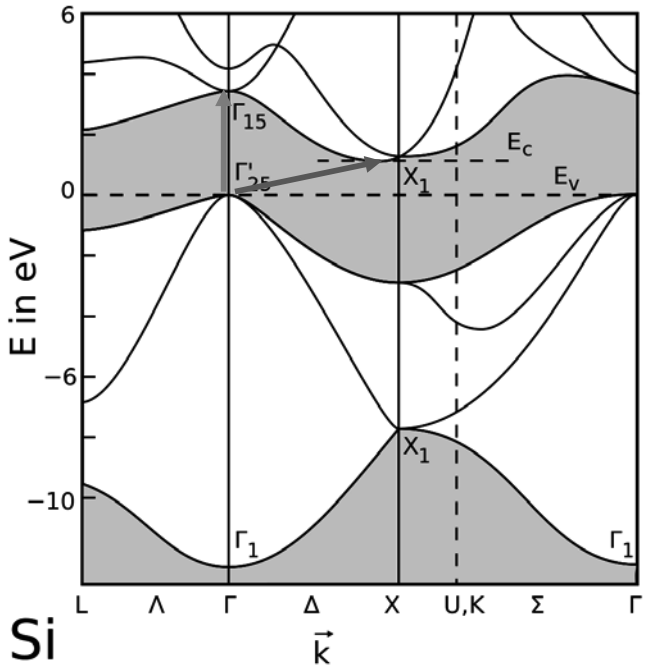

Figure 5: Band structure for silicon showing the indirect transition that is responsible for the onset of absorption and a direct transition (blue arrow) that occurs at certain higher energy values (figure adapted from Chelikowsky [21]).

Knowing that silicon is an indirect material we immediately move to replotting the data using the ½-exponent (the n=2 case from Equation 1, above). Figure 7 (next page) shows this plot for photon energies up to 3 eV (before the sharp rise caused by direct transitions). It can be seen that a large segment of the data can be well represented by a moderately straight light, supporting Tauc's formalism for an indirect material. The data deviate upward from the nominally-linear part for energies above about 2.2 eV, which could be expected for the following reasons. First, the E-vs-k energy level lines must be parabolic to yield the exponents derived by

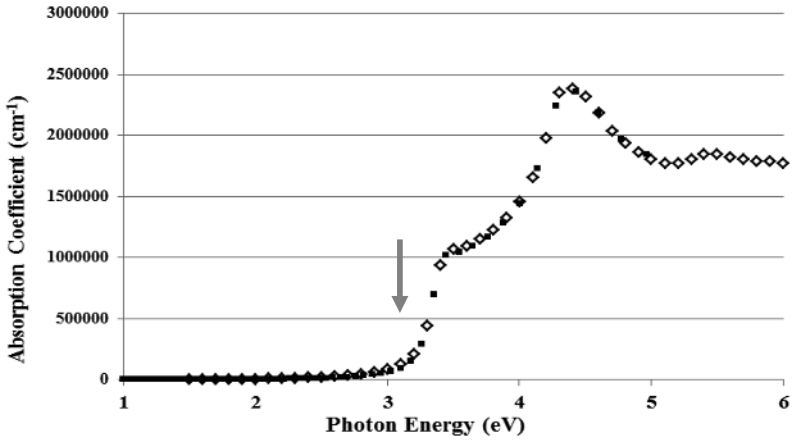

Figure 6: Dispersion of absorption coefficient at 300°K for intrinsic silicon. Open symbols are data from Aspnes and Studna[24]; filled symbols are from Green and Keevers[25]. The rapid rise above 3 eV (indicated by the arrow) comes from the onset of direct transitions.

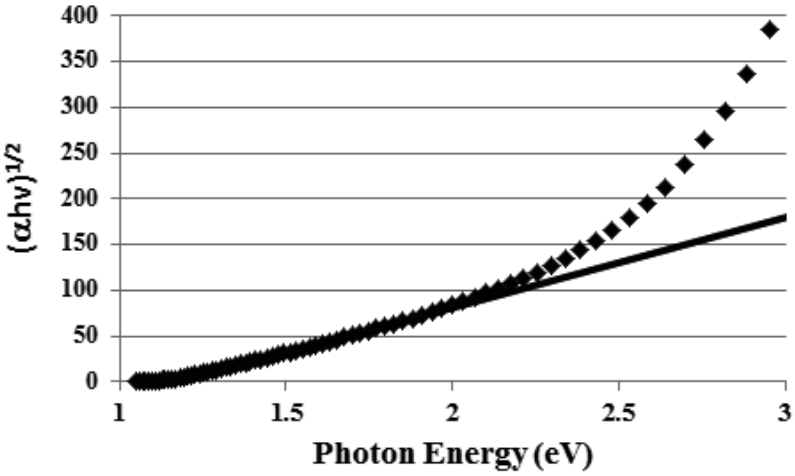

Figure 7: Overview Tauc plot examination of the single crystal silicon absorption data of Green and Keevers[25]. Data are plotted up to 3 eV showing the long region of good linearity (from the band edge up to about 2.2 eV) and including the higher energy range where there is strong upward deviation from the ideal ½-power indirect correspondence.

Tauc. However, as seen in Figure 5, there may be a central region of nice parabolic shape, but there is usually inflection and leveling of the lines at some point. This indicates a higher density of states, which will translate into a larger differential absorption effect as we evaluate at increasingly large photon energies. It is also possible that we might start to have the early contributions from direct transitions which will be added to the basic starting indirect behavior. Further, we might have other secondary indirect transitions that might begin to add into the main transition that was illustrated as the mechanism in Figure 5. All of these factors will lead to an upward deviation of the Tauc plot at higher energy values. For the present discussion we confine our assessment to the region that is nicely linear.

Since we are especially interested in using the Tauc method to extrapolate back to the X-axis to solve for the indirect optical band-gap, we turn our attention to the lower left part of this curve, as shown in Figure 8. Interestingly, the indirect plot displays two linear regions indicating two different indirect transitions. These correspond to the cases where a phonon needs to be either (A) absorbed from the lattice or (B) is emitted into the lattice[26]. Case A has the shallower line, which intersects at (Egap – Eph), where Eph is the energy of the phonon vibration. Case B, with the steeper line, intersects at (Egap + Eph). The intersection points found here were 1.0490 ± 0.0094 and 1.1351 ± 0.0012, resulting in a nominal phonon energy of 0.043 ± 0.010 eV, which is quite consistent with experimental and modeling studies of the phonon dispersion in silicon[27-30].

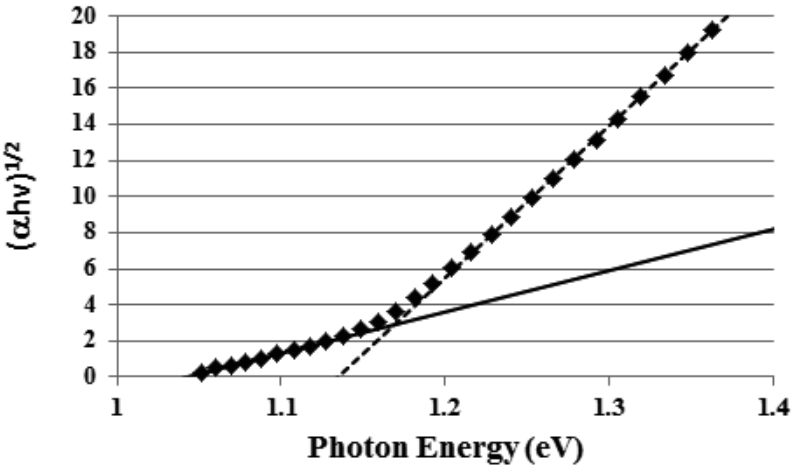

Figure 8: Close-up of the near-edge region of the indirect Tauc plot for silicon [25]. Two different indirect regions are found: the solid line includes phonon absorption and the dashed line is for phonon emission.

While the single crystal data for silicon can be resolved into both phonon absorption and emission processes, it would be rather unusual for thin film optical absorption data to extend down this low and thus band-gap values derived by the Tauc method are usually reported without acknowledging the phonon processes inherent in these indirect transitions. Notably, then,

experimental Tauc plots are derived from the steeper sloped region (case B) that extends to higher absorption coefficient values.

Now, we focus our attention more broadly to assess our ability to extrapolate from more limited optical absorption data. This is required because thin film samples may not be thick enough to accurately measure the relatively small absorption coefficient values covered in Figure 8. For example, if we had a 200 nm film that had α = 1000 cm^{-1} at a certain wavelength, then still 98% of the light intensity would be transmitted, so depending on the film quality and the spectrometer used it might be difficult to measure that α value. Figure 9 signifies this limit showing that the larger α values will necessarily be more accurate (for a given film thickness

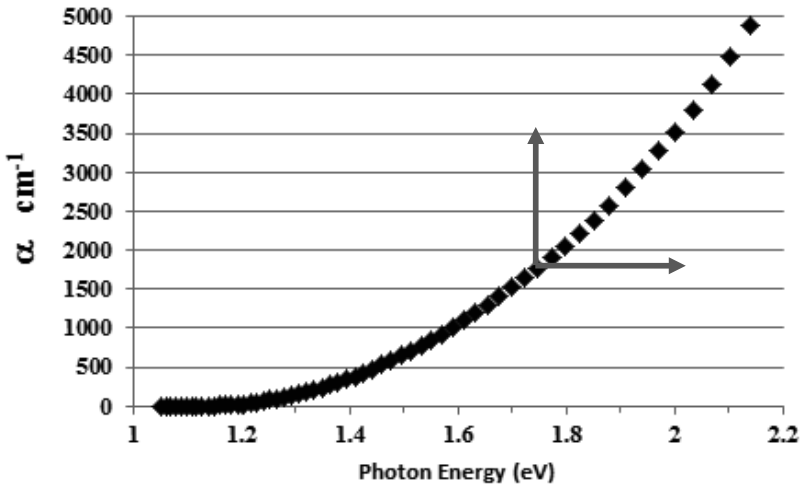

Figure 9: Absorption coefficient values for silicon in the region from 1.05 through 2.20 eV [25]. The parabolic shape associated with an indirect transition is clear.

and spectrometer) and that the linear regression of the type shown in Figures 7 and 8 would most sensibly be done for the photon energies above some threshold. This issue is further complicated by the fact that many thin films may be defective to some degree and exhibit sub-band-gap absorption or band tailing, the "Urbach tail mentioned above [19]. These states are usually described with an exponential function having absorption coefficient values that remain well above zero quite further into the gap.

Now, referring back to Figure 7, we test the degree of linearity that would be found (and the extrapolated band-gap) if we were fitting a Tauc plot using data only above some selected lower limit absorption coefficient value and working upwards with the more confident data. For simplicity we take a linear regression that is based on 10 adjacent data points (though one would normally select that fitting window to be as large as reasonable for the existing data set, as discussed before in our direct-gap work[1]). Figure 10 (next page) gives the band-gaps and extrapolated confidence interval values found when we do each of the possible 10-adjacent-point linear regressions for the silicon data in Figure 7. The X-axis in Figure 10 is draw to correspond to the photon energy of the left-most data point used in the linear regression. The typical width of

energy values thus used for these test fits spanned about 0.1 eV at the lower energies and grew to about 0.3 eV when fitting at the higher energies. For example, referring back to Figure 4, the 10-point-regression that starts at 1.1 eV (on the flatter line) will extend well into the area on the steeper line, resulting in a somewhat poorer fit.

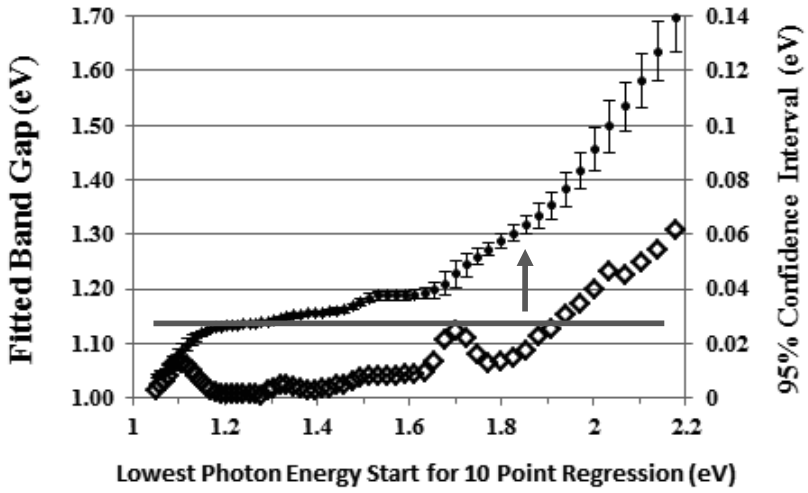

Figure 10: Fitted indirect band-gap values for each 10-point linear regression window (small circles) including their mathematical confidence interval based on the variability within each 10-point window. The specific values of mathematical confidence interval are referenced to the right side scale (open diamonds).

So, if we were working with a thin coating of single crystal silicon we might have trouble measuring the smaller α values and could be forced to fit a linear regression through a part of the data that appeared linear but might already be including some of the data from incipient direct transitions, for example, or a wider range of indirect transitions. It is no surprise that if we use a fitting window that is at higher energies then the confidence interval gets gradually wider (because we are extrapolating further). Overlaid onto Figure 10 is a flat line at the indirect band-gap value (determined using the steeper line from Figure 8, above). The higher-photon-energy-base fitted lines (those using the larger absorption coefficient values) find band-gap intercept values that are much higher above the Eg value than would have been predicted by the linear-regression's projected confidence interval. As noted above, this is partly attributable to the change in curvature for the E-vs-k energy levels in Figure 5, which provides for slightly more absorption at higher photon energies and slight upward curvature of the $\alpha(hv)$ curve, compared with what would have been predicted by the lowest energy threshold responses. Thus, we find that systematic error might be relatively large when associated with fitting using a range of energy values somewhat far from the lowest absorption coefficient values. The R^2 values and calculated confidence intervals must be considered the precision of the measurement, not the accuracy.

DISCUSSION

Application of the Tauc method to thin films is then especially strongly influenced by the thickness of the coating being measured. If the coating is especially thin then only the larger α values are sampled leading to a likely systematic bias that over-estimates the band-gap value. And, since the α values associated with those indirect transitions can be rather small it is questionable whether indirect materials can be fairly evaluated using this method. For example, as shown with silicon, there will always be some form of direct transition that eventually overshadows the indirect transition.

CONCLUSIONS

Direct and indirect band-gap model material data have been examined to help understand in greater detail the limitations of the Tauc method when applied to thin film materials. Direct-gap materials have been shown to have band-gap accuracy in the 1% range when considering the whole range of error contributions that might be important for real thin film sample preparation and characterization. A figure-of-merit has been applied that can help differentiate datasets that might have more mathematical likelihood of providing high accuracy band-gap values. This figure of merit is also applicable to indirect materials, but the absorption coefficient values found near the indirect-gap are frequently too low to be measured with typical samples, raising the question of whether good indirect-gap determinations can be made with the Tauc method.

ACKNOWLEDGEMENTS

Funding for this research was generously provided by the Malcolm G. McLaren fund at Rutgers University.

REFERENCES

1. Viezbicke, B.D., S. Patel, B.E. Davis and D.P. Birnie, *Evaluation of the Tauc Method for Optical Absorption Edge Determination: ZnO Thin Films as a Model System.* Physica Status Solidi, B, 2015. **252**(8): p. 1700-1710.
2. Tauc, J., R. Grigorovici and A. Vancu, *Optical properties and electronic structure of amorphous germanium.* Physica Status Solidi, 1966. **15**: p. 627-637.
3. Davis, E.A. and N.F. Mott, *Conduction in non-crystalline systems V. Conductivity, optical absorption and photoconductivity in amorphous semiconductors.* Philosophical Magazine, 1970. **22**: p. 903.
4. Mott, N.F. and E.A. Davis, *Electronic processes in non-crystalline materials*. 2nd ed. 1979: Clarendon Press (Oxford and New York).
5. Ozgur, U., Y.I. Alivov, C. Liu, A. Teke, M.A. Reshchikov, S. Dogan, V. Avrutin, S.J. Cho and H. Morkoc, *A comprehensive review of ZnO materials and devices.* Journal of Applied Physics, 2005. **98**(4).
6. Ozgur, U., D. Hofstetter and H. Morkoc, *ZnO Devices and Applications: A Review of Current Status and Future Prospects*. Proceedings of the Ieee, 2010. **98**(7): p. 1255-1268.
7. Rodnyi, P.A. and I.V. Khodyuk, *Optical and luminescence properties of zinc oxide (Review).* Optics and Spectroscopy, 2011. **111**(5): p. 776-785.
8. Gupta, T.K., *APPLICATION OF ZINC-OXIDE VARISTORS.* Journal of the American Ceramic Society, 1990. **73**(7): p. 1817-1840.
9. Bagnall, D.M., Y.F. Chen, Z. Zhu, T. Yao, S. Koyama, M.Y. Shen and T. Goto, *Optically pumped lasing of ZnO at room temperature.* Applied Physics Letters, 1997. **70**(17): p. 2230-2232.
10. Mitra, P., A.P. Chatterjee and H.S. Maiti, *Chemical deposition of ZnO films for gas sensors.* Journal of Materials Science-Materials in Electronics, 1998. **9**(6): p. 441-445.
11. Mitra, P., A.P. Chatterjee and H.S. Maiti, *ZnO thin film sensor.* Materials Letters, 1998. **35**(1-2): p. 33-38.

12. Platzer-Bjorkman, C., T. Torndahl, D. Abou-Ras, J. Malmstrom, J. Kessler and L. Stolt, *Zn(O,S) buffer layers by atomic layer deposition in Cu(In,Ga)Se-2 based thin film solar cells: Band alignment and sulfur gradient.* Journal of Applied Physics, 2006. **100**(4).
13. Abb, M., B. Sepulveda, H.M.H. Chong and O.L. Muskens, *Transparent conducting oxides for active hybrid metamaterial devices.* Journal of Optics, 2012. **14**(11).
14. Thomas, D.G., *The exciton spectrum of zinc oxide.* Journal of Physics and Chemistry of Solids, 1960. **15**(1-2): p. 86-96.
15. Srikant, V. and D.R. Clarke, *On the optical band gap of zinc oxide.* Journal of Applied Physics, 1998. **83**(10): p. 5447-5451.
16. Jellison, G.E. and L.A. Boatner, *Optical functions of uniaxial ZnO determined by generalized ellipsometry.* Physical Review B, 1998. **58**(7): p. 3586-3589.
17. Allsopp, H.J. and J.P. Roberts, *Non-stoichiometry of zinc oxide and its relation to sintering: Part 1 - Determination of non-stoichiometry in zinc oxide.* Transactions of the Faraday Society, 1959. **55**: p. 1386-1393.
18. Wang, M.D., D.Y. Zhu, Y. Liu, L. Zhang, C.X. Zheng, Z.H. He, D.H. Chen and L.S. Wen, *Determination of thickness and optical constants of ZnO thin films prepared by filtered cathode vacuum arc deposition.* Chinese Physics Letters, 2008. **25**(2): p. 743-746.
19. Urbach, F., *The Long-Wavelength Edge of Photographic Sensitivity and of the Electronic Absorption of Solids.* Physical Review 1953. **92**: p. 1324.
20. Vogel, D., P. Krueger and J. Pollmann, *Self-interaction and relaxation-corrected pseudopotentials for II-VI semiconductors.* Physical Review, B, 1996. **54**(8): p. 5495-5511.
21. Chelikowsky, J., *Silicon in all its forms.* MRS Bulletin, 2002. **27**(12): p. 951-960.
22. Chelikowsky, J.R. and M.L. Cohen, *Electronic structure of silicon.* Physical Review B, 1974. **10**(12): p. 5095-5107.
23. Chelikowsky, J.R. and M.L. Cohen, *Nonlocal pseudopotential calculations for the electronic structure of eleven diamond and zinc-blende semiconductors.* Physical Review B, 1976. **14**(2): p. 556-582.
24. Aspnes, D.E. and A.A. Studna, *Dielectric Functions and Optical-Parameters of Si, Ge, GaP, GaAs, GaSb, InP, InAs, and InSb from 1.5 to 6.0 eV.* Physical Review B, 1983. **27**(2): p. 985-1009.
25. Green, M.A. and M.J. Keevers, *Optical-Properties of Intrinsic Silicon at 300 K.* Progress in Photovoltaics, 1995. **3**(3): p. 189-192.
26. Kasap, S. and P. Capper, *3. Optical Properties of Electronic Materials: Fundamentals and Characterization*, in *Springer Handbook of Electronic and Photonic Materials*, S. Kasap and P. Capper, Editors. 2006, Springer: New York, NY. p. 47-77.
27. Yin, M.T. and M.L. Cohen, *Abinitio Calculation of the Phonon-Dispersion Relation - Application to Si.* Physical Review B, 1982. **25**(6): p. 4317-4320.
28. Nilsson, G. and G. Nelin, *Study of the Homology between Silicon and Germanium by Thermal-Neutron Spectrometry.* Physical Review B, 1972. **6**(10): p. 3777-3786.
29. Tubino, R., L. Piseri and G. Zerbi, *Lattice Dynamics and Spectroscopic Properties by a Valence Force Potential of Diamondlike Crystals: C, Si, Ge, and Sn.* Journal of Chemical Physics, 1972. **56**: p. 1022.
30. Sui, Z.F. and I.P. Herman, *Effect of Strain on Phonons in Si, Ge, and Si/Ge Heterostructures.* Physical Review B, 1993. **48**(24): p. 17938-17953.

INVESTIGATION OF PYROAURITE-TYPE ANIONIC CLAY-DERIVED MIXED OXIDES WITH VARIOUS COMPOSITIONS

Jonathan Gabriel[1], Aarti Patel[1], Ewul Ebenezer[2], Andrei Jitianu[2,3*], Mihaela Jitianu[1*]

[1]William Paterson University, Department of Chemistry, 300 Pompton Road, Wayne, NJ 07470
[2]Lehman College – City University of New York, Department of Chemistry, Davis Hall, 250 Bedford Boulevard West, Bronx, NY 10468
[3]PhD. Program in Chemistry and Biochemistry, The Graduate Center of the City University of New York, New York, NY 10016, USA
* Corresponding author

ABSTRACT

Pyroaurite, a natural mineral with the formula $Mg_6Fe_2(OH)_{16}(CO_3)\bullet 4H_2O$ belongs to the large class of anionic clays and contains positively charged Mg(II) and Fe(III) layers alternating with layers containing carbonate ions and water molecules. Mesoporous pyroaurite-type anionic clays with different Mg/Fe molar ratios (1:3-5:2) have been successfully synthesized by coprecipitation method. The corresponding oxides were obtained by thermal treatment at 550ºC and 900ºC. The effect of samples' composition on the structural and textural characteristics of starting pyroaurite and corresponding oxides has been investigated. The crystallite size, the phase composition and BET surface area values were found to strongly depend on the Mg/Fe ratios. TEM micrographs revealed that sheet-like morphology of the high Mg(II) content samples was preserved at 550ºC, due to a special decomposition mechanism of pyroaurite.

INTRODUCTION

Pyroaurite and sjögrenite compounds are two closely similar minerals that are two stacking modifications of typical composition $Mg_6Fe_2(OH)_{16}(CO_3)\bullet 4H_2O$[1]. Their structure is based on $Mg(OH)_2$ – brucite-like layers, in which some of the Mg(II) ions are randomly substituted by Fe(III) leading to positively charged layers, their charge being compensated by carbonate (CO_3^{2-}) ions, located in the interlayer region along with water molecules. Those two minerals are polytypes that differ only in layer stacking, the rhombohedral pyroaurite (3R polytype) and the hexagonal sjögrenite (2H polytype) creating two subgroups that belong to the much larger class of layered compounds called anionic clays[1,2]. The anionic clays have been largely investigated due to their applications as anion exchangers, catalysts and catalysts precursors, adsorbents and UV stabilizers, just to mention a few[3]. Cationic compositions along with specific characteristics of the interlayer play an important role in numerous applications[4].

Lately, anionic clays derived mixed oxides have been proved to be effective in desulfurization processes[5,6]. A high level of sulfur in fuels is not desired due to the formation of SO_x from the combustion of sulfur-containing compounds. SO_x causes acid rain and this in turn causes damage to buildings and affects dramatically the ecosystem balances[5]. Moreover, sulfur compounds poison the noble metal catalysts used in automobile catalytic converters and this leads to fuel to be incompletely combusted and consequently to emissions of incompletely combusted hydrocarbons, carbon monoxide, nitrogen oxides[7]. An interesting promising potential application of derived oxides is as absorbents for sulfur based compounds, due to their basic properties[7]. So far, different types of absorbents have been used, such as supported metal oxides (support is typically alumina or carbon), mixed metal oxides, metal ion-exchanged zeolites. While all those materials are quite effective, the main difference that anionic clays derived

oxides bring is that they show very good promise to work at ambient temperature, as opposed to elevated temperatures required for the other absorbents[7]. Based on the particularities of the layered structure and decomposition mechanism, the metal oxides have increased basicity relative to the clay precursor[7]. Due to these properties, anionic clays derived mixed oxides have been top candidates for absorbent applications for acidic species, such as CO_2, NO_x and SO_x, mercaptans, organosulfides, CS_2 and thiophene[7].

Surface properties and morphology of the oxides, and subsequently their absorption capacities, catalytic activity and efficiency as supporting material is strongly dependent on their chemical composition. The mixed oxides obtained after such a calcination process have very interesting properties, such as: high surface area, basic properties, formation of homogeneous mixture of oxides with very small crystallite size[8]. The key to these special characteristics resides in the distinctiveness of anionic clays decomposition that occurs in two steps: first, dehydration followed by the collapse of the lamellar structure[9]. The intermediate structure preserves the layered characteristics of anionic clays, and the overall topology is unchanged. Second, the decomposition of the anions and collapse of the structure leads to formation of a new 3-dimensional network[8]. The increase of surface area occurs together with this contraction of the layers and is possibly related to the associated strain development in the material. The calcination temperature is the key parameter to be controlled in this process.

This present work describes synthesis and characterization of a series of mixed oxides derived from synthetic phases structurally related to pyroaurite minerals. Pyroaurite-like materials with three different Mg/Fe molar ratios have been synthesized by precipitation and then calcined at two different temperatures. The structural and morphological characterization of the mixed oxides and their precursors indicated differences in structure, thermal behavior and surface characteristics as a function of the cation composition.

EXPERIMENTAL

Materials

All materials (Reagent grade) were used as received, without further purification. All solutions have been prepared with deionized water. Magnesium nitrate hexahydrate, >99% and iron nitrate nonahydrate, >98% (Sigma Aldrich) have been used for pyroaurite synthesis, along with sodium carbonate >99.5% and sodium hydroxide >98% (Sigma Aldrich).

Sample preparation

The pyroaurite-type samples with Mg/Fe molar ratios of 1:3, 2:1 and 5:2 were synthesized by the coprecipitation method at a constant pH=8. An 0.5M aqueous solution of $Mg(NO_3)_2 \cdot 6H_2O$ and $Fe(NO_3)_3 \cdot 9H_2O$ containing Mg(II) and Fe(III) in the required ratios was added dropwise under mechanical stirring (600 rpm) simultaneously with a basic solution containing 0.5M Na_2CO_3 and 0.5M NaOH in a reaction vessel at a constant pH=8. The reaction vessel was equipped with a heating mantle that maintained a constant temperature of 60°C during the reaction. Once the reaction was completed, the samples were aged for an hour at 60°C, then filtered, washed at room temperature with deionized water, and subsequently dried at 110°C overnight. Thermal treatment was carried out at 550°C and 900°C, respectively, at a heating rate of 5°C/min. Samples were kept at each temperature for 1h.

Sample characterization

Powder X-Ray diffraction patterns were recorded using a Rigaku Ultima IV Theta-Theta with a Cu Kα radiation (1.54056 Å) in the 2θ range 5-80°, step size 0.02 at a speed of 0.1°/min. For the determination of the average crystallite size, Williamson-Hall method has been employed:

$$\beta_L = K\lambda/L\cos\theta$$

where λ is the wavelength (CuKα), β_L is the size broadening, θ the Bragg angle.

The FTIR Spectra were recorded in the ATR mode in the range 4000-400 cm^{-1} using a Nicolet FTIR IS10 spectrometer equipped with the Smart Orbit HATR attachment (Thermo Scientific) at a resolution of 4 cm^{-1}.

Combined thermal analysis measurements (thermogravimetry TG and differential thermal analysis DTA) were carried out with a Seiko EXTAR TGA/DTA 6200 thermal analyzer using platinum crucibles. The measurements were carried out under flowing air at a heating rate of 5°/min up to 1000°C.

The surface area and porous structure of the samples was determined by absorption/desorption of nitrogen at 77K using a Tristar II 3020 BET surface analyzer. Samples were previously outgassed at 110°C (pyroaurite samples) and 300°C (oxide samples), respectively, in a nitrogen flow overnight. Surface areas were determined using the Brunauer-Emmet-Teller (BET) method and the pore size distribution was evaluated by nitrogen/helium mixture desorption using Barrett, Joyner & Halenda (BJH) method.

Transmission electron microscopy was carried out by means of a Hitachi Model 7700 under high resolution at an acceleration voltage of 100kV and a current of 10 μa. Samples were prepared on Formvar-coated thick carbon coated 200 mesh copper grid. Micrographs were taken at 50,000x magnification.

RESULTS AND DISCUSSION

The observed peaks in the X-Ray diffraction patterns (Figure 1) indicate well-crystallized samples for Mg/Fe ratios of 2:1 and 5:2 (JCPDS card 01-086-0181). A rather amorphous nature of the sample with Mg/Fe ratio of 1:3 is indicated by very broad and low intensity peaks (Figure 1 insert), almost not noticeable when overlaying all the patterns. For all samples, the diffraction peaks can be indexed with the space group *R3m*, revealing that the samples are crystallized in a rhombohedral structure characteristic to the pyroaurite polytype[1]. No secondary crystalline phases such as $Mg(OH)_2$ or $Fe(OH)_3$ have been identified in the diffractograms of the prepared samples.

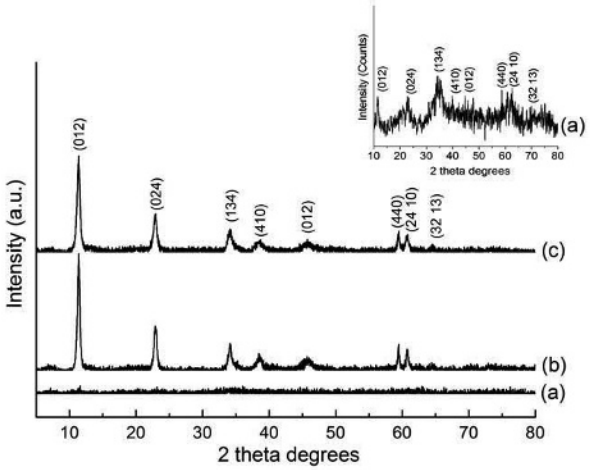

Figure 1. X-Ray diffraction patterns of pyroaurite samples:
a. Mg/Fe 1:3 (Insert), b. Mg/Fe 2:1, c. Mg/Fe 5:2;

Noteworthy changes are observed for the X-Ray diffraction patterns of the samples calcined at 550ºC (Figure 2). The well-defined pyroaurite peaks for the samples with Mg/Fe molar ratios 2:1 and 5:2 (Figure 1b, c) are replaced by less intense broader peaks (Figure 2b, c), suggesting a nanocrystalline material with very small nanoparticles. This strong change in the X-Ray patterns is an indication of the fact that thermal decomposition of pyroaurite occurs topotactically via a disordered structure[9]. Conversely, the sample with Mg/Fe ratio of 1:3 displays high-intensity narrow peaks, suggesting larger well crystallized particles (Figure 2a). The periclase Mg(Fe)O (JCPDS card 01-076-2585) was mainly detected for samples with Mg/Fe ratios 2:1 and 5:2 along with a small amount of magnesioferrite, $MgFe_2O_4$ spinel structure $MgFe_2O_4$ (JCPDS card 01-074-8054). These results reveal that the mixed oxides may primarily have a brucite-type structure with Fe(III) randomly distributed in the octahedral sites. Also, it is possible to consider the

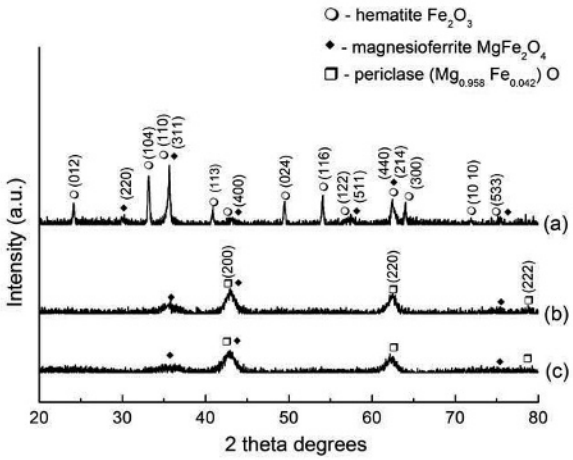

Figure 2. X-Ray diffraction patterns for the oxides obtained at 550ºC:
a. Mg/Fe 1:3, b. Mg/Fe 2:1, c. Mg/Fe 5:2.

formation of Mg(Fe)O solid solutions, based on the Fe(III) ion being smaller (0.49 Å) than Mg(II) (0.72 Å)[10]. The FTIR spectra support these results and will be discussed in detail later in the paper. The diffraction pattern of the sample with Mg/Fe ratio of 1:3 is very different from the ones of the samples with Mg/Fe ratios of 2:1 and 5:2. The lines reveal formation of mainly hematite Fe_2O_3 phase (JCPDS card 01-071-5088) along with a small quantity of magnesioferrite. This sample has the highest Fe(III) content and it appears that by decomposition it develops mainly a Fe(III)-only containing phase. With a further increase of calcination temperature to 900ºC, the broad peaks for samples with Mg/Fe ratios of 2:1 and 5:2 narrow and become more intense, indicating the presence of crystalline samples (Figure 3b,c). Peaks for the Fe(III)-rich sample (Figure 3a) with Mg/Fe 1:3 become sharper and more intense, as well, suggesting that crystallinity increases with temperature for this sample. No additional oxide phases have been identified at 900ºC compared to the ones at 550ºC.

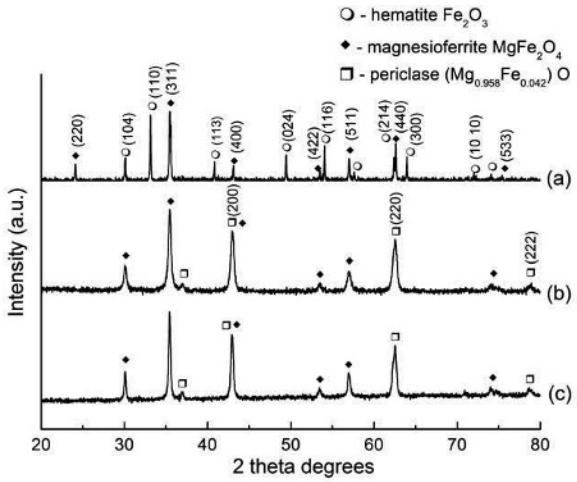

Figure 3. X-Ray diffraction patterns for the oxides obtained at 900ºC:
a. Mg/Fe 1:3, b. Mg/Fe 2:1, c. Mg/Fe 5:2.

Table I. Crystallite size for the Mg/Fe 1:3 sample and derived oxide phases obtained at, 550º and 900ºC.

Sample	Crystallite size (Å)				
	As prepared	Oxides at 550ºC		Oxides at 900ºC	
	Pyroaurite	Hematite Fe_2O_3	Magnesioferrite $MgFe_2O_4$	Hematite Fe_2O_3	Magnesioferrite $MgFe_2O_4$
Mg/Fe = 1:3	3.1	102	865	563	900

Table II. Crystallite size for the Mg/Fe 2:1 and Mg/Fe 5:2 samples and derived oxide phases obtained at 550º and 900ºC.

Sample	Crystallite size (Å)				
	As prepared	Oxides at 550ºC		Oxides at 900ºC	
	Pyroaurite	Periclase $(Mg_{0.958}Fe_{0.042})O$	Magnesioferrite $MgFe_2O_4$	Periclase $(Mg_{0.958}Fe_{0.042})O$	Magnesioferrite $MgFe_2O_4$
Mg/Fe = 2:1	141	50	23	75	31
Mg/Fe = 5:2	155	29	5.92	81	36

The crystallite sizes as determined from XRD measurements are reported in Tables I and II, for the sample with Mg/Fe ratio of 1:3 and samples with Mg/Fe ratios of 2:1 and 5:2, respectively. The evolution of crystallite sizes is shown for all phases formed. An interesting behavior is found for the sample with Mg/Fe 1:3 and the derived two oxide samples. A very small crystallite size (0.3 nm) was found in the starting pyroaurite sample, while slightly

larger, within the small nanoparticles domain, was identified for the samples with higher Mg/Fe ratio (14-15 nm). The evolution of the crystallite size with temperature is very different, depending on the Mg/Fe ratio, a sharp increase for both phases at 550ºC and further at 900ºC is displayed by the Fe(III)-rich sample. For the samples with Mg/Fe ratios of 2:1 and 5:2, an actual decrease in crystallite size was found for the oxide phases at 550ºC, followed by a moderate increase at 900ºC. This leads to the suggestion that the decomposition mechanism for samples is different, depending on the Mg/Fe ratio, as it will be described in the next section.

The thermal decomposition was investigated by TGA / DTA experiments (Figure 4). All samples start to lose weight from room temperature up to 550ºC. The thermal decomposition consists of two clear steps for samples with Mg/Fe ratios of 2:1 and 5:2 (Figure 4a,b). The first step corresponds to the loss of physisorbed and interlayer water[9] and is accompanied by an endothermal effect on the DTA curve at 170 and 180ºC, respectively. The second decomposition step relates to the loss of carbonate ions and the hydroxyl groups in the brucite-type layer[9], with two clear endothermal effects on the DTA curve at 290-305ºC and 354-357ºC, respectively. The thermal decomposition of the sample with Mg/Fe ratio of 1:3 is different (Figure 4c). Decomposition occurs in one step, basically a continuous weight loss was observed from room temperature till around 550ºC. The DTA curve for this sample only shows two endothermal effects in the temperature range 100-360ºC, one at 160ºC, and the second one at 345ºC. The absence of the peak at 290-300ºC suggests a disordered interlayer structure in those samples, leading to a gradual weight loss during heating. The amorphous nature of this sample leads to different decomposition features. Two more additional endothermal effects were observed for this sample with Mg/Fe ratio of 1:3, at 468ºC and at 588ºC. Those effects are not accompanied by weight loss, thus they may be attributed to phase transformation with temperature. Since the latter effects were not observed for the other two pyroaurite samples, it is an indication that the Fe(III)-rich sample with Mg/Fe ratio of 1:3 contains another phase besides the pyroaurite that could not be detected by X-Ray diffraction due to lack of crystallinity. Those findings for the Fe(III)-rich sample correlate well with the different phase composition identified by X-Ray diffraction at 550ºC and beyond.

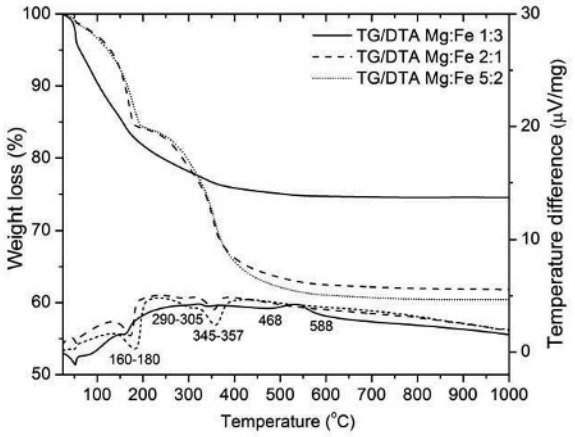

Figure 4. Thermal analysis of the pyroaurite samples.

FTIR analysis (Figure 5) reveals characteristic absorptions for carbonate-containing pyroaurite. All spectra show absorption bands at ~ 3380 cm^{-1}, attributed to hydroxyl stretching bands (υOH)[11], and located at lower wavenumbers than in simple hydroxides with no hydrogen bonds (> 3600 cm^{-1}). The band at 1640 cm^{-1} is attributed to the deformation of (δHOH) angle of water molecule[3]. Vibrational spectroscopy is widely applied in investigating the structure of the interlayer anion, in this present case, carbonate. As reported in the literature for anionic clays[12,13], carbonate anions in the interlayer are generally in a symmetric environment, characterized by a D_{3h} planar symmetry, with three IR active absorption bands as in the case of free carbonate anion, as follows: 1360 cm^{-1} (υ_3), 880 cm^{-1} (υ_2), 680 cm^{-1} (υ_4). Our spectra show an intense band situated at 1350 cm^{-1} (υ_3) along with the one at 680 cm^{-1} (υ_4), thus showing the presence of highly symmetrical D_{3h} carbonate anions. Yet, the presence of the band at 1470 cm^{-1} in the spectra of our samples with Mg/Fe ratios of 1:3 and 2:1 is attributed to a lowering in the symmetry of the carbonate anion to C_{2v} or C_s, as well as to a disordered nature of the interlayer[14,15]. The lowering symmetry of the carbonate ions is due to the restricted environment into which the anions are placed and to various intensity of the hydrogen bonds[3]. It appears that the intensity of the band at 1470 cm^{-1} decreases from the Fe(III)-rich sample with Mg/Fe ratio of 1:3 to the sample with Mg/Fe ratio of 2:1, suggesting that the lower symmetry of carbonate ions and the interlayer disorder becomes less significant in samples with higher Mg to Fe ratios. For the sample with Mg/Fe ratio of 5:2, only highly symmetric carbonate ions were identified (only the band at 1350 cm^{-1} is present). The absorption band at 550 cm^{-1} in the spectra of samples with Mg/Fe ratios of 2:1 and 5:2 is attributed to Mg-O vibrations of the brucitic layer[1]. This band is not very visible for the Fe(III)-rich sample, due to a very low Mg(II) content.

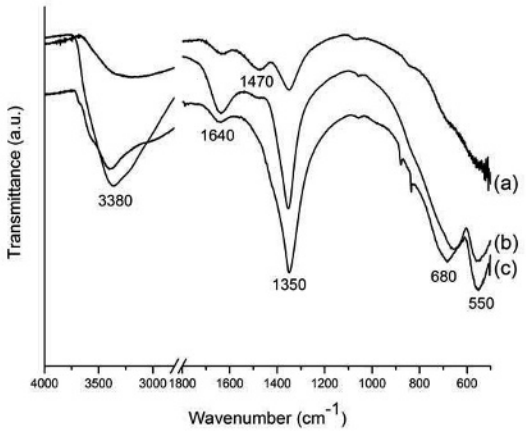

Figure 5. FTIR spectra of pyroaurite samples. a. Mg/Fe 1:3, b. Mg/Fe 2:1, c. Mg/Fe 5:2.

The FTIR spectra at 550ºC and 900ºC (Figure 6) show conversion of the pyroaurite structures into the corresponding oxides. The interpretation of the spectra is carried out in the light of structures of spinel, Fe_2O_3 and MgO species that have been identified by X-Ray diffraction. "Normal" spinel structures consist in a close-packed arrangement of oxide ions, in which the tetrahedral holes are occupied by the divalent cation (MgO_4 tetrahedra) and the octahedral

holes are occupied by the trivalent cation (FeO_6 octahedra)[16]. In some cases, total or partially "inverse" spinel structure can be formed. In this latter case, all or a part of the divalent cation will become octahedral, substituting part or all of the trivalent cation in the octahedral sites[16]. Hematite Fe_2O_3 consists of a close-packed oxide ions lattice with the Fe(III) in the octahedral holes, creating FeO_6 octahedra[16]. Magnesium oxide MgO is a highly ionic compound that has Mg(II) occupying the octahedral holes of a close-packed oxide ions lattice, creating MgO_6 octahedra[16].

The observed FTIR vibration bands for spinels have been labelled υ_1, υ_2, υ_3 and υ_4 in the succession of decreasing wavenumbers[17]. According to Tarte et al[17]. υ_1, υ_2 have been assigned to vibrations of the lattice of condensed octahedra. υ_3 seems to be related to a complex vibrations involving the participation of both types of cations, tetrahedral and octahedral, while υ_4 has been assigned to some type of vibration involving the tetrahedral cation[17]. FTIR spectra recorded for the oxides at 550ºC and 900ºC are very similar, bands become more defined at the higher calcination temperature, as the oxides crystallinity increases, as found by X-Ray diffraction. Due to the limitation of our instrument, the band due to υ_4 vibration could not be visualized, since it is located below 300 cm^{-1}, below our spectral range of our instrument. Moreover, some spinels do not always display all the bands. For the sample with Mg/Fe ratio of 1:3 calcined at 550ºC, the band at 520 cm^{-1} can be assigned to vibrations of (FeO_6) octahedra in Fe_2O_3[19], while the band at 425 cm^{-1} is assigned to υ_3 vibrations of (MgO_6) octahedra[18]. The shoulder at 473 cm^{-1} can be related to the formation of spinel structure, and assigned to the υ_1 vibrations of (FeO_6) octahedra[18,19] within the spinel structure.

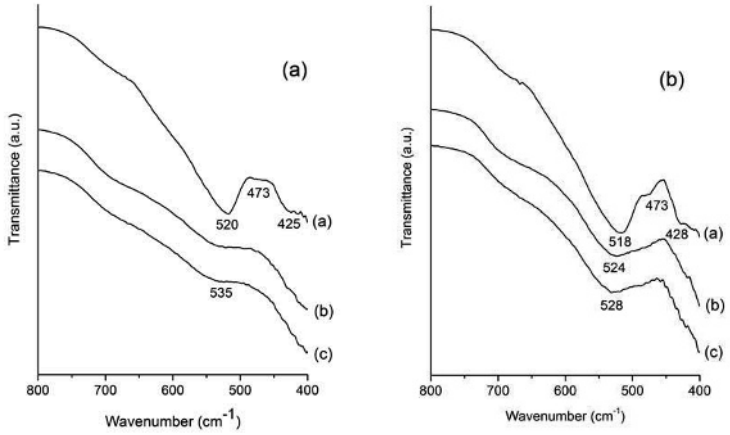

Figure 6. FTIR spectra of a. oxides at 550ºC, b. oxides at 900ºC
a. Mg/Fe 1:3, b. Mg/Fe 2:1, c. Mg/Fe 5:2.

The assignment of these bands is true to the evolution of the sample with Mg/Fe ratio of 1:3 towards 900ºC, the main change being that the shoulder at 473 cm^{-1} intensifies as the spinel structure becomes more crystallized at higher temperature. The band at 518-520 cm^{-1} in the spectra of the oxides corresponding to the sample with Mg/Fe ratio of 1:3 can be due also

to the isolated tetrahedral (MgO_4) groups in the spinel structure[18]. Thus, this band may be very well an overlap between vibrations of (FeO_6) octadedra in Fe_2O_3 structure and vibrations of isolated tetrahedral (MgO_4) groups in the spinel structure. The presence of the υ_3 band due to (MgO_6) octahedra suggests a degree of inversion of the $MgFe_2O_4$ spinel, according to the above mentioned spinel features[16]. Samples with higher Mg/Fe ratios 2:1 and 5:2 mainly exhibit a band at 535 cm^{-1} in the spectra of the oxides obtained at 550ºC that shifts to slightly lower wavenumbers for the oxides at 900ºC. Given the samples composition at 550ºC, which is mainly MgO with small inclusions of Fe(III), this band can be attributed to the highly ionic MgO, for which two bands, one near 550 cm^{-1} and one near 400 cm^{-1} corresponding to the longitudinal optic and transversal optic frequencies, respectively have been reported[17]. Due to the spectral range of our instrument, only the band near 550 cm^{-1}, present at 535 cm^{-1} for the oxides at 550ºC could be identified. As the spinel phase crystallizes better at 900ºC, it is evident that the shift of this band towards lower wavenumbers is related to its overlap with the band due to the isolated tetrahedral (MgO_4) groups in the spinel structure, as mentioned earlier. As the Mg content of the samples increases however from sample with Mg/Fe ratio 2:1 to 5:2, the band shifts towards higher wavenumbers, towards the value for pure MgO.

Table III. BET values for pyroaurite samples and corresponding oxides.

Sample	BET (m^2/g)		
	Pyroaurite	Oxides at 550ºC	Oxides at 900ºC
Mg/Fe = 1:3	262.04	25.96	2.09
Mg/Fe = 2:1	81.21	85.21	28.25
Mg/Fe = 5:2	49.87	94.26	13.97

Different appearances of the nitrogen absorption isotherms as a function of both Mg/Fe ratios and temperature suggest modifications of the porosity characteristics (Figures 7-10). The absorption isotherms of the uncalcined pyroaurite samples are very dissimilar, suggesting modifications of porosity with the Mg/Fe molar ratio (Figure 7). The Fe(III)-rich sample with Mg/Fe molar ratio 1:3 displays an isotherm with particular characteristics. For $p/p_o < 0.35$, multilayer adsorption is implied, and reveals microporous characteristics for this sample. For $0.35 < p/p_o < 0.6$, the isotherm shape suggests the presence of pores with a wide size range, and non-uniform in size and/or shape, as per the irregular form of the hysteresis loop. For $p/p_o > 0.6$, the absorption follows more or less a type IV isotherm[20].

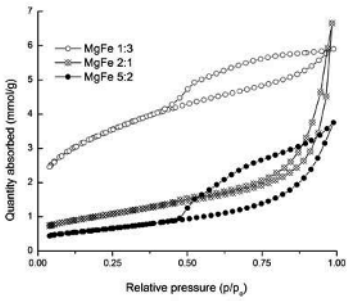

Figure 7. Adsorption isotherms for all pyroaurite samples

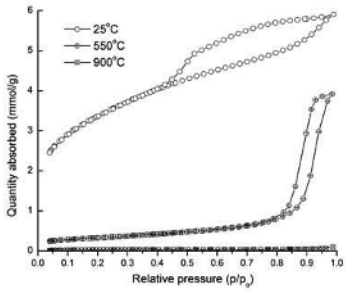

Figure 8. Adsorption isotherms for Mg/Fe 1:3 at all studied temperatures.

Samples with molar ratios Mg/Fe 2:1 and 5:2 show type IV absorption isotherms, with a H3 type hysteresis. Sample with Mg/Fe 2:1 displays however a very narrow hysteresis loop, suggesting more uniformly shaped pores. Conversely, the sample with Mg/Fe 5:2 molar ratio shows a broad H3 hysteresis loop, in the middle range of relative pressure. For this latter sample, for the values of pressure $p/p_o < 0.5$, the expected adsorption process is by formation of a monolayer, while the multilayer adsorption is occurring at high p/p_o. The loop type suggests that aggregates of plate-like particles may form non-uniform slit shaped pores[20].

The evolution of the adsorption isotherms with the temperature up to 900ºC illustrates that samples with Mg/Fe ratios 2:1 and 5:2 maintain the same adsorption characteristics with evolving temperature (Figures 9 and 10), while remarkable changes are occurring for the sample with Mg/Fe 1:3 ratio (Figure 8). For this latter sample, at 550ºC, the shape of the curve is typical for a type IV isotherm with a H1 hysteresis. The isotherm form and the narrow hysteresis loop with almost parallel branches indicate the presence of mesopores with almost regular geometry[20]. The adsorption is very low at 900ºC, the adsorption and desorption branches are close to zero adsorbate value.

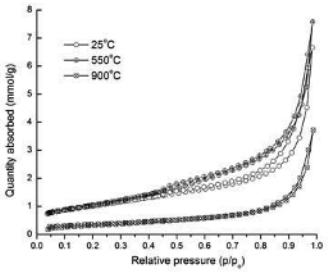

Figure 9. Adsorption isotherms for Mg/Fe 2:1 at all temperatures

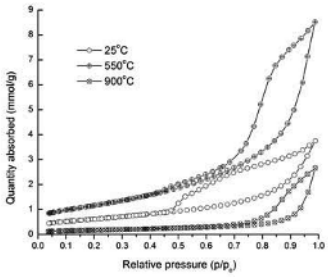

Figure 10. Adsorption isotherms for Mg/Fe 5:2 at all temperatures.

The calculated BET values (Table III) show the highest BET value for the Fe(III)-rich sample before calcination, due to the amorphous nature and very small crystallites, however the BET values for the oxides drops significantly till almost non-porosity is found in the sample at 900ºC. The BET values correlate well with the significant increase in the crystallite size with temperature for this Fe(III)-rich sample. For the other two samples, BET values increased after heat treatment at 550ºC (sample with Mg/Fe ratio 5:2) or remained about the same for the sample with Mg/Fe ratio 2:1 (Table III). As expected, all BET values decreased for the oxides at 900ºC, due to the increase in crystallite size.

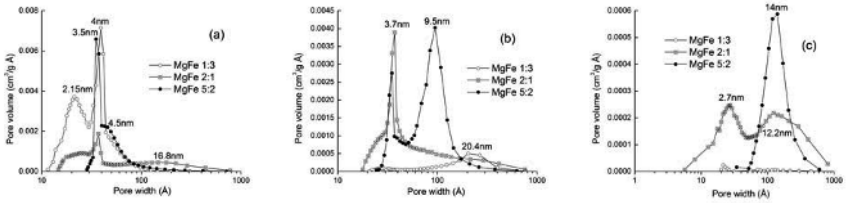

Figure 11. Particle size distribution for all samples:
a. pyroaurite, b. oxides at 550ºC, c.oxides at 900ºC.

One of the most interesting aspects of the anionic clays, including pyroaurite, is the formation of oxides with small crystallite size and high surface area[8] due to their special decomposition mechanism[9], which is the best illustrated by sample with Mg/Fe ratio 5:2. Sample with Mg/Fe ratio 2:1 shows a small increase in BET value at 550ºC, while sample with Mg/Fe ratio 1:3 definitely leads to oxides with low BET values and high crystallite size for 550ºC. It becomes thus clear that the main phase in this sample it is not pyroaurite, but an amorphous, most likely a Fe(III)-rich phase that does decompose by a different mechanism, leading to an accelerated crystallite size. This is supported also by the X-Ray diffraction results that show that the main oxide phase obtained by decomposition of sample with Mg/Fe ratio 1:3 is hematite Fe_2O_3 (Figures 2 and 3).

Pore size distribution (PSD) is mostly bimodal for starting pyroaurite samples (Figure 11a), samples with Mg/Fe 1:3 and 5:2 display a sharp peak with a maximum at 3.5 and 4 nm, respectively. Sample with Mg/Fe ratio 2:1 has a different pore distribution, over a large range, with maxima at 4 nm and 16.8 nm. At 550ºC (Figure 11b), the sample with Mg/Fe ratio 2:1 shows a more narrow pore size distribution around 3.7nm, while the one with Mg/Fe 5:2 displays a two high intensity peaks for a bimodal pore distribution centered around 3.7 nm and 9.5 nm. The PSD curve for the sample with Mg/Fe 1:3 at 550ºC is broad and shifted towards a larger size pores, with a maximum centered at 20.4 nm. At 900ºC (Figure 11c), only samples with Mg/Fe ratios of 2:1 and 5:2 display PSD curves, the one Fe(III)-rich sample is almost non-porous, as suggested by the very low BET surface area (Table III). The PSD for the Mg/Fe 2:1 sample is bimodal, with two maxima at 2.7 nm and 12.2 nm, while the PSD for the Mg/Fe 5:2 is centered around a single maximum at 14 nm. Consequently, at all temperatures, samples are mesoporous, no pores larger than 21 nm were found in samples at all temperatures.

TEM micrographs of the pyroaurite sample with Mg/Fe 1:3 illustrate that this sample has an amorphous nature (Figure 12a), while sheet-like particles are observed for the other two samples with higher Mg(II) content (Figure 12b,c). At 550ºC, particles for the sample Mg/Fe ratio 1:3 become more defined in shape (Figure 13 a). The sheet-like structure for samples with Mg/Fe 2:1 and 5:2 is preserved at this temperature (Figure 13 b,c), even though the pyroaurite has decomposed in the corresponding oxides. This preservation of shape is most likely due to the topotactic decomposition mechanism[9] of pyroaurite. At 900ºC, rhombohedral particles are predominant for all samples, owing to rhombohedral shape of either hematite or spinel structures (Figure 14).

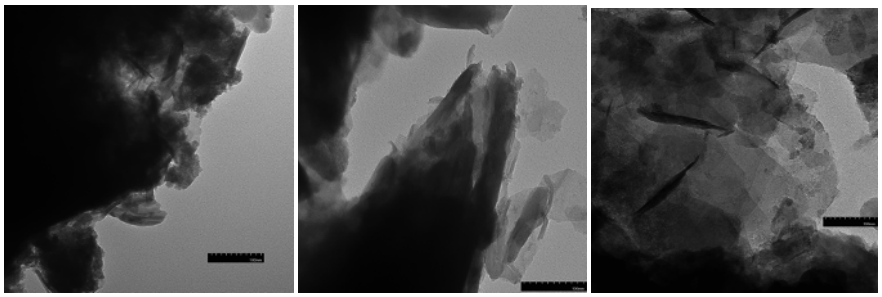

(a) (b) (c)

Figure 12. TEM micrographs for pyroaurite samples: a. Mg/Fe=1:3, b. Mg/Fe= 2:1, c. Mg/Fe 5:2.

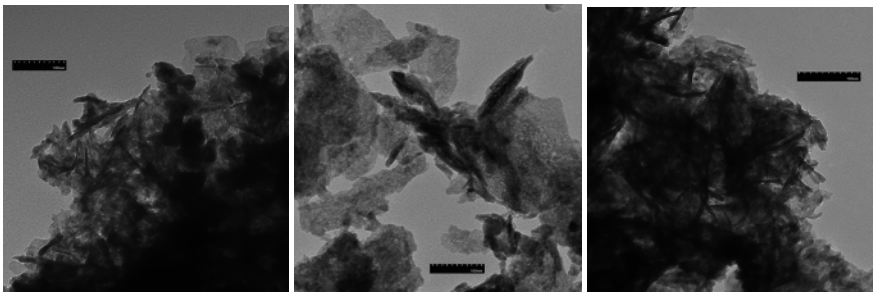

(a) (b) (c)

Figure 13. TEM micrographs for oxides at 550ºC: a. Mg/Fe=1:3, b. Mg/Fe= 2:1, c. Mg/Fe 5:2.

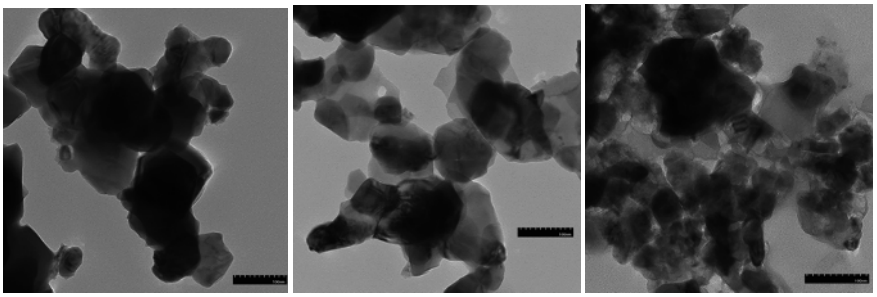

(a) (b) (c)

Figure 14. TEM micrographs for oxides at 900ºC: a. Mg/Fe=1:3, b. Mg/Fe= 2:1, c. Mg/Fe 5:2.

CONCLUSIONS

Pyroaurite-like structures with various Mg/Fe molar ratios have been obtained by coprecipitation. Structural, morphological and surface properties were found to be very dependent of the cation ratios. The Fe(III)-rich sample was mainly consisting of an amorphous Fe(III)-phase that led to oxides with very low surface area, while the samples with higher Mg(II) content consisted of crystalline pyroaurite lead to oxides with high surface area. High Fe(III) content is not desirable, in spite of an initial high surface area and small crystallite size. These desired characteristics are not preserved after calcinations. The special structure and decomposition mechanism of samples with Mg/Fe ratios 2:1 and 5:2 led to oxides with high surface area at 550ºC, along with a smaller crystallite size compared to the starting material. These make those compositions good candidates for catalytic reactions and/or adsorption of acidic species.

Acknowledgements

We acknowledge the financial support of the William Paterson University through Center for Research summer grant 2015 and ART grant 2014-2016.

REFERENCES

[1]P.G.Rouxhit and H.F.W. Taylor, Thermal decomposition of Sjögrenite and Pyroaurite, *Chimia*, **23**, 480-85 (1969).

[2]H.F.W. Taylor, Crystal structures of some double hydroxide minerals, *Mineralogical Magazine*, **39(304)**, 377-89 (1973).

[3]O.P. Ferreira, O. L. Alves, D. X. Gouveia, A. G. Souza Filho, J.A.C. de Paiva, and J.Mendes Filho, *J. Solid State Chem.* **177**, 3058-69 (2004).

[4]H.C.B. Hansen and C. Bender Koch, Synthesis and characterization of pyroaurite, *Applied Clay Sci.*, **10**, 5-19 (1995).

[5]Novel process for removing sulfur from fuels, US Patent, US 2010/0025301 A1, WO 2005/116169 A1.

[6]S. Dhir, R. Uppaluri and M.K. Purkait, Oxidative desulfurization: Kinetic modelling, *Journal of Hazardous Materials*, **161,** 1360-68 (2009).

[7]D. E. Sparks, T. Morgan, P.M. Patterson, S. A. Tackett, E. Morris, and M. Crocker, New sulfur adsorbents derived from layered double hydroxides I: Synthesis and COS adsorption, *Applied Catal. B: Env* **82**, 190-98 (2008).

[8]F. Cavani, F. Trifiro, and A. Vaccari, Hydrotalcite-type anionic clays: preparation, properties and applications, *Catal. Today* **11**, 173-301 (1991).

[9]M. Bellotto, B. Rebours, O. Clause, J. Lynch, D. Bazin, and E. Elkaim, Hydrotalcite Decomposition Mechanism: A Clue to the Structure and Reactivity of Spinel-like Mixed Oxides, *J. Phys. Chem.* **100**, 8535-42 (1996).

[10]Y. Ohishi, T. Kawabata, T. Shishido, K. Takaki, Q. Zhang, Y. Wang, K. Nomura, and K. Takehira, Mg-Fe-Al mixed oxides with mesoporous properties prepared from hydrotalcite as precursors: Catalytic behavior in ethylbenzene dehydrogenation, *Appl. Catal. A: Gen* **288**, 220-31 (2005).

[11]V. Rives, Mater. Characterisation of layered double hydroxides and their decomposition products, *Mater. Chem. Phys.* **75**, 19-25 (2002).

[12]M.J.H. Hernandez-Moreno, M.A. Ulibarri, J.L. Rendon, and C.J. Serna, IR Characteristics of Hydrotalcite-like compounds, *Phys. Chem. Min.* **12**, 34-38 (1985).

[13]C.J. Serna, J.L. Rendon, J.E. Iglesias, Crystal chemical study of layered $[Al_2Li(OH)_6]^+H^-\bullet nH_2O$, *Clays Clay Min* **30**, 180-82 (1982).

[14]D.G. Evans, and R.C.T. Slade, Structural Aspects of Layered Double Hydroxides, *Struct. Bond.* **119**, 1-87 (2006).

[15]D.L. Bish, Deviations from the ideal disordered structure in minerals of the pyroaurite group, *Program and Abstracts, 6th International Clay Conference*: Oxford (1978).

[16]A.F. Wells, Structural Inorganic Chemistry, Fifth Edition, Clarendon Press, Oxford (1984).

[17]J. Preudhomme and P. Tarte, Infrared studies of spinels-III. The normal II-III spinels, Spectrochimica Acta, 27A, 1817-35 (1971).

[18]J. Preudhomme and P. Tarte, Infrared studies of spinels-I. A critical discussion of the actual interpretations, Spectrochimica Acta, 27A, 961-68 (1971)

[19]F. Kovanda, V. Balek, V. Dornicak, P. Martinec, M. Maslan, L. Bilkova, D. Kolousek, and I.M. Bountsewa, Thermal behaviour of synthetic pyroaurite-like anionic clay, Journal of Thermal Analysis and Calorimetry, 71, 727-37 (2003).

[20]G. Carja, R. Nakamura, T. Aida, and J. Niiyama, Textural properties of layered double hydroxides: effect of magnesium substitution by copper or iron, *Microporous and Mesoporous Materials*, **47**, 275-84 (2001).

FORMATION AND CHARACTERIZATION OF NANO-SCALE TITANIUM CARBIDES IN A TITANIUM TRIALUMINIDE INTERMETALLIC

Edward A. Laitila
Donald E. Mikkola
Michigan Technological University
Houghton, Michigan, USA

ABSTRACT

Nano-scale cubic titanium carbide particles can be produced within the powder particles of a chromium-modified titanium trialuminide intermetallic by mechanonanosynthesis; that is, milling the intermetallic powder in the presence of an organic process control agent. The amount of the carbide in the microstructure can be very large, actually exceeding the amount of intermetallic, and is controlled simply by the milling time and addition of titanium powder. The small carbide particles produced in the heavily cold worked intermetallic powder are of the order of 2 nm, which is also the scale of the dislocation substructure, posing a challenge to the characterization of the milled material. Despite the severe peak broadening and overlap in the x-ray diffraction patterns it has been possible through profile fitting and synthesis to define and model the microstructure, as well as to follow the changes caused by consolidation giving insight not only into the microstructure formation, but the unusually high strengths of the consolidated composite material.

INTRODUCTION

Contrary to the binary titanium trialuminide which is very brittle, the chromium-modified titanium trialuminide intermetallic $(Al,Cr)_3Ti$ which forms the cubic $L1_2$ structure[1] has shown some compressive ductility along with excellent oxidation resistance and good high-temperature properties.[2] Given the moderate but good density-compensated strength, the original goal of this research was to strengthen this cubic $L1_2$ chromium-modified titanium trialuminide intermetallic by incorporating dispersoids of TiB_2 reduced in size by the "mechanical alloying" process. This process first developed by Benjamin[3] is often used to describe any severe mechanical deformation action by a milling process. More specific definitions have been applied such as mechanical alloying relating to the occurrence of solid-state alloying, whereas mechanical milling refers only to a size reduction.[4] In the current work attempts at mechanical alloying/milling combinations of elemental and/or prealloyed intermetallic powders with TiB_2 powders in a dry environment were unsuccessful and suggested the use of a process control agent (PCA) to facilitate milling. Historically there have been concerns about contamination by any added liquid with these types of milling processes.[5] Investigation of this issue of PCA contamination during mechanical alloying/milling of the trialuminide powder in an initial long time milling process monitored with x-ray powder diffraction (XRD) gave the unexpected results shown in Figure 1. That is, the domination of the XRD pattern by a new titanium carbo-nitride phase comprised of the isomorphous phases TiC and TiN identified by the * and + symbols and representative stick patterns respectively superimposed on the XRD pattern. Originally it was thought the TiB_2 phase shown would be the dispersoid. However, with the formation of the Ti(C,N) phase with a crystallite size an order of magnitude smaller and with this phase also being a hard particle the original approach was abandoned for the more favorable reaction product. This result changed the direction of the research to focus on the *in situ* reactions particularly those between the titanium in the intermetallic powder and the carbon from the PCA. As will be shown, this technique produces a hard, very fine, dispersoid of the carbide phase, the

amount of which can be easily controlled by simple processing parameters such as processing time.

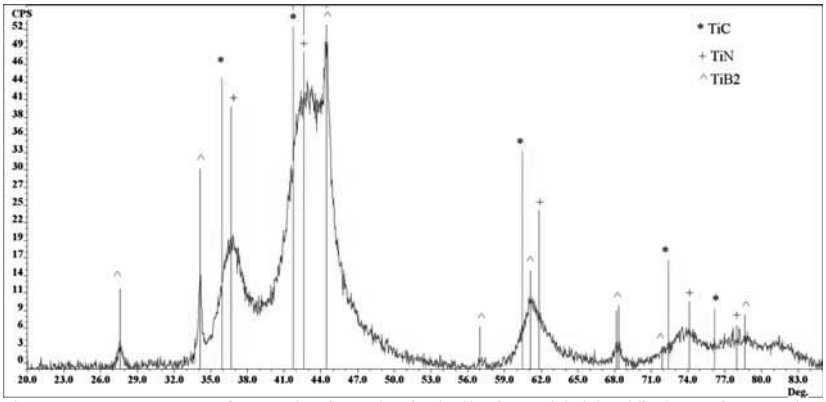

Figure 1 XRD Pattern after 90 h of mechanical alloying with identified reaction product phase Ti(C,N) with TiC identified by the * symbol and TiN identified by the + symbol with the representative stick patterns for each with the admixed TiB_2 identified by the ^ symbol.

Traditionally, the term *nanometer* region relates to features with sizes from 1 to 100 nm; however, in the current work sizes in the single-digit nanometer range are of interest and will be distinguished from the larger sizes with the term *nano-scale*. Unfortunately, when particle sizes, dislocation substructures, and grain sizes of metal matrix composite materials are in the nano-scale region characterization of the material by electron beam microscopy or x-ray diffraction (XRD) analysis becomes difficult. With electron beam imaging, scanning microscopy resolution has size limits near that of the lower nanometer regime, and with transmission microscopy the nano-scale features are often much smaller than the thickness of thin sections. In addition, the free surfaces created by thinning can change the energetics dramatically and hence the equilibria of the system. X-ray diffraction studies provide atomic-scale resolution in a natural three-dimensional environment, but the multiphase scattering effects complicate the patterns and while the structures can be determined, separating these effects has been difficult. Specifically, multiphase nano-scale crystallite sizes produce diffraction patterns comprised of many superimposed extremely broad overlapping diffraction peaks resulting in “amorphous-like” diffraction patterns thus masking important features of the diffraction, especially for phases with similar lattice parameters. Despite these difficulties, some simple procedures will be detailed here that lead to a much improved understanding of such patterns.

EXPERIMENTAL PROCEDURES

The current experiments will show that the systematic uptake of elements from the PCA can produce beneficial hard particle reaction products which ultimately yield composite materials with nano-scale features. The original goal to mechanically alloy the $L1_2$ intermetallic $Al_{66}Cr_9Ti_{25}$ chromium-modified titanium trialuminide with a hard particle dispersoid was therefore accomplished with TiC as a reaction product. This process is a variation of the mechanical alloying process with adequate amounts of the PCA (hexanes C_6H_{14}) providing the

carbon. This new process which can control the amount of the nano-scale hard particle reaction products that develop *in situ* is given the name Mechanonanosynthesis (MNS).

All MNS processing here was accomplished with a SPEX™ mill using a 6 to 1 charge ratio, about 90 g of mill media, 15 g of powder, and 18 mL of hexanes, in an argon environment. The post-processed powders are referred to as "as-milled" powder. In the first experiment a detailed characterization was carried out on powders having undergone the same MNS processing conditions of 13.65 g of prealloyed powders ($Al_{66}Cr_9Ti_{25}$) with 1.35 g of pure titanium sponge, an amount that was determined based on the amount of titanium to completely react with carbon to form TiC, while the 20 h processing time and amount of titanium in the experiments were based on an estimated carbon content of 2 wt. % when titanium trialuminide elemental powders were mechanically alloyed for 20 h.[6] Two prealloyed powders were used: a Reading Alloying (RA), which contained a small amount of carbon (0.25 wt. %), and a Master Alloy (MA). The variable in this case was the MNS processing time systematically varied for times of 0.5, 1, 5, 10, 15, 20, 25, 30, and 40 h. In the second experiment, powders with larger amounts of carbide were formed based on the same 13.65 g of $L1_2$ intermetallic alloy with 1.35 g of elemental titanium processed for a target period of 20 h[6] as just described. However, in this case the amount of titanium and MNS processing time were systematically increased by factors of 1, 2, 3, 5, and 6 (with corresponding decreases in $L1_2$ intermetallic) with these powders used for consolidation into bulk samples.

Half of the powders produced were degassed by vacuum annealing at 500ºC to remove hydrogen with these powders then encapsulated in quartz ampoule in an argon environment. These encapsulated powders were annealed at 1000ºC for 2 h to produce powders to be used as annealed reference powders.

The powders processed by MNS were examined by XRD with a Scintag (Division of Thermo ARL, Dearborn, MI) XDS-2000 instrument outfitted with 1 and 2 mm beam slits with 0.5 and 0.3 mm receiving slits at a 45 kV and 35 mA power setting for the copper target tube using dwell times of 20 sec, or more, with step sizes of 0.03 to 0.05º and a 2θ range from 10 to 120º. Surface topography of the as-milled (post MNS processing) powders was imaged with a Hitachi (Pleasanton, CA) S-4700 field emission scanning electron microscope. Carbon analysis was accomplished with a LECO (St. Joseph, MI) model C/S 224 inert gas fusion-chromatograph.

RESULTS

Carbon analysis of alloys created from the second experiment in which case the elemental titanium content in the mixture and the MNS time were multiplied by factors of 1, 2, 3, 5, and 6 resulting in a near linear uptake of carbon as a function of processing time as shown in Figure 2. The base composition for this series of alloys was 13.65 g of prealloyed trialuminide and 1.35 g of titanium for a 20 h MNS time with two alloys created at 20 h; denoted RA containing a small initial amount of carbon from the synthesis process, with the MA having no initial carbon present.

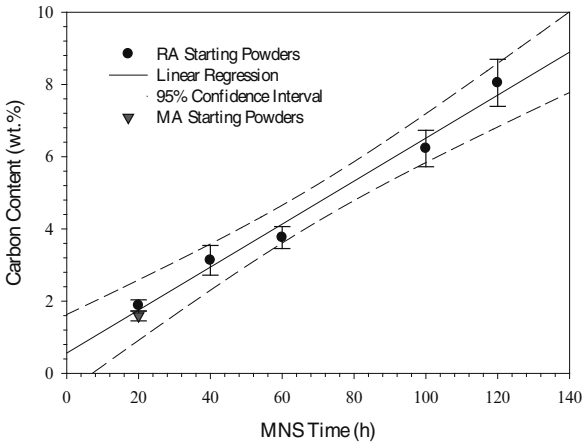

Figure 2 Dependence of carbon uptake on MNS processing time with elemental titanium amounts increased by the same factor for each test increment.

Characterization of the as-milled powders with XRD was accomplished by a combination of "intelligent" profile-fitting and synthesis of the individual Pearson VII peak profile models for each phase using the DMSNT (Scintag, Inc.) peak profile fitting software. The intelligent profile fitting simply requires detailed knowledge of the phases present and based on this information subsequent placement of peaks of proper intensity, approximate width, and in the proper position, provided the best simulation of the experimental information. Difficulties can arise in this process by not providing adequate initial models for the "first-guess" of the summation of each model; so that the required peaks may not be present or may be in the wrong positions with incorrect shapes, but may mathematically satisfy the convergence despite a lack of a physical description. The initial long-term milling experiment made possible the identification of the new phases formed providing the needed information for proper location to place each of the diffraction peaks from all phases identified. Several iterations (including background removal) were then carried out to help validate the process and provide statistical information with all data reported as an average of all individual profile peak analyses for each diffraction peak in these complex patterns. Examples of the XRD patterns for MNS times of 5 to 40 h are shown in Figure 3. All patterns, including the "amorphous-like" nature of the 40 h pattern with the very broad maximum peak, could be broken down by proper angular placement of the individual diffraction peaks for each phase identified with convergence providing detailed peak parameters.

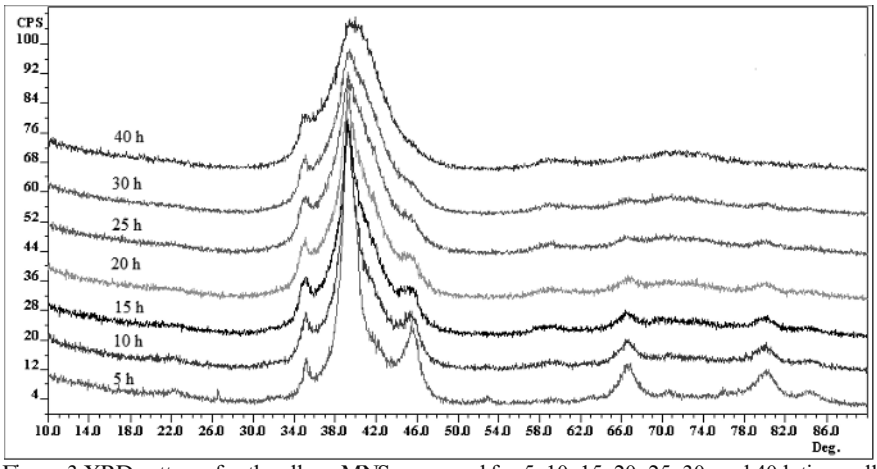

Figure 3 XRD patterns for the alloys MNS processed for 5, 10, 15, 20, 25, 30, and 40 h times all with similar starting chemistries.

An example of a deconvoluted diffraction pattern using this method is shown in Figure 4 with all identified phases accounted for, the $L1_2$ intermetallic, TiC, and TiH_2 (the hydrogen is removed later by vacuum annealing at 500ºC). Once the individual diffraction peaks are profile fit to the model, by minimization of the error between the sums of individual profiles with the raw data, individual peak parameters can be used for subsequent XRD analysis. Lattice parameter values determined for each phase helped in validation of the analysis.

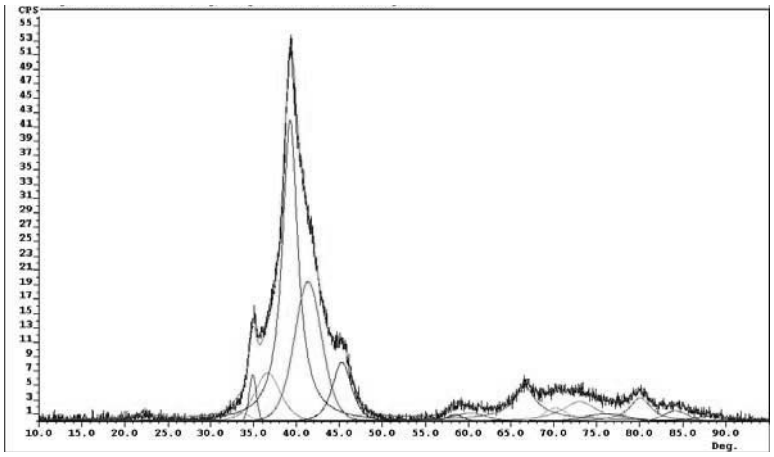

Figure 4 Profile fit example for phases identified in the XRD pattern for the 20 h MNS processing time.

Comparison of the XRD pattern of the as-milled material with that of annealed powder both with the same intensity scale, Figure 5, illustrates the easily observable increase in the background scattering over the whole 2Θ range. It should be noted the powder packing densities were essentially identical for each sample. The increased background scattering has been attributed to the random static displacements of atoms at the grain boundaries and this boundary phase will be given the designation of nano-grain boundary (NGB). This measurable scattering, increasing regularly with MNS processing time, makes it possible to estimate the volume fractions of the NGB phase from the intensity difference between the annealed and as-milled patterns.[7] Using this method in combination with the direct comparison method the total volume fractions of both crystalline and non-crystalline regions can be determined.

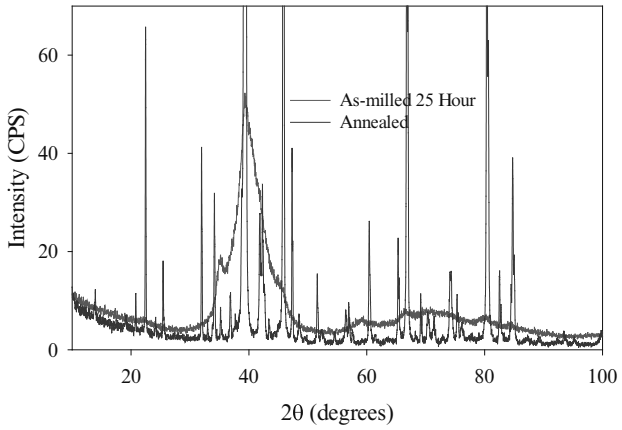

Figure 5 Comparison of as-milled powder to annealed powder with the same intensity scale.

Applying this overall approach to the experiment in which MNS processing time was increased with the same initial powder chemistry gives the results shown graphically in Figure 6. The NGB component increases rapidly as the crystallite size decreases with little change after MNS processing times of 10 - 15 h. As expected a rapid increase in TiC is observed with MNS time that appears to increase at a lesser rate as time progresses. However, there is no elemental titanium (diamond-shaped data points in Figure 6) present after the 15 h MNS time despite the still increasing TiC content. The $L1_2$ intermetallic decreases in a smooth systematic fashion as expected; prior to the correction for the background scattering the $L1_2$ intermetallic phase unrealistically increased initially then decreased. Another reaction product is the TiH_2 phase which increases at a much lower rate than the TiC. As noted, the hydrogen was easily removed as a post-MNS processing step prior to consolidation.

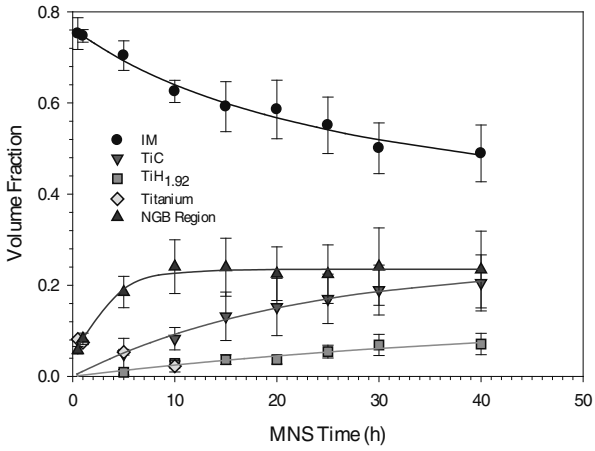

Figure 6 Phase volume fractions for the various MNS processing times all with the same starting composition.

The determined individual peak profiles represented with the common XRD Pearson VII peak model can be synthesized and then used as input to a Warren-Averbach analysis to determine crystallite size and microstrains. Each determination reported is the mean of at least three individual profile fit iterations. The Warren-Averbach method requires an annealed pattern for the Stokes correction of instrumental effects in the typical manner, this was accomplished with a well-annealed -400 mesh powder pressed and structurally detailed.[8] This process of developing the Warren-Averbach crystallite size and microstrain data for the series of alloys resulting from MNS processing of the same composition powders has been described earlier in the Powder Diffraction Journal.[7] Results of this analysis are illustrated in Figure 7 showing similar responses for both the <111> and <200> directions. The microstrain approaches a large value of 1 % elastic strain; however, it is a realistic strain considering the consolidated materials have been shown to be able to support these elastic strains. Conversely the crystallite size shows a rapid decrease asymptotically to a value of about 2 nm a size similar to that suggested as a theoretical size limit of a crystalline material.[9] The error bars are 95 % confidence intervals developed based on multiple background fit/profile fit synthesis followed by Warren-Averbach analysis. Note three of the data points show no error bars as these all converged with very similar models in multiple profile fit attempts.

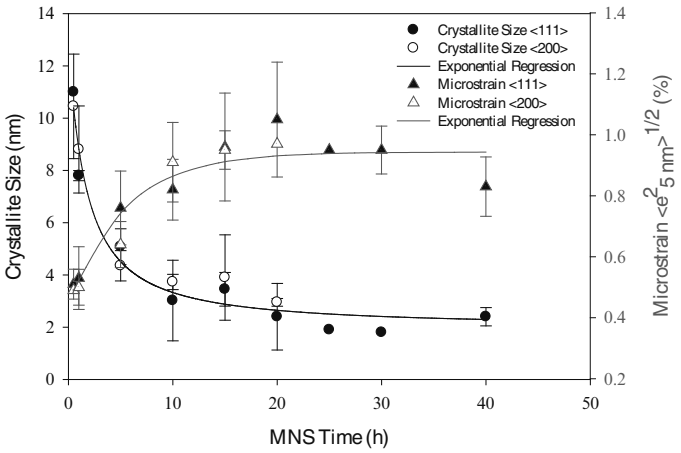

Figure 7 Warren-Averbach results of synthesized diffraction peaks for <111> and <200> directions in the $L1_2$ intermetallic phase.

Traditionally, dislocation densities have been estimated from the crystallite size, D, microstrain, $\langle \varepsilon^2 \rangle^{1/2}$, and Burgers vector according to $\rho = 2\sqrt{3}\langle \varepsilon \rangle^{1/2} / bD$. While the Burgers vector could not be determined a common room temperature dislocation observed in this material is the a/3<112> partial. Milligan[10] suggested that in general there is a different deformation mechanism for each of four regions of grains sizes; grain sizes above 1 μm traditional deformation by full dislocations nucleated within the grains; 30 nm to 1 μm where plastic deformation occurs by dislocations nucleated from grain boundary sources; 20 to 30 nm deformation dominated by partial dislocations that only pass through the grains; and those below about 10 nm where deformation occurs by grain boundary-mediated processes. It can be noted that the extremely small size crystallites observed here suggests this latter case will apply. The estimated dislocation densities determined for these MNS processed samples range from $4.6X10^9$ mm^{-2} at 0.5 h to constant values of about $5.4X10^{10}$ mm^{-2} for 20 h or beyond. These latter values are extremely large, about an order of magnitude larger than dislocation densities of ~ $5 X 10^9$ mm^{-2} in heavily cold rolled metals.[11]

The second experiment produced powders for consolidation that were processed by MNS with the base elemental titanium amount of 1.35 g with a 20 h processing time, both parameters were incremented by 1, 2, 3, 4, and 6 times (with a corresponding decrease in the amount of $L1_2$ intermetallic). As shown in Figure 8 the XRD peaks for the TiC phase at MNS processing time of 120 h dominated the XRD pattern indicating that very large amounts of reaction product can be easily produced in the as-milled state.

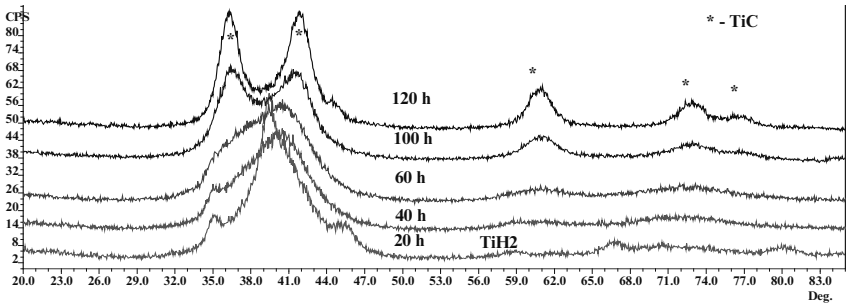

Figure 8 XRD patterns of as-milled powder for longer MNS processing times and similarly larger amounts of elemental titanium.

Microscopic study of the as-milled particle surfaces revealed heavy deformation of the surface that appeared to be made up of highly plastically deformed or "smeared" particles on larger particle surfaces such as the particle shown in Figure 9 highlighted by the black arrow. Assuming an original spherical shape for the smeared particle and considering the small thickness of the smeared particle on the surface, the estimated plastic deformation undergone by the particle is quite large, certainly exceeding typical ductilities observed in the large-grained $L1_2$ intermetallic. This is unusual given the mechanical properties of the $L1_2$ intermetallic. Close examination shows that the entire surface is littered with these smaller particles smeared and bonded to the surface of larger particles. Little attention has been given to this behavior in the literature, despite the likelihood that these surface features reflect fundamental aspects of the "mechanical alloying" process.

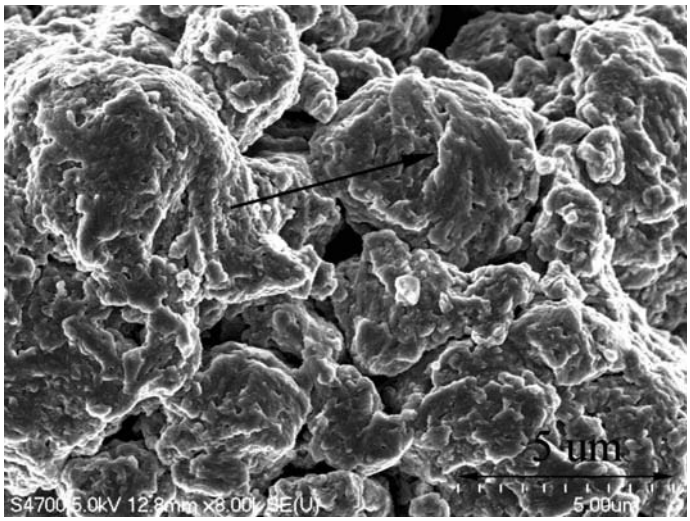

Figure 9 Field emission electron microscope micrograph of powder particle surface from MNS processing for 10 h.

DISCUSSION

MNS processing produces crystallite sizes and reaction products with microstructural features that have the smallest expected size for a polycrystalline material. The small size of the crystallites and measurable increase in the background scattering suggest microstructural features in agreement with observations by Gleiter et al.[12] for a 6 nm grain size sample indicating the background scattering was from atoms comprising the grain boundary region. Recall that the volume fraction of this NGB phase was 0.24 of all the phases (Figure 6). However, it represents 0.48 of the $L1_2$ intermetallic material as these would only include grain boundaries within that phase. In earlier work by Gleiter et al.[13] on a 6 nm grain size iron sample the grain boundary atoms were estimated to be close to 50 % in number and volume, having a value similar to that experimentally determined here, with these atoms on the grain boundaries suggested to have a "gas-like" structural arrangement.

This severe deformation processing causes significant defect generation with extremely large dislocation densities. However, the detailed nature of these defects/dislocations has not been determined. A detailed study of dislocations and defects is an important focus for future work in analyzing as-milled powders by transmission electron microscopy. The small intermetallic crystallites are expected to be defect free; therefore the defects must reside on the surface of these crystallites providing the origin for the observed large microstrains. In large-grained polycrystals the grain boundary surface is atomically thin and often has a superstructure consisting of coincident lattice sites[14] that are typically several to tens of atoms apart. Since these distances can easily exceed the expected size of the individual grain facets on the 2-3 nm grains assuming a tetrakaidecahedral shape, this type of large-grain boundary structure cannot exist. Grain boundary structural changes have also been observed in work by Valiev et al.[15] who suggested a new grain boundary structure emerging in sub-micrometer/nanometer grain sized materials (i.e. sizes closer to the 100 nm upper limit of nanometer range) termed a non-equilibrium grain boundary (NEGB). These consist of large numbers of non-equilibrium extrinsic grain boundary dislocations and show changes in fundamental properties that are typically microstructure-independent, such as Debye temperature and elastic modulus.[16] This can be taken as support for the hypothesis that the grain boundary structure changes in these nano-scale materials are necessary to accommodate the large increase in surface area, concurrent with a decrease in each grain facet surface area becoming a small number of unit cells.

Based on the detailed characterization of the as-milled powder an average microstructural model can be suggested considering only the $L1_2$ intermetallic and the TiC phase. Combining the small crystallite size, extremely high dislocation (or defect) density, with the boundary structure change to an NGB structure leads to the model presented in Figure 10. It is derived from the mean dimensions and volume fractions experimentally determined for a tetrakaidecahedron cut through the largest diameters of space-filling polygons yielding the classic hexagonal shape for the average grains. The grain interior modeled by the crystallite size is represented by regular close-packed atomic spacing (no attempt was made to represent exact orientation differences in grains) with the more loosely defined atoms comprising the defect region surrounding the crystallites and random displacements represented by the regions between grains (these atom placements only visually highlight the atomic density differences). The defects must accumulate on the periphery of the crystallites, which are dislocation-free by definition, with the additional change in the grain boundary structure to that of the NGB structure. The small crystallites would be expected to have a very high surface energy thus increasing the internal energy; however, it might be that this crystalline-defect-NGB atomic structural change lessens the surface energy by changing the structural requirements for compatibility. Therefore, the defects on the surface of these crystallites may well act as a structural accommodation gradient to the random static

displacements of the grain boundary atoms thereby lowering the internal energy of the system; i.e., a natural response to the rapidly developed very large increase in surface area. Thus, the grain size can be taken as the center to center distance of the NGB phase regions. These expected and observed changes in the grain boundary structure, support the work of Gleiter et al.[17], who have also shown orders of magnitude increases in diffusion at the grain boundaries and large diffusivities at very low temperatures. Specifically, they reported that the diffusivity for 8 nm grain size copper at 353 °K was fourteen orders of magnitude greater than bulk self-diffusion and about three orders of magnitude greater than with GB self-diffusion in large-grained polycrystalline copper. This three-dimensional contiguous structural arrangement of the NGB's may well be the key to understanding this behavior.

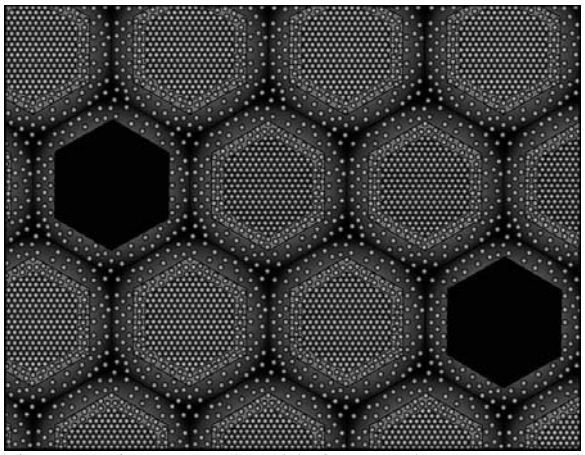

Figure 10 Microstructural model of nano-scale MNS processed as-milled material considering mean sizes of the $L1_2$ intermetallic and TiC phases and data developed in this analysis with the area representing the volume fraction calculated for these regions.

Rigney et al.[18] have shown experimentally the microstructural similarities between the transfer (or tribo) layer from sliding wear of two metals and the deformed materials in the mechanical alloying process developed by Benjamin.[3] In that work it was determined that the tribo layer had grain sizes of less than 10 nm with similar grain sizes also found internally in the mechanically alloyed powder. However, most of the grains in the mechanically alloyed powder were larger and it was concluded that while there are similarities the deformation in the mechanically alloyed material was inhomogeneous compared to the tribo layer. Also it is important to note that the nature of the surface of the mechanically alloyed powder was not investigated. Both these wear surfaces and as-milled powders show alloying, thus mass transport occurs, but plausible detailed explanations of these alloying events are sparse. Considering the structural arrangements developed during MNS processing, along with the Gleiter et al.[17] work on increased diffusivity of nano-scale grain boundaries, it might be expected that this type of NGB structure is developed at the points of contact from the severe deformation in both environments providing a mechanism of enhanced short-circuit diffusion. Importantly, the NGB structure can be considered a contiguous phase creating a three-dimensional highway for rapid diffusivity and hence the immediate and rapid alloying that occurs in both processes. Therefore,

these surface events in "mechanical alloying" processing may play a dominant role in the alloying and grain size reduction as the deformation reaches the limit the material can accommodate under the given conditions. These structures can also play an important role in accomplishing mass transport not only with the alloying but also with the reactions that occur. Further, the triple junctions are possible nucleation sites for the TiC in these contiguous NGB regions. This NGB structure may also play a role in other deformation processes such as cold welding.

Fundamentally important in this study is the discovery of the *in situ* reactions occurring during the MNS processing and their simple dependence on an adequate supply of reactants. For the case of the chromium-modified titanium trialuminide milled with elemental titanium (in the experiment where both the titanium content and MNS processing time were increased) a linear uptake of carbon and production of TiC was observed. When the excess titanium content is fixed the TiC content begins to saturate with all elemental titanium completely reacted by the 15 h MNS processing time. Thus, it is quite clear that titanium is extracted from the base chromium-modified titanium trialuminide alloy but at a much lower rate. Of course, the carbon was always available.

A similar behavior was observed in the MNS processing of iron powder using hexanes as a PCA with *in situ* reaction to produce the Fe_3C phase in amounts dependent on MNS processing time. This suggests that there are a multitude of systems capable of producing a variety of matrix and reaction products in the form of a powder with an extremely high density of non-equilibrium nuclei able to produce unique microstructures utilizing conventional powder metallurgy techniques. The $L1_2$ intermetallic with at least 0.15 volume fraction of carbide has an ultra-high yield strength above 2 GPa, and was produced by conventional powder consolidation with cold isostatic pressing followed by hot isostatic pressing into a fully dense material.[19]

CONCLUSIONS

The MNS process can create composites with engineered volume fractions of particles having nano-scale dimensions by *in situ* reactions. In the system studied here the size of the crystallites in the $L1_2$ intermetallic and size of TiC formed *in situ* during the MNS processing approach the smallest known dimensions for crystalline materials of about 2 nm. At these sizes the grain boundary facet area is of the order of ten unit cells making a coincident type lattice typical of large-grained materials difficult to form. These observations suggest a random static atomic displacement of the atoms in the NGB's and that this disordered structure may well be a response to the lack of lattice sites on these grain boundary facets coupled with the large number of defects on the periphery of the crystallites buffering this structural change and thereby providing thermodynamic stability. These contiguous networks of NGB regions are expected to result in very high diffusivities providing short-circuit diffusion paths for rapid mass transport in low temperature processes such as mechanical alloying.

The origins of the commonly-observed surface smeared particles on the surfaces of larger as-milled particles appear to be point of contact severe deformation of localized material which creates the NGB structure as the material experiences the limits of deformation, in this case reaching a steady state of small size about 2 nm. These structural changes make possible grain boundary mediated plasticity in this near room temperature processing, a process that is similar to superplastic behavior, which although observed at higher temperatures with larger grain sizes, is also dependent on grain boundary diffusion processes. Large deformation related to small crystallites has been reported by Rigney et al.[18] in their wear studies and they suggested a

smallest size of about 3 nm near that developed during MNS processing. Such deformation may be important in other severe deformation point of contact processes such as cold welding.[20]

REFERENCES

[1] S. Zhang, J.P. Nic, and D.E. Mikkola, New Cubic Phases Formed by Alloying Al_3Ti with Manganese and Chromium, *Scripta Met.*, Vol. 24, 57-62, 1990

[2] D.E. Mikkola, J.P. Nic, S. Zhang, and W.W. Milligan, Alloying of Al_3Ti to Form Cubic Phases, *ISIJ International (Japan)*, 31, 10, 1076-1079, Oct. 1991

[3] J.S. Benjamin, Dispersion-Strengthened Superalloys by Mechanical Alloying, *Metallurgical Transactions*, Vol. 1, 2943-2951, October, 1970

[4] C. Suryanarayana, Mechanical Alloying and Milling, *Progress in Materials Science*, Vol. 46, 1-184, 2001

[5] Alan Arias, Chemical Reactions of Metal Powders with Organic and Inorganic Liquids during Ball Milling, *NASA TN D-8015*, NASA, Washington D.C., September 1975

[6] S. Srinivasan, P.B. Desch, and R.B. Schwarz, Metastable Phases in the Al_3X (X = Titanium, Zirconium, Hafnium) Intermetallic System, *Scripta Metallurgica*, Vol. 25, 2513-2516, 1991

[7] E.A. Laitila, D.E. Mikkola, Employing X-ray Scattering to Characterize Materials with Grain Sizes in the Nano-Regime, *Powder Diffraction*, Vol. 23, Issue 2, 96-100, June 2008

[8] J.P. Nic, Structure/Property/Composition Relationships in Cubic Al_3Ti-Base Intermetallic Alloys, *MS Thesis*, Michigan Technological University, 1992

[9] C. Suryanarayana, Nanocrystalline Materials, *International Materials Reviews*, Vol. 40, No. 2, 41-64, 1995

[10] W. W. Milligan, Mechanical Behavior of Bulk Nanocrystalline and Ultrafine-Grain Metals, *Comprehensive Structural Integrity*. Elsevier, Amsterdam 529 (2003)

[11] D. Hull and D.J. Bacon, *Introduction to Dislocations*, Pergamon Press, 1984

[12] R. Birringer, U. Herr, X. Zhu, and H. Gleiter, X-Ray Diffraction Studies of the Structure of Nanometer-Sized Crystalline Materials, *Physical Review B*, Vol. 35, No. 17, 9085-9090, 1987

[13] R. Birringer, H.P. Klein, P. Marquardt, and H. Gleiter, Nanocrystalline Materials an Approach to a Novel Solid Structure with Gas-Like Disorder?, *Physics Letters*, Vol. 102A, No. 8, 365-369, 1984

[14] W. Bollmann, *Crystal Defects and Crystalline Interfaces*, Springer-Verlag Berlin Heidelberg, 1970

[15] R.Z. Valiev, V.Yu. Gertsman, and O.A. Kaibyshev, Grain Boundary Structure and Properties Under External Influences, *Physica Status Solidi*. A, 97, 11-56, 1986

[16] R.K. Islamgaliev, I.V. Alexandrov, and R.Z. Valiev, Bulk Nanostructured Materials from Severe Plastic Deformation, *Progress in Materials Science*, Vol. 45, 103-189, 2000

[17] J. Horvath, R. Birringer, and H. Gleiter, Diffusion in Nanocrystalline Material, *Solid State Communications*, Vol. 62, No. 5, 319-322, 1987

[18] L.H. Chen, M.G.S. Naylor, A.R. Rosenfield, and D.A. Rigney, Wear in Sliding Systems, *Wear*, Vol. 100, 195-219, 1984

[19] E.A. Laitila, and D.E. Mikkola, Ultra-High Strength Composite Materials Developed by Mechanonanosynthesis Processing, *to be published in the MS&T 2015 Proceedings*

[20] N. Bay, Cold Welding. Part 1: Characteristics, Bonding Mechanisms, Bond Strength, *Metal Construction*, Vol. 18, No. 6, 369-372, 1986

GROWTH KINETICS OF LANTHANUM PHOSPHATE CORE/SHELL NANOPARTICLES DOPED WITH Ce-Tb AND Eu

M.C Molina Higgins [1], J. V. Rojas [1]

[1] Mechanical and Nuclear Engineering, Virginia Commonwealth University, 401 West Main Street, Richmond, Virginia 23284-3067301

Keywords: Lanthanide phosphate, nucleation, luminescent nanoparticles

Abstract

Lanthanide phosphate ($LnPO_4$) nanoparticles have been used for biomedical and luminescent devices, in applications ranging from drugs carriers to fluorescent lamps, because of properties such as relatively low toxicity, light absorption and luminescence. This properties are generally affected by size and shape of the nanoparticles. In this work we studied the growth and size evolution of $LnPO_4$ nanoparticles with core and 4 shells-core structure. Lanthanide phosphate nanoparticles were prepared by mixing aqueous solutions of lanthanum chloride ($LaCl_3$), containing a fraction of Cerium-Terbium (Ce-Tb) and Europium (Eu), and Sodium Tripolyphosphate (NaTPP) in a molar ratio of Ln/NaTPP=1. Each solution was aged for 3 hours at~90°C. During the heating process aliquots were collected periodically and analyzed with UV-Vis spectroscopy. Also, XRD, TEM, HRTEM and SAED were used to characterize the crystalline structure and morphology of the nanoparticles. The crystalline structure of the nanoparticles was found to be rhabdophane structure ($LnPO_4 \bullet xH_2O$) and an average particle size of ~4.2 nm for the core and ~5.9 nm for the core-4 shells structure was obtained. Additionally the HRTEM and SAED analysis confirmed the rhabdophane structure observed with XRD.

1. Introduction

The luminescence in phosphors has been an interesting topic for scientist during the last 100 years. The first phosphorus used was synthesized in 1866 by Theodore Sidot and its first use was in television screens [1]. In the recent years, phosphorus at the nanoscale level have been used successfully in applications such as drug carriers [12], fluorescents lamps, display devices, cathode ray tubes, scintillation detection, drug and luminous painting [1]. The luminescent properties of nanophosphors often depend on the shape and size distribution of the nanoparticles. Therefore studies regarding the growth kinetics of this type of nanomaterials, as well as they mechanism of energy transfer has been reported by several authors [2, 3, 4].

The growth of luminescent nanoparticles, and nanoparticles in general, follows the LaMer theory. In this model, the reactive material begins to collide and form clusters, subsequently the clusters become stable and start to grow. These two stages are called nucleation and growth [8]. In order to stabilize the clusters and prevent aggregation, capping agents such as NaTPP [5], oleic acid, [6] cetyltrimethylammonium bromide (CTAB) [7], etc. are added to the synthesis providing a better control of the growth process [8]. The LaMer mechanism is useful to explain the stages of nucleation and growth of several types nanocrystals, however it does not account for the kinetics of the process [9]. In the interest of studying the growth kinetic of the

nanoparticles, ions with luminescent properties are placed inside the material, and the changes in the luminescence are followed in time [5].

$LnPO_4$ materials has been successfully used as phosphors in fluorescent lamps and in scintillation detection [17]. Commercially, inorganic macrocrystals are preferred for the applications aforementioned, however the manufacturing of these crystals is expensive. Consequently fabrication of $LnPO_4$ nanocrystals, offers a low cost alternative for new phosphor technologies. Interesting enough, $LaPO_4$ doped with ions such as Ce-Tb and Eu are a promising materials for biomedical applications such as biolabeling, phototherapy and optical imaging [14, 17]. $LaPO_4$ nanomaterials when doped with Ce-Tb or Eu under UV- excitation at a wavelength of 254 nm become green or red emitters, respectively. In the first case, the energy transfer process occurs between the Ce and the Tb. The Tb acts as an impurity, allowing forbidden transitions in the nanocrystal. When a Ce electron reaches a Tb activation center, a relaxation takes places between the energy bands $^5D_4 \rightarrow ^7F_J$ and a photon is emitted [17]. On the other hand, when a $LaPO_4$ matrix is doped with Eu an electron transfer between the Oxygen (O) 2p shell and the 4f shell of Eu occurs. When the electron return to the valence band, a photon is emitted [14].

In this work, an aqueous colloidal synthesis of Lanthanide phosphate ($LnPO_4$) core-shell structures will be presented. Two types of nanoparticles were made. The first one is $LaPO_4$ doped with Cerium (Ce) and Terbium (Tb), and the second one is $LaPO_4$ doped with Europium (Eu). Furthermore, growth of the nanoparticles with core and core with four shells, was investigated through Ultraviolet-Visible Spectroscopy (UV-Vis). The final product was characterized with X-Ray Diffraction (XRD), transmission electron microscopy (TEM), high resolution transmission electron microscopy (HRTEM), and selected area electron diffraction (SAED).

2. Experimental Procedure

2.1 Materials

Lanthanum chloride ($LaCl_3$) heptahydrate, Cerium Chloride ($CeCl_3$) heptahydrate, Terbium Chloride ($TbCl_3$) hexahydrate, Europium Chloride ($EuCl_3$) hexahydrate and Sodium triphosphate pentabasic ($Na_5P_3O_{10}$ or NaTPP), were obtained from Sigma Aldrich. Additionally, deionized water (DI) (18MΩ) collected from an EMD Millipore Direct QTM 3UV was used for the preparation of the aqueous solutions.

2.2 Aqueous Colloidal Synthesis

Aqueous colloidal synthesis of the core and core-shell $La_{40\%}Ce_{45\%}Tb_{15\%}PO_4$ nanoparticles was carried out with the aforementioned materials. Firstly, a 0.1 M solution of $LnCl_3$ (Ln=La, Ce, Tb) was prepared by mixing $LaCl_3$, $CeCl_3$ and $TbCl_3$ with volume percentages of 40%, 45%, and 15%, respectively. The solution was then added to a 0.1 M NaTPP with a volume ratio of 1:1 and the mixture was vortexed until a colorless liquid was obtained. Subsequently the clear solution was stirred for 3 hours at 90 °C in a 100SH Fisher Scientific Stirring Hotplate. Then, the suspension was allowed to cool at room temperature, transferred to a dialysis membrane and dialyzed against DI water for 24 h. Finally, the clear suspension of core $La_{40\%}Ce_{45\%}Tb_{15\%}PO_4$ was collected. In order to add the first shell, a solution of 0.1M NaTPP: 0.1 $LnCl_3$ (40% $LaCl_3$, 45% $CeCl_3$, 15% $TbCl_3$) with 2:1 v:v ratio was added to the aqueous core solution. For the shell

deposition, the ratio between the Ln Core and Ln shell was 1:1. Subsequently, the mixture was vortexed and placed in the hotplate. The mixture was kept under stirring and heating for 3 h at ~ 90°C. Also, the core-1 shell samples was dialyzed overnight. The procedure above for the addition of shells was repeated 3 more times until 4 shells were added on top of the core. Dialysis of the nanoparticles was carried out between the additions of each shell in order to remove unreacted species. In addition, $La_{75\%}Eu_{25\%}PO_4$ core-shells nanoparticles were also synthesized, following the same procedure mentioned above.

2.3 Sample Characterization

The time evolution absorbance of the resulting nanoparticles, during its synthesis process, as well as their particle size, particle size distribution and crystallinity were evaluated. The evolution of the UV-Vis absorbance of the NaTPP-$LnCl_3$ mixture with time throughout the synthesis process of the nanoparticles analyzed through a GENESYS 10S UV-Vis spectrophotometer. An aliquot from the solution during the heating process was taken every 0.5 hours. Afterwards, the aliquots were diluted in deionized water. Furthermore, the particle size and particle size distribution of the core and core- 4 shells were evaluated by TEM using a Zeiss Libra 120 Plus operating at a voltage of 120kV. For TEM, HRTEM and SAED analysis, the samples were collected after the dialysis a small portion was diluted 100 times in acetone. Next, the samples were sonicated for ~20 minutes to break up any existing aggregates. Finally, a formvar carbon coated copper grid was immersed in the diluted solution and allowed to dry at room temperature. The particle size analysis was performed with the software Image J. the crystalline structure of the nanoparticles was evaluated with XRD. The analysis was carried out using a PANalytical X'Pert Pro diffractometer with a Copper anode (CuK) at a voltage of 45kV and a current of 40 mA. The samples for XRD were prepared by drying the aqueous suspension under vacuum at ~ 35°C. Afterwards the sample was ground to a fine powder. Finally, the fine powder was deposited on the spinning sample stage of the diffractometer. Evaluation of the XRD patterns was performed with the software X'Pert Highscore Plus.

3. Results and Discussion

The aqueous synthesis of $LnPO_4$ nanoparticles is based on the reaction between solutions containing rare earth ions and polyphosphate salts [5]. The heating process implemented in the synthesis of the nanomaterial, activates the hydrolysis of the tripolyphosphate (TPP) group [12]. The hydrolysis promotes a first order reaction in the polyphosphate chain. As a result, the chain splits progressively until the TPP transforms into orthophosphate groups (PO_4^{-3}) [11]. The anion of the PO_4^{-3} reacts with the rare-earth salts cations producing stabilization and size control during the nucleation and crystallization of the $LnPO_4$. As the heating time increases the initial colorless solution becomes turbid due to the coalescence and precipitation of the nanoparticles [12]. The removal of unreacted species through dialysis leads to a translucent suspension. Nonetheless, the addition of shells on the core nanoparticles results in white suspension.

The UV-Vis time evolution spectra for the core structure for both, $La_{40\%}Ce_{45\%}Tb_{15\%}PO_4$ and $La_{75\%}Eu_{25\%}PO_4$ nanoparticles, are presented in figures 1a) and 1 b) respectively. The absorption spectra of $LnPO_4$ nanostructures doped with Ce and Tb, shown in Figure 1.a), evidence two characteristic peaks at 248 nm and the second one at 302 nm at a time equals 0 h, before the starting of the heating process. These features are related to Ce-TPP polymeric bond complexes [10]. The disappearance of the peak at 305nm as the synthesis time increase is due the TPP

transforming into PO_4^{-3} (orthophosphate) and forming covalent bonds with the Ln species. This leads to the formation of $LnPO_4$ crystalline nanostructures. The absorbance peak at 273 nm is related with the amount of crystalline $LnPO_4$ phase [5].In addition this peak is continuously growing during the synthesis process. The peak at 273 nm is associated with transitions between the 4f-4f5d of the Ce in the hydrated $LaPO_4$ matrix. The energy transfer within the nanophosphor is due to the interactions between Ce and Tb. The energy travels from a Ce^{+3} to Ce^{+3} until a Tb^{+3} is reached, subsequently green light is emitted due to Tb^{3+} relaxation and energy transfer between the $^5D_4$ level and the ^7F_J state. It is important to notice, that the relaxation that takes places in Tb is under investigation [17].

The results regarding the core structure of $LaPO_4$ nanoparticles doped with Eu are observed in figure 1.b. The peak at 230 nm represents the interaction of the O^{-2} ligand with the rare earth metal (Eu^{+3}). In this case the absorption and emission of the matrix and the dopant depend on the Eu concentration [13]. The energy transfer mechanism of the nanostructures doped with Eu is due the electron movement between the filled 2p shell of oxygen (which acts as the valence band) and a partially filled 4f shell of Eu^{3+}. This transition occurs at ~ 230 nm. Afterwards, the electron return to the valence state, a photon is emitted and a red light is produced. The band gap of $LaPO_4$ doped with Eu, diminished until a Eu concentration of 50wt% is added to the matrix. Experimentally no decrease in the bad gap is observed from this concentration value [14]. Equation (1) was used to calculate the energy transitions of the undoped and doped material. Where E is the energy transition (J), h is the Planck constant (6.62×10^{-34} J/s), c is the velocity of a photon (3x108 m/s) and λ is the wavelength for each case.

$$E = \frac{hc}{\lambda} \tag{1}$$

The energy transitions calculation by this method leads to values of 5.96 eV, 5.39 eV and 4.56 eV for the $LaPO_4$, $LaPO_4$ doped with Eu and $LaPO_4$ doped with Ce and Tb respectively. The energy transition corresponding to $LaPO_4$ matches with the value presented in the literature for hexagonal $LaPO_4$. In monazite structures this value has been reported to be ~8 eV. [18]. The separation between the conduction and the valence band in various materials doped with Ce^{+3} ions such as $LaSi_3N_5$ and $Sr_3V_2O_8$ has been reported as 4.6 eV [19, 20]. $LaPO_4$ bulk when doped with Ce and Tb present five different energy transitions, due to the different split levels of the excited state ^2D ($5d^1$). These energies are 4.46 eV, 4.76 eV, 5.2 eV, 5.8 eV and 6.05 eV [21]. However at the nanoscale level, for the Tb^{+3} emission due to f-d transition above 5.6 eV are suppressed [21].Similarly, for materials doped with Eu transition energy values between 5.4 and 5.5 eV has been found in compounds such as Y_2O_3 and $InBO_3$ [22, 23]. Most of the energy transfer in $LaPO_4$ nanoparticles doped with Eu is due to the interaction between Eu and O. Another three additional transitions can be observed at $^7F_{0,1} \rightarrow {}^5D_4$, $^7F_{0,1} \rightarrow {}^5G_3$ and $^7F_0 \rightarrow {}^5L_6$, but these peaks have a low intensity because they are forbidden transitions and they cannot be observed with UV-Vis [14].

Changes in absorbance of the matrix during the addition of shells were analyzed and the results are presented in figures 1.c and 1.d. The figures show the time evolution of the absorbance for the most intense peaks, 273 nm and 230 nm, in the $LnPO_4$ doped with Ce-Tb and Eu respectively. The growth of the nanoparticles is a heterogeneous process were the $LnPO_4$ shells grows on top of the core structure. Consequently, the core acts as a nuclei template [10]. The absorbance in the UV-Vis spectra is related to the absorption cross section of the material.

Therefore, an increase in the absorbance will indicate an increase in the amount of crystalline $LnPO_4$ nanoparticles synthesized since there is more material absorbing light [16].

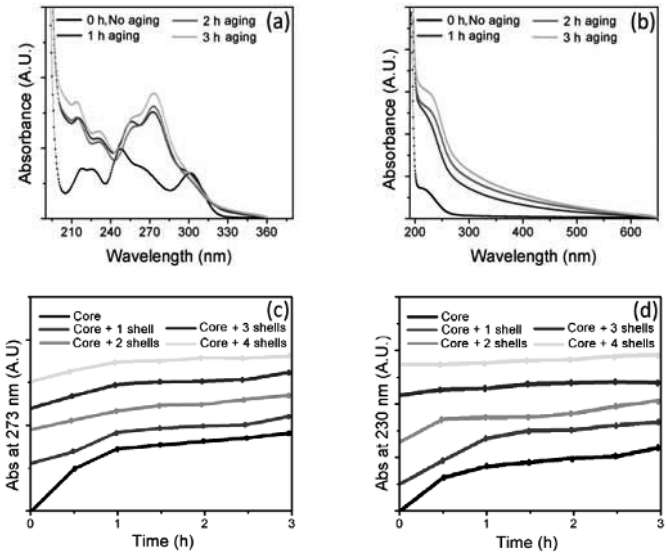

Figure 1. a) And **b)** are the UV-Vis absorption spectra at different time of synthesis from the $La_{40\%}Ce_{45\%}Tb_{15\%}PO_4$ and $La_{75\%}Eu_{25\%}PO_4$ nanoparticles, respectively. **c)** And **d)** Time evolution of the absorption bands at 273 nm and 230 nm for the $La_{40\%}Ce_{45\%}Tb_{15\%}PO_4$ and $La_{75\%}Eu_{25\%}PO_4$ nanoparticles respectively.

The morphology of the nanoparticles was studied by TEM. The TEM images showed an average particle size of 4.3 ± 0.7 nm and 5.9 ± 0.8 nm for the core and core-4 shells of the $La_{40\%}Ce_{45\%}Tb_{15\%}PO_4$ nanoparticles. Analysis of the average particle size in the $La_{75\%}Eu_{25\%}PO_4$ nanophosphor was 4.0 ± 0.6 nm and 5.8 ± 0.8 nm for the core and core-4 shells respectively. In figure 2, TEM micrographs and size distribution of the nanoparticles are shown. Although the results indicates a narrow size distribution, particles of several sizes are observed in the TEM images for core-4 shells. This suggest that part of the precursor NaTPP: Ln do not contribute to the growing of the shells on the nanoparticles but to the formation of new core $LaPO_4$ nanoparticles. Also aggregation of the nanoparticles is observed, as well as a spherical morphology. The dark shade surrounding the nanoparticles is related with the amount of surfactant still present after the 4 dialysis processes.

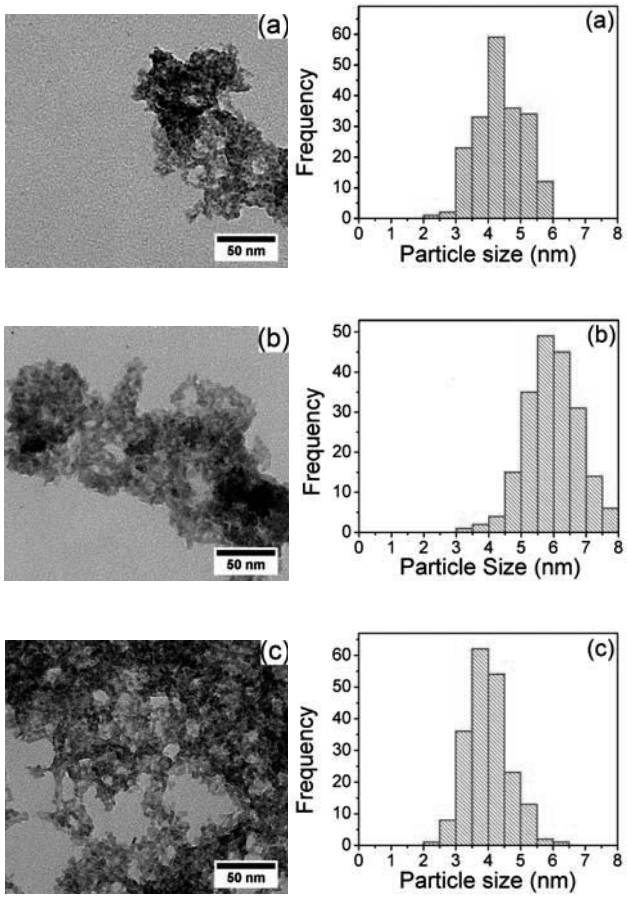
(a)
50 nm
(a)
Frequency
Particle size (nm)
(b)
50 nm
(b)
Frequency
Particle Size (nm)
(c)
50 nm
(c)
Frequency
Particle size (nm)

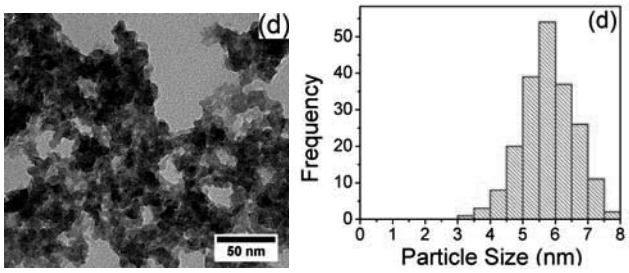

Figure 2. TEM Micrographs and their respective size distribution of **a).** Core $La_{40\%}Ce_{45\%}Tb_{15\%}PO_4$ **b).** Core-4 shells $La_{40\%}Ce_{45\%}Tb_{15\%}PO_4$ **c)**. Core $La_{75\%}Eu_{25\%}PO_4$ d**).** Core-4 shells $La_{75\%}Eu_{25\%}PO_4$.

Evaluation of the crystalline structure of the nanoparticles was carried out through XRD analysis. The XRD patterns shown in figure 3 revealed that the aqueous synthesis of $LnPO_4$ nanoparticles produce a rhabdophane structure (PDF 000-46-1439, $LnPO_4 \bullet xH2O$), that correspond to a hydrated form of hexagonal $LnPO_4$ [10]. In the $LnPO_4$ patterns there is no indication of additional peaks regarding the $LaPO_4$ spectra. Absence of these peaks confirms the complete solubility of the Tb, Ce and Eu in the $LaPO_4$ matrix. The peaks of $LnPO_4$ are shifted to higher 2θ angles with respect to the $LaPO_4$ nanoparticles. The shifting is expected due the different cell parameters of the attained nanoparticles. The atomic radii of La (~187 pm) is slightly larger than the atomic radii of the dopants Ce, Tb and Eu (181 pm, 180 pm and 185 pm respectively). Consequently, a decrease in the unit cell parameters takes places when a dopant replaces a La atom in the lattice [24]. In addition, the XRD patterns were used to calculate the particle size using the Scherrer equation assuming a spherical nanoparticle shape. The results for the $LnPO_4$ nanoparticles doped with Ce and Tb were 4.4 nm, 5.3 nm, 5.6 nm, 5.9 nm, and 6.2 nm for the core, core-1 shell, core-2 shells, core-3 shells, and core-4 shells respectively. Furthermore, the size of the $LnPO_4$ nanoparticles doped with Eu were 4.3 nm, 5.2 nm, 5.5 nm, 5.9 nm, and 6.2 nm for the core, core-1 shell, core-2 shells, core-3 shells and core-4 shells respectively. The particle size results encountered for the $LaPO_4$ doped with Ce and Tb revealed an average thickness of the shells of 0.23 nm, while the nanoparticles doped with Eu had an average thickness of the shell of 0.24 nm Therefore the thickness of the shell corresponds approximately to one atomic layer. Interestingly enough, the attain value of the thicknesses of the second, third and fourth shells for the nanoparticles doped with Ce-Tb and Eu were approximately 0.15 nm, which is less than the atomic radius of La, Ce and Tb. This is an evidence during the process for the addition of shells, new nuclei are formed. Those nuclei grow with a smaller particle size and at a low nucleation rate [10]. As a result the mean particle size measured by the different characterization techniques shift towards smaller particle size values.

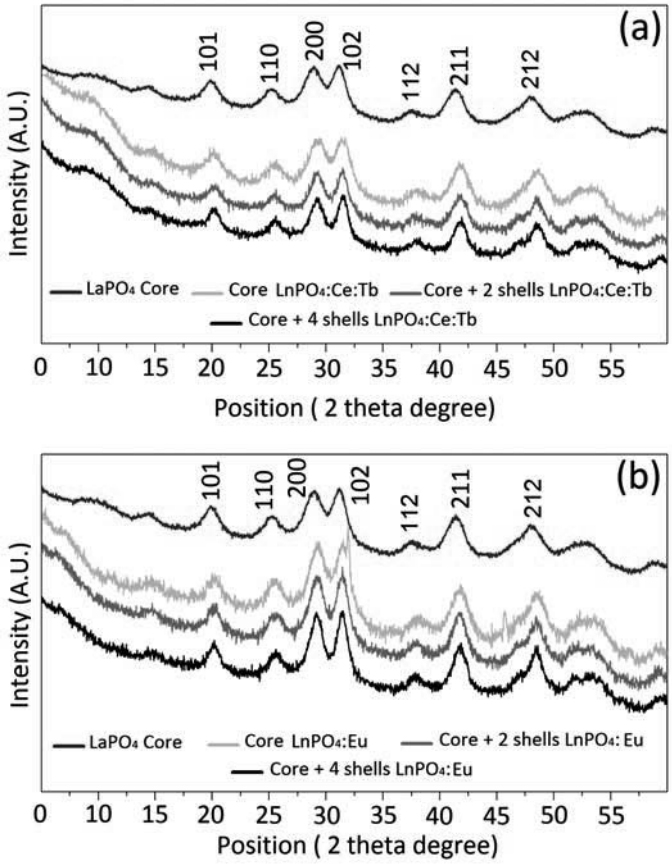

Figure 3. XRD Pattern of **a).** Core shell Structures $La_{40\%}Ce_{45\%}Tb_{15\%}PO_4$ and **b)** Core shell structures $La_{75\%}Eu_{25\%}PO_4$

The crystalline structure of the nanoparticles was also evaluated with HRTEM and SAED and the results are shown in figure 4. The HRTEM image of the core-4 shells nanoparticles doped with Eu revealed a 0.32 nm d_{200} that is in closely agreement to the 0.31nm d_{200} found in the XRD pattern. It is important to notice that, in the HRTEM image, the core is not distinguishable from the shells. Given that the chemical composition of the core and shells is identical, no diffraction contrast was observed. Furthermore, the lattice fringes identified in the core-4 shells images correspond to a single crystalline domain [25]. On the other hand, the d-spacing values found through the SAED pattern for the core-4 shells nanoparticles doped with Ce and Tb match with

the ones obtained with XRD. The XRD d_{200} was 0.31 nm, while the SAED d-pacing in the plane (200) was 0.32 nm.

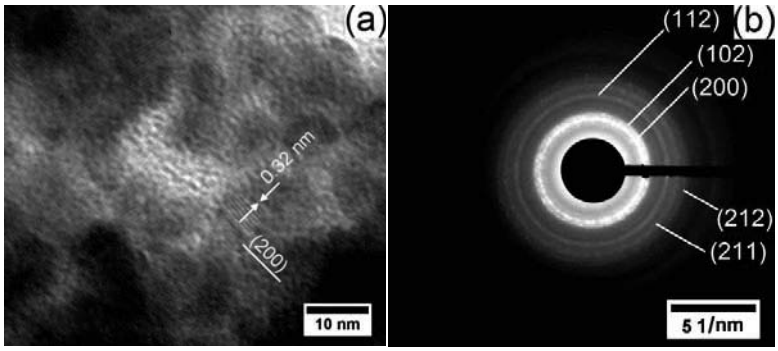

Figure 4. a). HRTEM of Core-4 shell $La_{75\%}Eu_{25\%}PO_4$ nanoparticles and **b)** SAED Core-4 shells $La_{40\%}Ce_{45\%}Tb_{15\%}PO_4$ nanoparticles

4. Conclusions

$LnPO_4$ core shell nanostructures doped with Ce-Tb and Eu, exhibiting green and red luminescence respectively, had been synthesized by an aqueous route. The obtained nanoparticles were evaluated by UV-Vis, TEM, HRTEM, XRD and SAED in order to study the growth, morphology and crystallinity. The time evolution of the absorbance peak at 273 nm for the $La_{40\%}Ce_{45\%}Tb_{15\%}PO_4$ nanoparticles and 230 nm for the $La_{75\%}Eu_{25\%}PO_4$ showed an increasing absorbance. This behavior evidenced the evolution of the amount of $LnPO_4$ in the aqueous suspension with time. In addition nanoparticles with a mean size of 4.3 ± 0.7 nm and, 4.0 ± 0.6 nm were obtained for the core structures while a particle size of 5.9 ± 0.8 nm and 5.8 ± 0.8 nm were found for the core-4 shells nanoparticles. The results were in close agreement with particle size found in XRD by the Scherrer Equation. Further evaluation of the crystalline structure with HRTEM and SAED lead to a d_{200} ~0.32 nm. The nanoparticles exhibited a rhabdophane crystalline structure, a hydrated form of hexagonal $LnPO_4$.These red and green emitters can be used not only in applications such as luminescent devices but also in the medical field, where core shells structures are often needed to encapsulate drugs while their light emission allows to track the drug carriers.

5. Acknowledgements

Research financed with the support of the mechanical and nuclear engineering department from Virginia Commonwealth University (VCU) and the NRC-HQ-84-14-FOA-002 faculty development program in radiation detection and health physics. Also the authors will like to acknowledge to the material's characterization facility NCC (Nanomaterials Core Characterization Center) at VCU.

6. References

[1] Shigeo Shionoya and William M. Yen. *Phosphor Handbook*, (Boca Raton, FL: CRC Press, 1998), 231-233

[2] M. Kawase, T. Suzuki and K. Miura, "Growth mechanism of lanthanum phosphate particles by continuous precipitation," *Chemical Engineering Science*, 62 (2007), 4875–4879.

[3] K. Byrappa, C. Chandrashekar, B. Basavalingu, K. LokanathaRai, S. Ananda and M. Yoshimura, "Growth, morphology and mechanism of rare earth vanadate crystals under mild hydrothermal conditions," *Journal of Crystal Growth*, 306 (1) (2007), 94-101.

[4] X. Xu, L. Hu, N. Gao, S. Liu, S. Wageh, A. A. Al-Ghamdi, A. Alshahrie and X. Fang, "Controlled growth from ZnS nanoparticles to ZnS–CdS nanoparticle hybrids with enhanced photoactivity," *Advanced Functional Materials*, 25 (3) (2014), 445-454

[5] V. Buissette, M. Moreau, T. Gacoin, J.-P. Boilot, J.-Y. Chane-Ching and T. Le Mercier, "Colloidal Synthesis of Luminescent Rhabdophane $LaPO_4:Ln^{3+}$•xH2O (Ln = Ce, Tb, Eu; x ≈ 0.7) Nanocrystals," *Chemistry of materials*, 16 (19) (2004), 3767-3773.

[6] Z. Li, X. Hou, L. Yu, Z. Zhang and P. Zhang, "Preparation of lanthanum trifluoride nanoparticles surface-capped by tributyl phosphate and evaluation of their tribological properties as lubricant additive in liquid paraffin," *Applied Surface Science*, 292 (2014), 971–977.

[7] M. Anbia, M. K. Rofouei and S. W. Husain, "Synthesis of Mesoporous Lanthanum Phosphate and Its Use as a Novel Sorbent," *Chinese journal of chemistry*, 24 (8) (2006), 1026-1030.

[8] K. Carroll, Core-Shell Nanoparticles: Synthesis, Design, and Characterization, (PhD thesis Virginia Commonwealth University, 2010), 2-3

[9] Pekka Hänninen and Harri Härmä, *Lanthanide luminescence: Photophysical, analytical and biological aspects*, (Berlin: Springer Science & Business Media, 2011), 118-119.

[10] V. Buissette, D. Giaume, T. Gacoin and J.-P. Boilot, "Aqueous routes to lanthanide-doped oxide nanophosphors," *Journal of Materials Chemistry*, 16 (6) (2006), 529-539.

[11] Igor S. Kulaev, Vladimir Vagabov and Tatiana Kulakovskaya, *The biochemistry of inorganic polyphosphates* (Chichester: John Wiley & Sons 2005), 11-12.

[12] J. Rojas, J. Woodward, N. Chen, A. Rondinone, C. Castano and S. Mirzadeh, "Synthesis and characterization of lanthanum phosphate nanoparticles as carriers for ^{223}Ra and ^{225}Ra for targeted alpha therapy," *Nuclear Medicine and Biology*, 42, (7) (2015), 614-620.

[13] M. Cayless, Lamps and lighting (New York, NY: Routledge, 2012), 149-151.

[14] S. K. Gupta, P. S. Ghosh, M. Sahu, K. Bhattacharyya, R. Tewari and V. Natarajan, "Intense red emitting monoclinic $LaPO_4:Eu^{3+}$ nanoparticles: host–dopant energy transfer dynamics and photoluminescence properties," *RSC Advances*, 5, (72) (2015), 58832–58842.

[15] N. T. Thanh, N. Maclean and S. Mahiddine, "Mechanisms of Nucleation and Growth of Nanoparticles in Solution," *Chemical Reviews*, 114 (15) (2014) 7610–7630.

[16] M. Califano, "Re-examination of the Size-Dependent Absorption Properties of CdSe Quantum Dots," *The Journal of Physical Chemistry C*, 113 (45) (2009), 19468–19474.

[17] V. Pankratov, A. Popov, S. Chernov, A. Zharkouskaya and C. Feldmann, "Mechanism for energy transfer processes between Ce^{3+} and Tb^{3+} in $LaPO_4$: Ce, Tb nanocrystals by time-resolved luminescence spectroscopy," *Basic Solid State Physics*, 247, (9) (2010), 2252-2257.

[18] S. Syrotyuk, Y. Chornodolskyy, V. Vidtovskyy, A. Voloshinovskii and A. Gektin, "Band Structure of $LaPO_4$," *Functional Materials*, 20, (3) (2013), 373-377.

[19] C. T. Petit, R. Lan, P. I. Cowin and S. Tao, "Structure and conductivity of strontium-doped cerium orthovanadates $Ce_{1-x}Sr_xVO_4$ ($0 \leq x \leq 0.175$)," *Journal of Solid State Chemistry*, 183, (6), (2010), 1231–1238.

[20] A. M. Ibrahim, Z. Lenčéš, P. Šajgalík, L. Benco and M. Marsman, "Electronic structure and energy level schemes of RE^{3+}:$LaSi_3N_5$ and RE^{2+}:$LaSi_3N_{5-x}O_x$ phosphors (RE= Ce, Pr, Nd, Pm, Sm, Eu) from first principles," *Journal of Luminescence*, (164) (2015), 131–137.

[21] V. Pankratov, A. Popov, A. Kotlov and C. Feldmann, "Luminescence of nano and macrosized $LaPO_4$: Ce, Tb excited by synchrotron radiation," *Optical Materials*, (33), (2011), 1102-1105.

[22] M. Ramaiah, "Luminescence studies of europium doped with yttrium oxide nano phosphor," (Atlanta, GA: Scholarly Editions, 2013), 238-240.

[23] Z.-W. Chiu, Y.-J. Hsiao and L.-W. Ji, "Photoluminescence and Optoelectronics Characteristics of Eu-doped $InBO_3$ Nanocrystals," *International Journal of Electrochemical Science*, (10), 2391-2399.

[24] M. Runowski, K. Dabrowska, T. Grzyb, P. Miernikiewicz and S. Lis, "Core/shell-type nanorods of Tb^{3+} doped $LaPO_4$, modified with amine groups, revealing reduced cytotoxicity," *Journal of nanoparticle research*, 15 (11) (2013), 1-16

[25] Zhu, X. Liu, X. Liu, Q. Li, J. Li, S. Zhang, J. Meng and X. Cao, "Facile sonochemical synthesis of $CePO_4$:Tb/$LaPO_4$ core/shell nanorods with highly improved photoluminescent properties," *Journal of Nanotechnology*, 17 (16) (2006), 4217-4222.

INFLUENCE OF SYNTHESIS PARAMETERS ON MORPHOLOGY, CRYSTALLINE STRUCTURE AND COLLOIDAL STABILITY OF CORE AND CORE-SHELL $LaPO_4$ NANOPARTICLES

Miguel Toro [a], Jessika Rojas [a]
[a] Virginia Commonwealth University, Mechanical and Nuclear Engineer Department
Richmond, Virginia, United States

ABSTRACT

Lanthanum phosphate ($LaPO_4$) nanoparticles (NPs) with core and core-shell structure have shown potential as carriers of radionuclides, such as ^{225}Ac and ^{223}Ra, for targeted radiotherapy and imaging. However, their ability to retain both the parent and daughter isotopes may be influenced by the synthesis parameters. In this work, $LaPO_4$ NPs were prepared in aqueous solution using lanthanum nitrate and sodium tripolyphosphate precursors, at moderate temperature and purified by dialysis. Various synthesis procedures modifying the synthesis time, synthesis temperature, and purification procedure were designed and their influence on the size, shape, and stability of the NPs was evaluated through statistical analysis. The crystalline structure, morphology, and colloidal stability of the NPs were characterized with X-Ray diffraction (XRD), transmission electron microscopy (TEM), and zeta potential (ZP). The particle size was found to increase with both the addition of shells and the increment of either the synthesis temperature or time. Nanoparticles as small as 3.4 nm were obtained at 80 °C for 2 h while NPs synthesized at 90 °C for 3 h with the addition of 4 shells of $LaPO_4$ were 6.5 nm in diameter. The synthesis parameters did not show any effect on the crystalline structure nor on the colloidal stability. Similarly, the purification procedures did not have influence on the particle size, furthermore their effect on the colloidal stability was not statistically different.

INTRODUCTION

Materials at the nanoscale level have proven to exhibit remarkable properties not observed at the bulk level. This fact has brought the opportunity to utilize nanomaterials in applications where their specific properties lead to the development of new technologies or the enhancement of current ones. Metallic nanoparticles with various geometries, for instance, have shown numerous properties not obtained in the bulk [1,2]. Thus, they have been investigated and implemented in various areas such as energy, electronics, catalysis, and medicine, among others [3–6]. Nanomaterials have been studied and used in various medical fields such as radioimmunotherapy, target radiotherapy, and diagnostic imaging. For example, super paramagnetic iron-oxide NPs have shown potential as contrast agents for MRI and gold NPs have demonstrated unique size-dependent optical and photothermal properties that make them candidates as contrast agents [7]. Moreover, in the nuclear medicine field, inorganic NPs such as quantum dots, metallic, oxides, and phosphates have generated interest for theranostics as carriers for radioisotopes [8]. Radioactive NPs have been previously synthesized containing the radioactive material on the surface through a linker or as part of the structure as a dopant [9,10].

Lanthanide phosphate NPs have been studied for target alpha therapy (TAT) as carriers for radioisotopes that decay by the emission of multiple alpha particles such as ^{223}Ra, ^{225}Ac, and ^{225}Ra [10–13]. These NPs have shown resistance to radiation damage, size-shape dependent properties. In addition, their surface may be modified with bioconjugates to target specific organs [10,11,14]. Among the different lanthanides phosphates, lanthanum and gadolinium phosphate NPs have been tested

and exhibited promising results retaining the radionuclides during in vitro and in vivo experiments [10–13]. Understanding the effect of the synthesis parameters on the NPs size, crystalline structure, and colloidal stability is crucial for the future application of this type of NPs in medicine. For instance, the size and shape of the NPs may influence the enhance permeability and retention effect (EPR) that is critical for the accumulation of the NPs in the tumor tissue [15]. Moreover, the type of crystalline structure of the NPs might influence the radiation resistance of radioactive NPs used in theranostics [16]. Furthermore, the colloidal stability is critical since NPs tend to aggregate increasing the average size and losing some of their characteristics at the nanoscale level [17].

This study aims to extend the knowledge of the influence of synthesis parameters such as synthesis temperature, synthesis time, and purification procedure on the characteristics of $LaPO_4$ NPs with core and core-shells structures. Lanthanum phosphate NPs were synthesized using an aqueous route at moderate temperature by adapting a procedure developed by Buissette et al [18]. The synthesis temperature, synthesis time, and purification procedure were varied in two different levels to obtain a factorial experiment 2^3. The levels for synthesis temperature and time were defined by tracking the growth kinetics of lanthanide phosphate ($LnPO_4$) NPs with Ultra Violet – Visible spectroscopy (UV-Vis) and the purification procedures were defined based on a preliminary qualitative study in which the stability and sedimentation of NPs was followed during 8 weeks. The influence of these parameters on the NPs was characterized using X-Ray diffraction (XRD), transmission electron microscopy (TEM), and zeta potential (ZP).

EXPERIMENTAL PROCEDURE

Materials

Lanthanum chloride heptahydrate ($LaCl_3$-$7H_2O$), terbium chloride hexahydrate ($TbCl_3$-$6H_2O$, 99.9% purity), cerium chloride heptahydrate ($CeCl_3$-$7H_2O$, 99.9% purity), and sodium tripolyphosphate (Na-TPP) were obtained from Sigma Aldrich. Lanthanum nitrate hexahydrate ($La(NO_3)_3$-$6H_2O$, 99.99% purity, REacton) was from Alfa Aesar. All the chemicals were analytical chemical grade and used without further purification. Deionized water (18 MΩ) was obtained from a MilliPore MilliQ water purification system. A 10 kDa molecular weight cutoff regenerated cellulose dialysis membrane from ®Spectra/Por was used for the purification of the colloidal suspension; the membrane was washed before being used to remove preservatives.

Sample preparation

Core, core + 2 shells, and core + 4 shells $LaPO_4$ NPs were synthesized following a procedure proposed by Buissette et al [18]. For the synthesis of core NPs, 0.1 M $La(NO_3)_3$-$6H_2O$ solution and 0.1 M Na-TPP, in a 1:1 volume ratio, were mixed and vortexed until a clear solution was obtained. Then, the solution was heated at the respective temperature for certain amount of time at continuous stirring. After synthesis, the turbid solution of core NPs was transferred to a dialysis membrane and dialyzed overnight against DI water. The purified solution was split into two equal parts for the later characterization of the core NPs and synthesis of the core-shells NPs.

Two purification procedures to remove unreacted species from both core and core + shells were implemented and evaluated. In the first purification procedure, dialysis was carried out only after the addition of the selected number of shells, i.e. no dialysis purification within the addition of each $LaPO_4$ shell. In this context, dialyzed core suspension was mixed with shells solution

prepared with 0.1 M $La(NO_3)_3$-$6H_2O$ and 0.1 M Na-TPP in a volume ratio of 1:2 and vortexed for ~2 mins. Subsequently, the solution was heated at the selected temperature and time. Once the synthesis time had elapsed for the first shell, a second shell was added. This was done by adding shells solution to the ongoing core + 1 shell reaction at the selected temperature. The process continued for additional few more hours. For characterization purposes a portion of the core + 2 shells NPs was dialyzed overnight, while the rest was used for the synthesis of core + 3 shells NPs. Core + 3 shells and core + 4 shells $LaPO_4$ solutions were prepared following the same proportions and steps described above, i.e. adding shells solution to the ongoing core-shells reaction at the respective temperature and heated for few more hours. Finally, the core + 4 shells solution was dialyzed overnight after the synthesis. For the second purification procedure, similar solutions (chemicals and proportions) and synthesis steps were used for the core-shell structures. The procedure consisted on dialyzing the suspensions for a period of 10 h after the addition of each shell. Therefore, a dialyzed solution was used for the synthesis of each core-shell structure. These additional dialysis steps were implemented to reduce the concentration of unreacted species before the synthesis of each shell. Samples of core, core + 2 shells, and core + 4 shells NPs prepared by the two different purification procedures and combinations of times and temperatures were collected for characterization purposes. The ratio of La content in the core to that of the shells was 1:1.

Design of experiments (DOE)

In order to evaluate the influence of the synthesis parameters, time and temperature, on the characteristics of $LaPO_4$ NPs, two levels of temperature and time were selected. For this purpose a screening experiment was carried out using UV-Vis spectroscopy to determine the lower and upper parameters where crystalline lanthanide phosphate was obtained. $LnPO_4$ core NPs (40% $LaCl_3$-$7H_2O$, 45% $CeCl_3$-$7H_2O$, and 15% $TbCl_3$-$6H_2O$ in volume) were synthesized at temperatures of 75, 80, 85, and 90 °C. The upper limit parameters of 90 °C and 3 h were selected based on the procedure proposed by Buissette et al [19]. The growth kinetics was studied following the evolution of the UV-Vis absorption bands of cerium-trypolyphosphate free complexes and crystalline lanthanide phosphate on the absorption spectrum of the $LnPO_4$ NPs [19]. The spectra were collected for aliquots taken every half an hour throughout the synthesis of the core NPs. Finally, the two purification procedures were implemented and their effect on the NPs colloidal stability was evaluated.

Materials characterization

A PANalytical X'Pert Pro MPD X-ray diffractometer with a copper anode (Cu Kα, λ = 1.5401 Å) was used to investigate the crystalline structure of the NPs. The samples were dried in an oven under vacuum (~30 mm Hg) for 2 days at a constant temperature of 35 °C. Afterwards, the samples were ground until a fine white powder was obtained. The powder was deposited on a zero background plate and the measurements were carried out using the sample stage Reflection-Transmission Spinner PW3064/60 and rotatory speed of 0.5 rev/s. The X-ray tube was operated at a voltage of 45 kV and a current of 40 mA. Crystalline structure and crystallite size analysis were performed on X'Pert HighScore Plus software.

The morphology and particle size were studied by TEM with a Zeiss Libra 120 Plus operating at 120 kV. For TEM imaging, a solution of the purified and filtered NPs was diluted in acetone and sonicated for 20 min. The samples were prepared by immersing a formvar-carbon coated copper grid into the diluted suspension and allowed to dry at room temperature. Particle

size analysis was carried out using the Image J 4.18v software. A Malvern Zen 3600 Zetasizer (Zetasizer nano) was used as a tool to evaluate the colloidal stability of the colloidal suspensions through zeta potential measurements. The samples were filtered with a 0.2 µm pore size filter and measured without further preparation steps.

RESULTS AND DISCUSSION

Synthesis of $LaPO_4$ NPs

The synthesis of $LaPO_4$ NPs in aqueous media is based on a precipitation reaction mechanism. Initially, a homogeneous solution containing La precursor and the complexing agent sodium tripolyphosphate is prepared in order to obtain La-TPP polymeric species. The complexing agent serves two main functions during the synthesis, it restricts the growth of the NPs and forms a stabilizing shell to avoid NPs aggregation. The subsequent thermal decomposition of the solution at moderate temperature promotes the hydrolysis of the tripolyphosphate to form pyrophosphate and orthophosphate ions. The interaction of the orthophosphate (PO_4^{3-}) and La^{3+} ions contribute to the formation of crystallites, while a fraction of the polyphosphate groups help to restrict the growth of the crystallites and provides stability to the NPs in solution [18]. Moreover, an increase in synthesis time results in an increment in the concentration of orthophosphate ions and a change in the solution appearance into a white suspension. Additionally, it promotes the aggregation of NPs since the orthophosphate ions increase at the expense of polyphosphate groups reducing the stabilizing shell around the NPs [18]. The addition of shells to the core NPs was proposed to replicate the core-shell structures studied elsewhere [10,11] and evaluate the effect of the synthesis parameters on these core-shells structures.

Growth kinetics of $LnPO_4$ NPs

The growth kinetics of $LnPO_4$ was carried out to follow the evolution of the UV-Vis absorption bands corresponding to cerium-tripolyphosphate free complexes (248 and 302 nm) and the one associated with the formation of crystalline lanthanide phosphate phase (272 nm). The UV-Vis spectra obtained for the core $LnPO_4$ NPs synthesized at various temperatures of 75, 80, 85, and 90 °C, and times of 1.5, 2, and 3 h are shown in Figure 1 a). The absorption spectrum showed at 0 h correspond to the mixture of the lanthanide salt and the surfactant before the synthesis. For this mixture, the absorption bands of cerium-tripolyphosphate free complexes located at 248 and 302 nm are observed, while the band at 272 nm is not present. Once the solution is heated at temperatures greater than 80 °C the vanishing of the cerium-tripolyphosphate bands and the growth of the band at 272 nm can be observed after 1.5 h of synthesis. For temperatures below 80 °C, the time required for the formation of the crystalline phase is not of interest for the study since the transition from the free complexes to the crystalline phase started after 3 h of synthesis. As it was stated before, variations in synthesis temperatures and times for the DOE might promote the synthesis of NPs with different sizes, i.e. NPs synthesized using the lower and upper parameters might have different sizes. As a consequence, the lower temperature and time selected for the experiment were 80 °C and 2 h respectively. In Figure 1 b) the absorption spectra of 80 and 90 °C for synthesis times of 0, 1, 2, and 3 hours are shown. This plot shows in detail the formation of the crystalline phase between the selected parameters. The combination of synthesis parameters used for the DOE are shown on Table I.

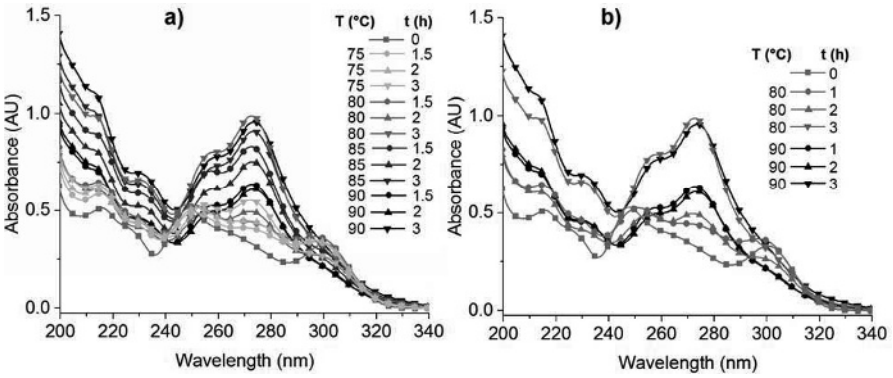

Figure 1. Absorption spectra for a) 75, 80, 85, and 90 °C synthesis temperatures and b) 80 and 90 °C at 3 synthesis times.

Table I. Combination of parameters defined by DOE.

Sample	Temperature (°C)	Time (h)	Purification procedure	
A	90	2	1	90-2-1
B			2	90-2-2
C	90	3	1	90-3-1
D			2	90-3-2
E	80	2	1	80-2-1
F			2	80-2-2
G	80	3	1	80-3-1
H			2	80-3-2

Crystalline structure and crystallite size

Core, core + 2 shells, and core + 4 shells lanthanum phosphate NPs for the different combinations of synthesis parameters were analyzed using XRD to evaluate the crystalline structure and crystallite size of the NPs. The XRD spectra for the core and core-shells NPs are shown in Figure 2 to 4 for the different parameters of temperatures and times. For the purification procedures there is no difference on the spectra, and hence on the crystalline structure and crystallite size. The broadening of the peaks, characteristic of nanocrystalline materials, is observed in all the spectra for the different samples. The spectra for the core NPs synthesized at the four combinations of parameters are shown in Figure 2. Comparing the spectra for the different parameters, it can be observed that for the lower temperature and time (80 °C and 2 h), the peaks are broader and less intense compare to the others. Moreover, the increase of temperature and time leads to sharper and well-defined peaks. A similar behavior can be observed on Figure 3 and 4 for core + 2 and core + 4 shells respectively.

The analysis of crystalline structure was done on the X'Pert HighScore Plus software using the ICDD database version number 2.0902. A crystalline structure of lanthanum phosphate with a hexagonal crystal system and a space group $P6_222$ (ICDD database Ref. code: 00-004-0635) was obtained for the core and core-shells structures synthesized at the different parameters combinations.

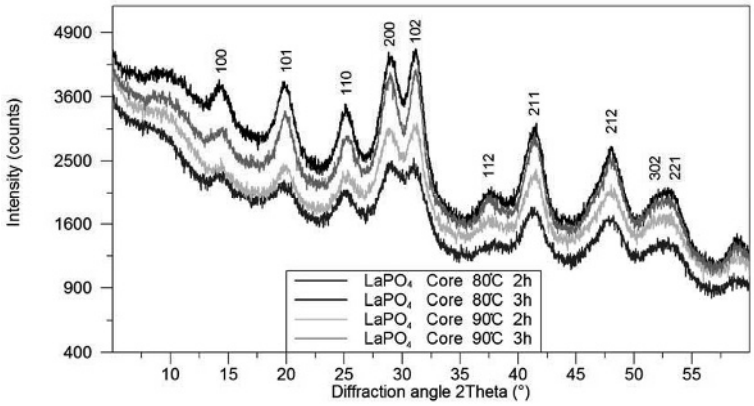

Figure 2. XRD spectra for $LaPO_4$ core NPs at the 4 combinations of synthesis temperature and time.

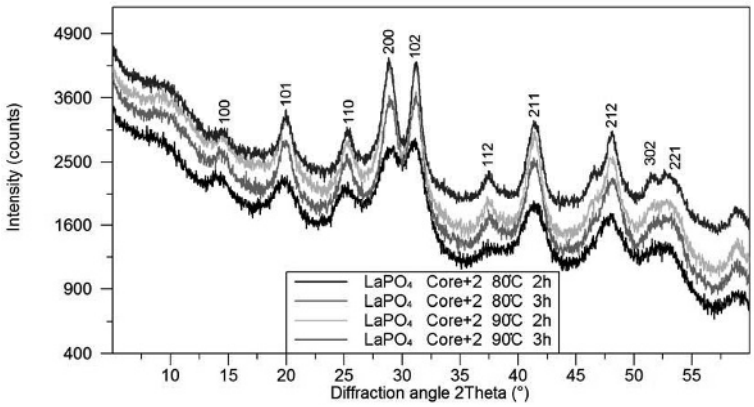

Figure 3. XRD spectra for $LaPO_4$ core + 2 shells NPs at the 4 combinations of synthesis temperature and time.

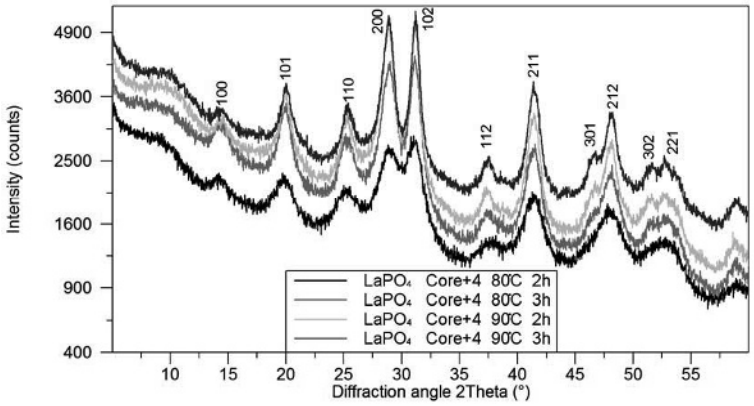

Figure 4. XRD spectra for $LaPO_4$ core + 4 shells NPs at the 4 combinations of synthesis temperature and time.

The XRD spectra were used to calculate the crystallite size using Scherrer equation [20]. For the crystallite size analysis, the peak located at ~ 41° was used. The results obtained for the different core and core-shells NPs at different synthesis parameters are shown on Figure 5. Comparing the values obtained for the core crystallite size for the parameters 80 °C - 3 h, 90 °C - 2 h, and 90 °C - 3 h there is not a statistical difference between them. Furthermore, an increase in the size of the NPs with the addition of shells for all the parameters was evidenced. Moreover, the increment of synthesis temperature or time has a direct influence with the growth of bigger NPs for the core and core-shells since the greatest values were obtained for 90 °C - 3 h.

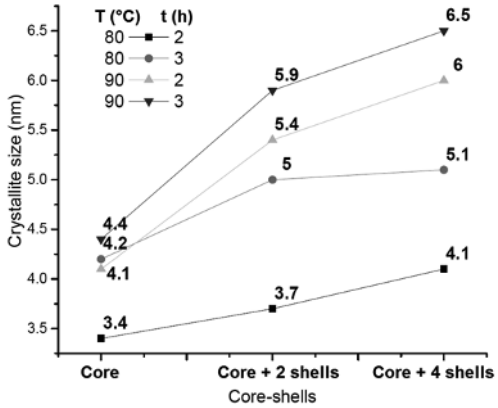

Figure 5. Crystallite size for core, core + 2 shells, and core + 4 shells NPs for different synthesis parameters.

Size, morphology, and distribution

TEM micrographs along with the particle size distributions of core and core + 4 shells synthesized at different synthesis temperatures and times are shown on Figures 6 to 8. The sample preparation on the formvar-carbon coated copper grid promotes the aggregation of NPs due to the surface dewetting and the "coffee-ring effect" as can be observed on Figures 6 and 7 [21]. The "coffee-ring effect" consists in the segregation of the NPs in the outer ring of the grid, increasing the density of NPs in this area and hence promoting aggregation. Although this makes the particle size measurement difficult, the contrast arising from electron diffraction in the crystalline NPs allows to distinguish and measure the size of individual NPs. In Figure 8 the larger presence of unreacted species from the phosphate precursor, built up through the addition of 4 shells to the core $LaPO_4$, becomes noticeable. The core and core-shells NPs can be approximated to a spherical morphology with an average diameter of 3.7 nm (± 0.6 nm), 3.5 nm (± 0.6 nm), and 4.9 nm (± 1 nm) for core 90 °C – 2 h, core + 4 shells 80 °C – 2 h, and core + 4 shells 90 °C – 3 h respectively. These results are slightly different to the ones obtained by XRD using Scherrer equation since XRD provides a statistical representation of the particle size due to the amount of sample that contributes to the diffraction, while TEM is a local measurement of the average NP diameter.

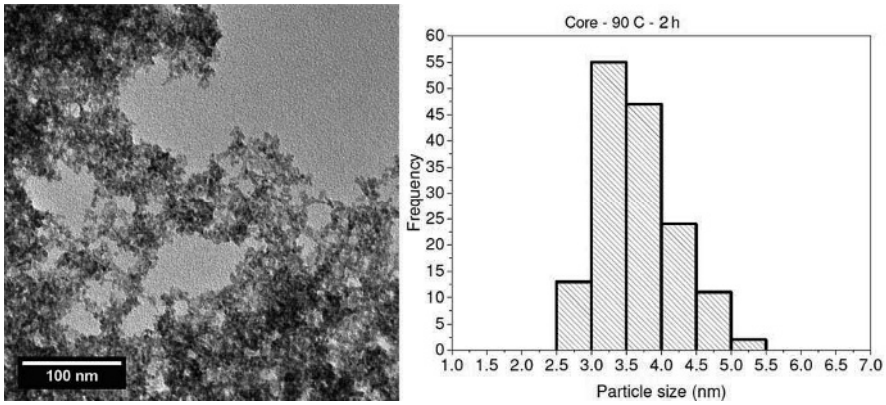

Figure 6. TEM micrograph and particle size distribution for core $LaPO_4$ synthesized at 90 °C for 2 hours.

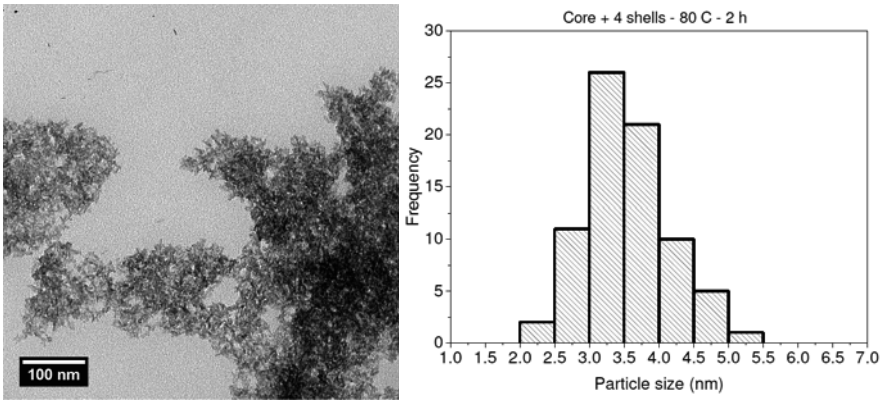

Figure 7. TEM micrograph and particle size distribution for core + 4 shells $LaPO_4$ synthesized at 80 °C for 2 hours.

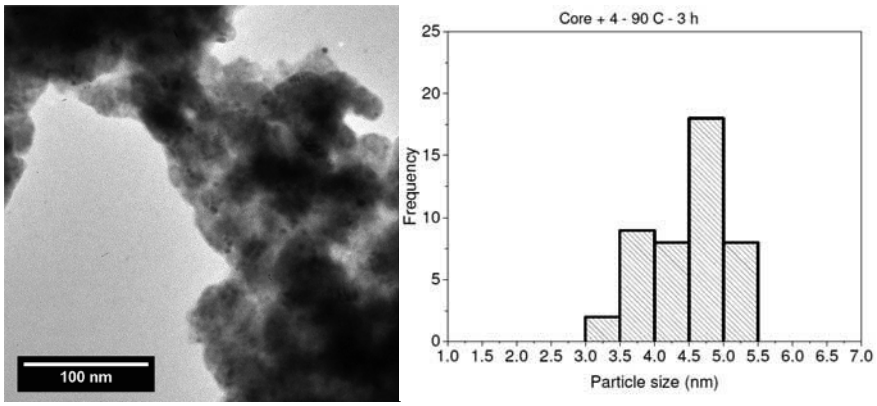

Figure 8. TEM micrograph and particle size distribution for core + 4 shells $LaPO_4$ synthesized at 90 °C for 3 hours.

Stability colloidal suspension

The colloidal behavior of the NPs in water was studied to determine the stability of all the different combination parameters using Zeta Potential. The pH of the various samples was measured prior to the zeta potential measurement giving a value of 6. Zeta potentials (ζ) were measured by laser Doppler velocimetry (Malvern Zen 3600 Zetasizer) using Henry's equation:

$$U_E = \frac{2\varepsilon\zeta f(ka)}{3\eta} \quad (1)$$

where ε is the dielectric constant of water, ζ is the zeta potential, *f*(ka) is the Henry's function, η is the medium viscosity, and U_E is the electrophoretic mobility. In Table II a summary of the average zeta potential and standard deviation for the different parameters is presented. According to Larsson et al., a suspension is considered stable when zeta potentials are greater than 30 mV or smaller than -30 mV [22]. Nonetheless, this assumption may not be accurate since NPs can be either monodisperse or in an aggregated state without significantly changing the magnitude of zeta potential [18]. Moreover, the NPs can loss their mechanical stability by showing sedimentation due to the difference in densities without the formation of aggregates. Besides, the magnitudes obtained are related with the conditions used to synthesize or prepare the NPs for the measurements, which restrict the possibility to compare results with the literature. For example, F. Meiser et al. studied the zeta potential of functionalize and bioconjugate lanthanide phosphate NPs as a function of pH obtaining a maximum value of ~ -40 mV [14]. Also, M. McLaughlin et al. reported the zeta potential of lanthanide phosphate NPs without surface modification, functionalized NPs, and bioconjugate NPs with a magnitude of -63.2, -56.4, and -27.9 mV respectively [11]. Therefore, two statistical tests were done to evaluate if the purification procedures affect the colloidal stability due to the influence of the concentration of unreacted species [23]. The ANOVA test and t-test revealed that the difference between the samples variance and means are not statistically different respectively.

Table II. Zeta potentials for different synthesis parameters and purification process for core, core + 2 shells, and core + 4 shells in a colloidal suspension with pH = 6.

		ZP (mV)	
		Purification process 1	Purification process 2
Core	80 °C - 2 h	-28.6 (±1.6)	
	80 °C - 3 h	-11.8 (±4.6)	
	90 °C - 2 h	-29.4 (±0.5)	
	90 °C - 3 h	-33.5 (±1.3)	
Core + 2 shells	80 °C - 2 h	-33.7 (±1.5)	-35.9 (±3.2)
	80 °C - 3 h	-34.4 (±1.5)	-35.9 (±1.5)
	90 °C - 2 h	-34.1 (±1.0)	-32.3 (±0.4)
	90 °C - 3 h	-34.4 (±0.7)	-32.4 (±1.2)
Core + 4 shells	80 °C - 2 h	-35.7 (±1.4)	-32.6 (±2.0)
	80 °C - 3 h	-32.2 (±1.3)	-32.6 (±0.8)
	90 °C - 2 h	-34.0 (±1.0)	-34.4 (±0.4)
	90 °C - 3 h	-34.1 (±1.4)	-33.0 (±1.2)

CONCLUSIONS

In this study, $LaPO_4$ core and core-shells NPs were synthesized with the aim to evaluate the influence of synthesis and purification parameters on the size, morphology, crystalline structure, and colloidal stability. The synthesis parameters, temperature and time, have a direct effect on the particle size, which increase with the increment of the temperature and/or time according to the hydrolysis reaction of tripolyphosphate groups to form orthophosphate ions.

Furthermore, there is no effect of these parameters on the crystalline structure and colloidal stability for the proposed combinations since a hexagonal crystalline structure of lanthanum phosphate was obtained for all the core and core-shell structures and the zeta potential is not statistically different among one another based on an ANOVA test. Finally, the proposed purification procedures did not show to have any influence in the morphology of the nanoparticles. Moreover, the difference on the zeta potential among the samples is not statistically significant. Therefore, the proposed purification procedures do not evidenced any effect in the colloidal stability of the NPs. However, for bioconjugation and in vivo studies the reduction of unreacted species may play an important role.

ACKNOWLEDGEMENTS
This work is being financed by the Virginia Commonwealth University with the support of the Mechanical and Nuclear Engineering department and the NRC-HQ-84-14-FOA-002, Faculty Development Program in Radiation Detection and Health Physics at VCU.

REFERENCES

1. L. Wang and Y. Yamauchi, Metallic nanocages: synthesis of bimetallic Pt-Pd hollow nanoparticles with dendritic shells by selective chemical etching, *J. Am. Chem. Soc.* **135,** 16762–5 (2013).

2. M. Mahmoud, D. O'Neil, and M. El-Sayed, Hollow and solid metallic nanoparticles in sensing and in nanocatalysis. *Chem. Mater.* **26,** 44–58 (2014).

3. A. Mesbahi, A review on gold nanoparticles radiosensitization effect in radiation therapy of cancer. *Reports Pract. Oncol. Radiother.* **15,** 176–180 (2010).

4. G. Cao, Nanostructures and Nanomaterials - Synthesis, Properties and Applications. *Imperial College Press* (2004).

5. H. Xu, L. Zeng, S. Xing, G. Shi, Y. Xian, and L. Jin, Microwave-radiated synthesis of gold nanoparticles/carbon nanotubes composites and its application to voltammetric detection of trace mercury(II). *Electrochem. commun.* **10,** 1839–1843 (2008).

6. K. Okuyama, W. Lenggoro, and T. Iwaki, Nanoparticle Preparation and Its Application - A Nanotechnology Particle Project in Japan. *2004 Int. Conf. MEMS, NANO Smart Syst.* 1–4 (2004).

7. H.-C. Huang, S. Barua, G. Sharma, S. K. Dey, and K. Rege, Inorganic nanoparticles for cancer imaging and therapy. *J. Control. Release* **155,** 344–357 (2011).

8. S. S. Kelkar and T. M. Reineke, Theranostics: combining imaging and therapy. *Bioconjug.*

Chem. **22,** 1879–903 (2011).

9. M. F. McLaughlin, J. Woodward, R. A. Boll, A. J. Rondinone, S. Mirzadeh, and J. D. Robertson, Gold-coated lanthanide phosphate nanoparticles for an 225 Ac in vivo, *Radiochim,* **101**, 595-600 (2013).

10. Woodward, J. *et al.* LaPO4 nanoparticles doped with actinium-225 that partially sequester daughter radionuclides, *Bioconjug. Chem.* **22,** 766–776 (2011).

11. M. F. McLaughlin, J. Woodward, R. A. Boll, J. S. Wall, A. J. Rondinone, S. J. Kennel, S. Mirzadeh, and J. D. Robertson, Gold Coated Lanthanide Phosphate Nanoparticles for Targeted Alpha Generator Radiotherapy, *PLoS One* **8,** 2–9 (2013).

12. J. V. Rojas, J. D. Woodward, N. Chen, A. J. Rondinone, C. H. Castano, and S. Mirzadeh, Synthesis and characterization of lanthanum phosphate nanoparticles as carriers for 223Ra and 225Ra for targeted alpha therapy, *Nucl. Med. Biol.* **42,** 614–620 (2015).

13. M. F. McLaughlin, D. Robertson, P. H. Pevsner, J. S. Wall, S. Mirzadeh, and S. J. Kennel, LnPO4 nanoparticles doped with Ac-225 and sequestered daughters for targeted alpha therapy, *Cancer Biother. Radiopharm.* **29,** 34–41 (2014).

14. F. Meiser, C. Cortez, and F. Caruso, Biofunctionalization of fluorescent rare-earth-doped lanthanum phosphate colloidal nanoparticles, *Angew. Chemie - Int. Ed.* **43,** 5954–5957 (2004).

15. C. Heneweer, J. P. Holland, V. Divilov, S. Carlin, and J. S. Lewis, Magnitude of enhanced permeability and retention effect in tumors with different phenotypes: 89Zr-albumin as a model system, *J. Nucl. Med.* **52,** 625–633 (2011).

16. A. E. Grechanovsky, N. N. Eremin, and V. S. Urusov, Radiation Resistance of LaPO4 (Monazite Structure) and YbPO4 (Zircon Structure) from Data of Computer Simulation, *Physics of the solid state,* **55,** 1929–1935 (2013).

17. F. Gambinossi, S. E. Mylon, and J. K. Ferri, Aggregation kinetics and colloidal stability of functionalized nanoparticles, *Adv. Colloid Interface Sci,* (2014).

18. V. Buissette, D. Giaume, T. Gacoin, and J.-P. Boilot, Aqueous routes to lanthanide-doped oxide nanophosphors, *J. Mater. Chem,* **16,** 529 (2006).

19. V. Buissette, M. Moreau, T. Gacoin, J.-P. Boilot, J.-Y. Chane-Ching, and T. Le Mercier, Colloidal synthesis of luminescent rhabdophane LaPO4:Ln 3+·xH2O (Ln = Ce, Tb, Eu; x

≈ 0.7) nanocrystals, *Chem. Mater,* **16,** 3767–3773 (2004).

20. B. D. Cullity and R. S. Stock, *Elements of X-Ray Diffraction*. (Addison-Wesley Publishing Company, 1956).

21. B. Michen, C. Geers, D. Vanhecke, C. Endes, B. Rothen-Rutishauser, S. Balog, and A. Petri-Fink, Avoiding drying-artifacts in transmission electron microscopy: Characterizing the size and colloidal state of nanoparticles, *Sci. Rep.,* **5,** 9793 (2015).

22. M. Larsson, J. Duffy, and A. Hill,n Suspension stability : Why particle size , zeta potential and rheology are important. *Www.Malvern.Com* **20,** 1–35 (2011).

23. Instruments, B. & Technical, C. Colloidal Stability in Aqueous Suspensions : Two Variables. **1,** 1–4 (1896).

ZINC OXIDE NANOPARTICLES FOR SPACE SATELLITE SOLAR PANEL PROTECTION LAYER

Phillip Clift[*], Jordan Wladyka, Tyler Payton, and Dale Henneke[**]
New Mexico Institute of Mining and Technology
Socorro, New Mexico, USA

ABSTRACT

Space solar panels have a protective layer (i.e., a flexible, cover-glass material), which protects the panel from solar radiation. Unfortunately, current formulations of this layer are inadequate due to an accumulation of electrical charge over time, which causes the protective layer to decay and reduces its effectiveness. This work describes a synthesis method for zinc oxide (ZnO) nanoparticles, their characterization, and incorporation into a novel composite material that could serves as a replacement for the current cover glass technology. The ZnO nanoparticles provide a conduit within the composite for the electrical charge to dissipate. It was found that composites having as little as 2wt% ZnO nanoparticle provided greater than 10,000× improvement in the electrical conductivity of the protective layer while reducing the optical transmission of usable light by approximately 10%.

INTRODUCTION

State of the art solar panels that are used in space applications are rolled or folded into a pre-launch configuration, which is unfurled once the satellite reaches orbit. These solar panels have a protective layer that is composed of a composite material containing a silicone-based matrix with glass bead filler; this composite is called pseudomorphic glass (PMG). Figure 1 depicts a cross-section of a typical solar panel using a PMG protective layer and substrate.

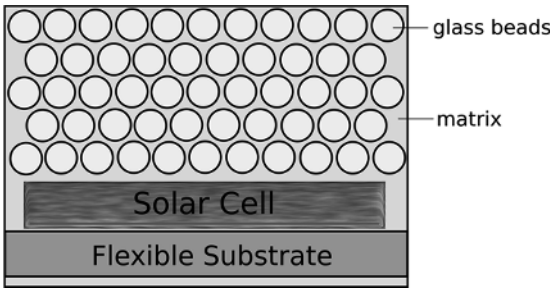

Figure 1. Conceptual design of flexible solar array with PMG coverglass and PMG substrate for hybrid configuration.

PMG Formulations

The PMG provides protection against space radiation (i.e., cosmic radiation), it is flexible, will not fracture when rolled, and it is transparent to light that is converted to electricity by the solar cell (i.e., EM radiation on the order of 200 to 2500 nm). The layer must be optically transparent over this range of wavelengths or the solar array will not function. The traditional PMG layer accumulates electrical charge, which leads to degradation overtime. To mitigate the accumulation of electrical charge, the layer should be electrically conductive but must also retain

1 Author e-mail address: pclift@nmt.edu
2 Corresponding author. E-mail: henneke@nmt.edu

its mechanical flexibility and optical transparency.

Wilt and Levin[1,2] improved the electrical conductivity of PMG by incorporating aluminum-zinc oxide (AZO) and indium-tin oxide (ITO) into the PMG layer. Multiple samples were made by loading a variety of weight fractions of AZO and ITO into the composite; the loading varied from 0.001 to 0.5wt%. At 0.1wt% AZO loading, the electrical conductivity was found to be around 9×10^{-13} S/cm at 500V, while the optical transparency compared to unloaded PMG was found to be 85% at a wavelength of 500nm. For a loading of 0.1wt% ITO, the electrical conductivity was found 2.8×10^{-13} S/cm at 500V, while the optical transparency at 500nm was reduced to 90%. It was shown that electrical conductivity can be improved by incorporating electrically conductive materials into the PMG layer, but there is a loss of optical transparency even when using materials that are traditionally considered to be transparent.

Zinc oxide could be used as an alternative to AZO and ITO composite formulations due to its optical transparency over the relevant wavelength range and its electrical conductivity. ZnO has a band gap around 3.37 eV at 300K [2] and is commonly used as a transparent thin film electrode layer for amorphous Si solar cells and varistors[3,4]. Nanoparticles of ZnO can be made with a variety of morphologies that would effectively dissipate accumulated charge in a PMG layer.

Zinc Oxide Agglomerates

Swati *et al.*,[5] produced ZnO agglomerates (ZnO-A) and characterized their chemical and physical properties with both organic or inorganic precursors. ZnO-A were produced using a variety of organic and inorganic precursors (e.g., zinc acetate, zinc nitrate, and zinc chloride). The precursors were mixed together and placed into a pre-heated furnace at ~900°C in a pure oxygen environment until the reaction was complete. After synthesis, the ZnO-A powder was studied using differential scanning calorimetry (DSC), X-ray diffraction (XRD), scanning electron microscopy (SEM), and photoluminescence emission (PLE).

From the DSC data, it was determined that the optimal temperature for this sol-gel reaction was ~900°C, due to the overall weight loss reaching a maximum of 92.4% from thermal decomposition. This temperature represents the highest yield for ZnO-A that can be formed using this method. XRD was used to verify the crystallite size, as well as, impurities in the ZnO-A. It was evident from the XRD data that the use of organic precursors yielded the smallest crystallite size (~13.45nm) when compared to other inorganic precursors. PLE was used to determine the optical properties of the ZNO-A. The emission spectra intensities increased and shifted from 2.28eV to 2.82eV, from green to blue emission of the visible light spectra, as crystallite size was reduced. SEM provided visual evidence of the surface morphologies for the ZnO-A synthesized from various precursors (i.e., zinc acetate, zinc chloride, zinc nitrate). The ZnO-A, with zinc acetate and zinc nitrate precursors, possessed similar morphologies with primary and secondary agglomerates attached to one another. Whereas, the zinc chloride was found to have primary and secondary particles, in the form of platelets, stacked on one another.

Zinc Oxide Tetrapods

Wang *et al.*,[6] synthesized and characterized ZnO tetrapods (ZnO-T) to better understand the formation mechanism of ZnO nanocrystals. ZnO-T have a morphology that is a polyhedral caltrop with a zinc blende core crystal structure and wurtzite crystals protruding from the [111] faces. The wurtzite legs are separated at an angle of 120° with respect to each of their positions. Wang *et al.* made the ZnO-T by placing zinc powder in quartz boat and heating it in a tube furnace to ~850°C in an oxygen / argon environment. The gas was set to flow through the quartz tube at rate of 10 sccm for O_2 and 100 sccm for Ar. As the zinc vaporized, it reacted with oxygen in the tube furnace forming ZnO-T, which was collected onto a silicon substrate that was placed above the zinc powder. The collected material was examined by XRD and TEM.

XRD data verified the composition of the ZnO-T showing with three major peaks at 32°, 34°, and 36° (2θ) representing the (100), (002), and (101) planes for the wurtzite structure, respectively. Selected area diffraction (SAD) was done using TEM, which showed evidence of a wurtzite crystal structure for the ZnO-T legs with a growth direction of the legs in the {0001} direction with a lattice parameter of 0.259 nm. There was evidence that the oxygen content played a major role in the growth of ZnO-T. Higher concentrations of oxygen produced longer the legs on the ZnO-T, while the growth rates that were observed corresponded to kinetically controlled growth.

EXPERIMENTAL PROCEDURE

Zinc oxide agglomerates were synthesized using a sol-gel process adapted from Swati *et al.* [7]. The reagents that were used, both of which were obtained from Alfa Aesar, are: ACS grade zinc acetate and ACS grade citric acid. An aqueous solution, having a molar ratio of 1:1:10 zinc acetate dehydrate to citric acid to water, was mixed in a beaker. 40mL of this solution was poured into a quartz boat, placed into a tube furnace, and heated to 900°C for 30 minutes. The material that was removed from the boat was used as the ZnO-A material for composite testing.

Zinc oxide tetrapods were synthesized using an adaption of the method described by Wang *et al.* [6]. The experimental setup (see Figure 2) permitted control of the reaction temperature, ambient gas flowrate, and reaction pressure. ACS grade Zinc Powder (99.9%) having particles ranging in size from 1 to 5 μm was obtained from Atlantic Equipment Engineers Inc. The Zn powder was placed into a quartz boat and heated to ~900°C at a pressure of 1 atm with a gas mixture having 5%$_{vol}$ oxygen / 95%$_{vol}$ argon flowing at a rate of 100 sccm.

After synthesis both of the ZnO products were characterized to determine particle size and morphology. SEM was used to determine the morphology of the particles as well as relative particle size. XRD was performed to confirm the crystal structure of both nanocrystalline materials and to confirm the purity of the final product after synthesis.

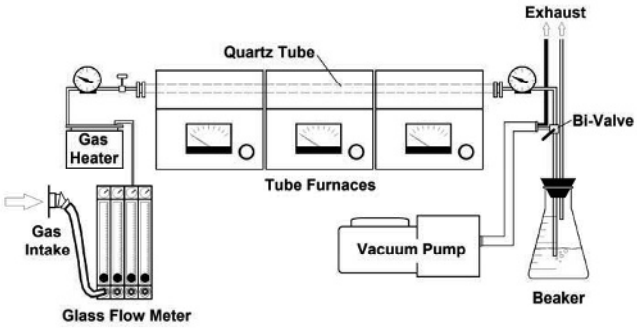

Figure 2. Schematic of tube furnace and synthesis apparatus.

The synthesized ZnO-A and ZnO-T materials incorporated into the PMG composite in various weight percentages. The PMG composite was made using a two-part space grade silicone resin from Dow-Corning (DC93-500) mixed with fused silica beads ranging in size from 1-20μm. The synthesized zinc oxide materials were mixed with the resin and beads, then tape cast onto a glass substrate. The casts were made 0.127mm thick and the composite material was left to cure for 24 hours. The cast composite material was then analyzed using UV/VIS spectrometry to determine it transmissivity and with a conventional four-point resistivity probe tester to find its

conductivity.

RESULTS AND DISCUSSION

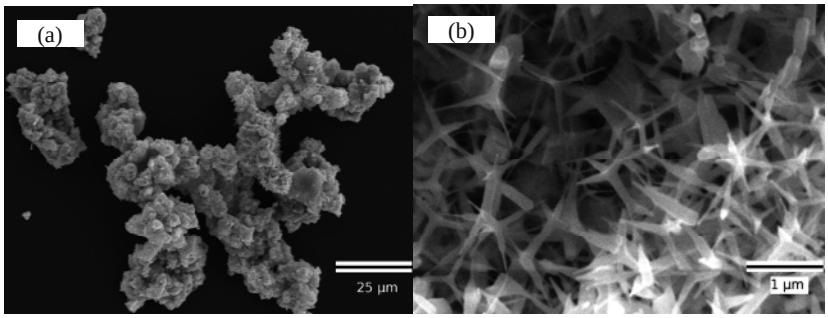

Figure 3. (a) SEM images of ZnO-A and (b) ZnO-T.

The morphologies of the zinc oxide agglomerates (ZnO-A) and tetrapods (ZnO-T) were analyzed by SEM; Figure 3 shows images of the resulting materials. Figure 3a depicts the ZnO-A material collected after synthesis, while Figure 3b shows the ZnO-T collected on a silicon wafer placed ~5 cm downstream from the quartz boat. In figure 3a, the resulting ZnO-A material was found to be similar to the material made by Swati *et al.* with the primary and secondary spherical particles agglomerated in the same fashion. The synthesized ZnO-T material (shown in figure 3b) is also quite similar to what was made by Wang *et al.* and it possesses the same polyhedron caltrop geometry. These ZnO materials were then mixed by milling with fused silica beads and reanalyzed by SEM, as shown in Figure 4.

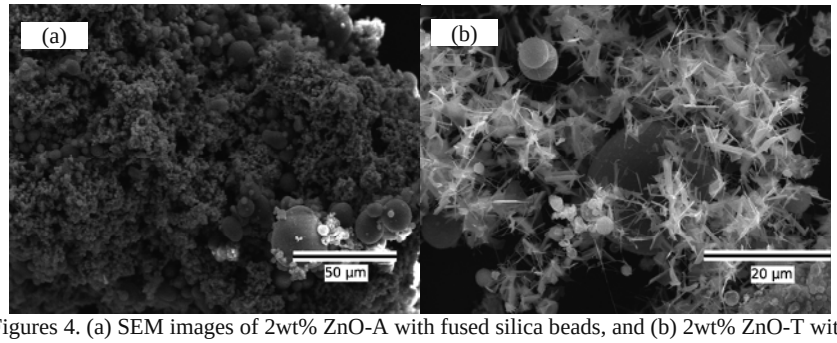

Figures 4. (a) SEM images of 2wt% ZnO-A with fused silica beads, and (b) 2wt% ZnO-T with fused silica beads.

The ZnO-A and fused silica bead blended at 2wt% can be seen in figure 4a; the overall size of the 1-20 µm beads can be seen in contrast with the ZnO-A material. Figure 4b shows the same weight percent blend with ZnO-T and glass beads. The ZnO-T is clearly visible and seems to adhere to the larger beads, but not the smaller beads.

The ZnO materials and fused silica were mixed with the PMG composite and tape cast to form 5 mil thick sheets. Four tape cast composites were made, two with ZnO-A and two with

ZnO-T. Each pair of tape casts, with respective ZnO nanoparticles, was incorporated with either 2wt% or 6wt% of the ZnO materials. After curing the samples, they were sectioned into smaller specimens and analyzed using UV/Vis spectrometry and four-point probe conductivity testing.

Figure 5 depicts the transmissivity of the tape-cast composite materials. The transmittance percentage for the ZnO-A 2wt% and 6wt% at 500 nm are: 86.5% and 81.6%; respectively. For the ZnO-T, the transmittance for the ZnO-T at 2wt% and 6wt% at 500 nm are: 84.9% and 77.4%; respectively. The slight deviations in the UV/Vis spectra between the 2wt% and the 6wt%, of the ZnO-A and ZnO-T, may be attributed to the agglomeration of ZnO materials during the tape casting process.

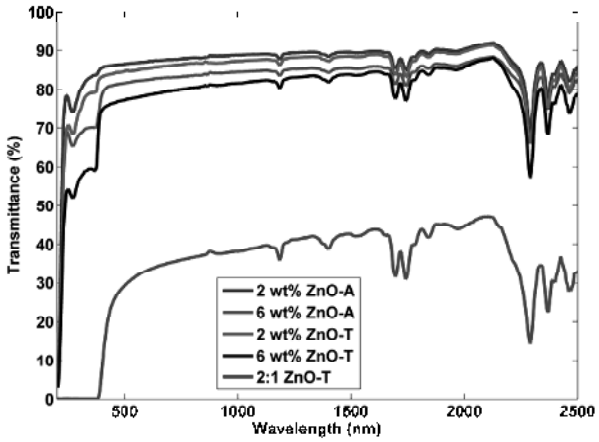

Figure 5. UV/Vis spectra of composite with various loadings of ZnO nanocrystals.

Table I. Resistance, conductivity, and transmissivity at 500 nm for ZnO-A and ZnO-T PMG composites at different loadings.

Sample	Thickness [mm]	Resistance [ohm/sq]	Conductivity [S/cm]	Transmissivity [%] (at 500nm)
2wt% ZnO-A	0.12	1.14×10^{8}	7.30×10^{-7}	86.5
6wt% ZnO-A	0.12	7.44×10^{7}	1.12×10^{-6}	81.6
2wt% ZnO-T	0.11	1.50×10^{8}	6.06×10^{-7}	84.9
6wt% ZnO-T	0.12	6.12×10^{7}	1.36×10^{-6}	77.4

The conductivity of the composite material as determined by four-point probe measurement (without a bias voltage applied to the sample), can be seen in Table I. The conductivity of ZnO-A composite was found to increase by 21.1% as the ZnO loading increased from 2wt% to 6wt%. For the ZnO-T composites, an increase of 38.3% for the same change in ZnO loading was observed. When comparing the two forms of ZnO (ZnO-A to ZnO-T) at 2wt%, a 9.3% increase in the conductivity was found. At 6wt%, the increase in conductivity was found to be 9.7% for the tetrapods when compared to the agglomerates.

Figure 6 compares the conductivity (S/cm) of various composite materials as a function of

conductive filler loading within the composite (wt%). The data from Table I is plotted in Figure 6 along with data from Wilt *et al.* The four data points corresponding to the ZnO-A and ZnO-T composites appear in the top-center and top-right corner of the plot. It is clear that these samples have orders of magnitude improvement in the conductivity while having a similar loss in the optical transmissivity.

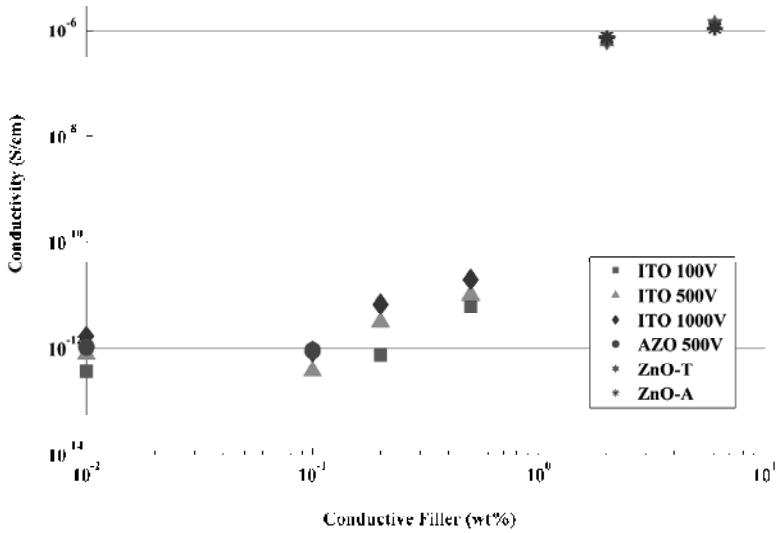

Figure 6. Conductivity plot of ZnO composite materials. ITO and AZO composite data is from Wilt *et al.* [1], these composites were tested with and without an induced voltage applied to the sample. The ZnO-A and ZnO-T composites were only tested without an applied voltage.

It is possible that a percolation network within the composite may have permitted a complete circuit from one ZnO site to another, which would increase the conductivity of the composite while maintaining much of its optical transparency. This is especially true since the optical transparency of bulk ZnO is substantially less than that of nanometer sized ZnO particles in small dispersed quantities. However, it is still possible to produce 1D thin films of ZnO and have the material possess full transparency [15].

CONCLUSION

ZnO-A and ZnO-T composites had higher conductivities values (~μS/cm) compared to the ITO and AZO composites made by Wilt *et al.* (~pS/cm) [1]. The optical transmissivity of the ZnO composites was similar to that of ITO and AZO, but at a much higher material loading. ZnO-A and ZnO-T composites are clearly a better solution than either ITO or AZO for replacing current coverglass materials.

These results indicate ZnO nanomaterials outperform both AZO and ITO, but an optimal loading amount still needs to be determined, as well as, a method to uniformly disperse the ZnO

materials within the PMG. This data shows significant gains in transmittance and conductance when compared to ITO and AZO at the same level of loading.

The data may be indicative of a percolation conduction where the n-type ZnO is behaving as the conduction network through the polymer composite matrix. It should also be noted with the intrinsic defects of ZnO, the material will be dominated by oxygen vacancies. However, since ZnO-T was synthesized in 5% oxygen and the remainder was Zn and Argon vapor. It is possible that the ZnO-T may have extra Zn atoms at oxygen vacancy sites. This may increase the concentration of available electrons, but reduces hole concentration and mobility. In other literature, it has been shown that ZnO used as a conductive network in a polymer matrix does increase conductivity for thin film applications, as described by Oosterhout *et al.*[13]. Hong *et al.*[14] describe the conduction of a charge, via a percolation network of micron sized to nano-sized particles, is mainly attributed to the tunneling effect.

More research and testing is in progress to verify the data and observations made thus far.

ACKNOWLEDGEMENTS

We would like to extend a special thanks to Dave Wilt, of the Kirtland Air Force Research Lab, for supplying the some of the raw materials; and for allowing us to use the characterization equipment for this research. Without his help none of this would have been possible.

REFERENCES

[1] Z. S. Levin, D. Wilt, R. Hoffman, and D. Ferguson, Conductive Solar Cell Cover Glass Replacement For Electric Propulsion Environments, *Phys, Sim, and Photon. Eng. Photo. Devices.,* **8981**, 1-5 (2014).

[2] D. Wilt, A. Howard, N. Snyder, T. Sahlstrom, N. Heersema, L. Nathan, T. Ohshima, S. Sato, and M. Imaizumi. PseudoMorphic Glass to enable high efficiency space photovoltaic devices. *PVSC,* **37th IEEE**, 001949-54 (2011).

[3] B. Rech and H. Wagner, Potential of amorphous silicon for solar cells, *Appl. Phys. A,* **69**, 155-167 (1999).

[4] K. Ellmer, A. Klein, and B. Rech, Transparent Conductive Zinc Oxide: basics and Applications in Thin Film Solar Cells, Springer Series, **104**, 70 (2008).

[5] G. Swati, S. Mishra, D. Yadav, R.K. Sharma, D. Dwivedi, N. Vijayan, J.S. Tawale, V. Shanker, and D. Haranath, High yield synthesis and characterization of aqueous zinc oxide nano-crystals using various precursors*, J. Alloys and Cmpnds*, **571**, 1-5 (2013).

[6] F.Z. Wang, Z.Z. Ye, D.W. Ma, L.P. Zhu, and F. Zhuge, Novel morphologies of ZnO nanotetrapods, *Mater. Lett.,* **59**, 560 – 563 (2005).

[7] M. Kitano, T. Hamabe, and S. Maeda, Growth of large tetrapod-like ZnO Crystals I: Experimental considerations on kinetics of growth. *J. Crystal Growth*, **102**, 965-973 (1990).

[8] M. Kitano, T. Hamabe, S. Maeda, and T. Okabe, Growth of large tetrapod-like ZnO crystals II: Morphological considerations on growth mechanism. *J. Crystal Growth*, **108**, 277-284 (1991).

[9] M.C. Newton, S. Ferth, T. Matsuura, and P. A. Warburton, Synthesis and characterization of zinc oxide tetrapod nanocrystals. *J. Phys.*, **26**, 251-255 (2006).

[10] N.A. Samat, R. M. Nor, Sol–gel synthesis of zinc oxide nanoparticles using Citrus aurantifolia extracts. *Ceramics Intl.*, **39**, 545-548 (2013).

[11] Q. Wan, K. Yu, T.H. Wang, and C.L. Lin, Low-field electron emission from tetrapod-like ZnO nanostructures synthesized by rapid evaporation. *Appl. Phys. Lett.*, **83-11**, 2253-2255 (2003).

[12] Z. Zhang, H. Yuan, Large-scale synthesis and optical behaviors of ZnO tetrapods. *Appl. Phys. Lett.,* **90**, 1-3 (2007).

[13] S.D. Oosterhout, L. Koster, S.S. van Bavel, J. Loos, O. Stenzel, R. Thiedmann, V. Schmidt, B.

Campo, T.J. Cleij, L. Lutzen, and D. Vanderzande, Controlling the morphology and efficiency of hybrid ZnO: polythiophene solar cells via side chain functionalization. *Advanced Energy Materials*, **1(1)**, 90-96 (2011).
[14] J.I. Hong, L.S. Schadler, R.W. Siegel, and E. Mårtensson, Rescaled electrical properties of ZnO/low density polyethylene nanocomposites. *Applied physics letters*, **82(12)**, 1956-1958 (2003).
[15] E.M. Fortunato, P.M. Barquinha, A.C.M.B.G. Pimentel, A.M. Gonçalves, A.J. Marques, L.M. Pereira, and R.F. Martins, Fully Transparent ZnO Thin-Film Transistor Produced at Room Temperature. *Advanced Materials*, **17(5)**, 590-594, (2005).